Etude expérimentale et numérique de la rupture ductile sous chargement multiaxial

Jessica Papasidero

Manuscrit présenté par

Jessica PAPASIDERO

pour l'obtention du grade de

Docteur de l'École Polytechnique

Spécialité : MÉCANIQUE

Laboratoire de Mécanique des Solides
Ecole Polytechnique
91120 Palaiseau, France

Étude expérimentale et numérique de la rupture ductile sous chargement multiaxial

Soutenue le 16 janvier 2014 devant le jury composé de :

Tudor BALAN	Examinateur
Ahmed BENALLAL	Rapporteur
Jacques BESSON	Examinateur
Pierre-Olivier BOUCHARD	Examinateur
Véronique DOQUET	Co-directrice de thèse
André DRAGON	Rapporteur
Dirk MOHR	Co-directeur de thèse

Abstract

A stocky tubular tension-torsion specimen geometry was optimized to characterize the effect of the stress state (stress triaxiality and Lode angle parameter) on metals ductility, at low stress triaxialities. Biaxial tests (proportional and non-proportional) were performed on 36NiCrMo16 steel and 2024-T351 aluminum alloy. Strain fields were measured by stereo-correlation of digital images during the tests. Loading paths to fracture (evolution of the equivalent plastic strain, the stress triaxiality and the Lode angle parameter at the critical point) were determined. The evolution of aluminum ductility with respect to the stress triaxiality measured from tension-torsion tests differed substantially from that obtained by Bao and Wierzbicki in 2004. Indeed, the latter suggested a minimal ductility under shear, while the tension-torsion technique revealed a maximal ductility under shear. Non-proportional loading paths were shown to have an influence on ductility, by means of tests consisting in a pre-compression, pre-tension or pre-torsion, followed by a proportional loading sequence under combined tension-torsion. SEM observations of metallographic sections from biaxial interrupted tests, a real-time monitoring of the surface strain and damage during in-situ torsion tests in the SEM, and a crack propagation test coupled with in-situ X-ray synchrotron laminography brought evidences of localization phenomena at different scales, and of the growth of some cavities, even under pure shear, by contrast with the total collapse predicted by unit cell models. This growth may be due to the significant axial elongation measured under pure torsion (Swift effect). Shear localization was identified as the main coalescence mechanism, which justifies the choice of the Hosford-Coulomb fracture initiation criterion. Used in conjunction with a non-linear damage indicator, it accounts for the measured ductilities, even under possibly non-proportional loadings.

Acknowledgements

Je remercie le Laboratoire de Mécanique des Solides de m'avoir accueillie dans ses locaux.

Je tiens à exprimer ma gratitude envers mes directeurs de thèse, Véronique Doquet et Dirk Mohr, qui m'ont encadrée et guidée tout au long de ces trois années de doctorat.

Je remercie mes rapporteurs MM Benallal et Dragon, ainsi que MM Balan, Besson et Bouchard d'avoir accepté d'évaluer ce travail.

Je souhaite ensuite remercier Vincent De Greef et Erik Guimbretière, qui m'ont beaucoup appris et aidée dans l'utilisation des machines d'essais et la réalisation des montages. Un très grand merci également à Daniel Caldemaison qui m'a fait faire mes premiers pas avec le MEB, et à Alexandre Tanguy qui a partagé avec moi son savoir et son expérience en microscopie et en préparation métallographique.

Une mention spéciale pour Sébastien Lepeer, mon stagiaire, qui, par sa motivation, son efficacité, et son travail méticuleux, a largement contribué à certains résultats présentés dans le chapitre III de cette thèse. Merci, et bravo, Sébastien !

Je tiens également à remercier très chaleureusement Thilo Morgeneyer, chargé de recherche au Centre des Matériaux, qui m'a accueillie au sein de son équipe et m'a offert l'opportunité de réaliser des essais à l'ESRF de Grenoble, au cours des derniers mois de ma thèse.

J'en viens maintenant aux personnes avec qui je n'ai pas travaillé, mais dont la présence a grandement contribué à la bonne ambiance et qualité de vie nécessaires à la réalisation d'un travail dans les meilleures conditions. Merci aux doctorants et post-doctorants du LMS qui ont partagé mon quotidien. Merci à Camille, Fabien, Gauthier qui ont été parmi les premiers « jeunes » du laboratoire dont j'ai croisé le chemin ; à mes chers co-bureau JB, puis Chus ; à mon voisin de bureau Clément ; à Armel dont les anecdotes et la culture ne cessent de m'impressionner ; à Barbara et Aurélie ; à Matthieu et Mathieu, Christian, Gongyao, Borja, David, Dennis ; bien sûr, à nos dignes représentants, Dimitri et Gwen. Merci aussi à l'ensemble du secrétariat du LMS : Alexandra, Anna, Christiane, Valérie, Danielle, dont le

travail fantastique transforme les formalités administratives les plus fastidieuses en une promenade.

Merci à mes amis musiciens Laurent, Pierre et Alexandra, pour nos répétitions qui ont rythmé une grande partie de cette période.

Merci à mes amis Anne, Chloé et Charles.

Un grand merci à ma famille, à mes parents. Vingt-cinq ans après s’être assise sur son premier banc d’école, votre fille a enfin terminé ses études !

Et merci à Raphaël, pour son soutien de tous les instants.

Table of Content

Introduction

The interest on ductile fracture can be explained by several factors: necessity of mastering metal forming processes, understanding and improving materials and structures limitations in systems submitted to complex stress states and in which safety is of paramount importance (aeronautics, automotive industry, railways, nuclear power generation, civil engineering…). This subject has drawn attention for several decades. A recent renewal of this interest was associated with the production of nano-structured metals by severe plastic deformation. Though a lot has been achieved in understanding and modelling ductile fracture, the need for more accurate insight in damage mechanisms and predictive fracture models is still very high.

Without pretention to exhaustivity – as the work undertaken in this topic is extremely large – this section proposes a synthetic overview of major contributions on ductile fracture. First, the parameters used to describe a stress state will be defined, as researchers are most interested in their influence on failure. Then, elements from the literature concerning the macroscopic, microscopic and modelling aspects of ductile fracture will be presented.

1. Stress state definition

The stress state at a point P corresponding to a stress tensor $\boldsymbol{\sigma}$ is illustrated in Fig. 0-1. It consists in a hydrostatic component (OO') and a deviatoric component (O'P), and can be represented in the principal stress space by its ordered principal stresses $\{\sigma_1, \sigma_2, \sigma_3\}$, with $\sigma_1 \geq \sigma_2 \geq \sigma_3$. It can also be defined in a unique way by its three invariants I_1, J_2 and J_3:

$$I_1 = tr(\boldsymbol{\sigma}) \tag{0.1}$$

$$J_2 = \frac{1}{2} tr(\mathbf{s}^2) \tag{0.2}$$

$$J_3 = \frac{1}{3} tr(\mathbf{s}^3) \tag{0.3}$$

where **s** is the deviatoric stress tensor. I_1 is related to the mean stress σ_m by :

$$\sigma_m = \frac{1}{3} I_1 \tag{0.4}$$

while J_2 is related to the Mises equivalent stress $\bar{\sigma}$ by:

$$\bar{\sigma} = \sqrt{3 J_2} \tag{0.5}$$

The stress state P (Fig. 0-1) is often conveniently expressed in the Haigh-Westergaard cylindrical coordinate frame $\{\xi, \rho, \theta\}$. In this frame, ξ is the magnitude of the hydrostatic component $\boldsymbol{\xi} = (\sigma_m, \sigma_m, \sigma_m)$, and ρ is the magnitude of the deviatoric stress $\mathbf{s} = (s_1, s_2, s_3)$. Therefore:

$$\xi = \sqrt{3}\sigma_m = \frac{1}{\sqrt{3}} I_1 \tag{0.1}$$

$$\rho = \sqrt{2 J_2} \tag{0.2}$$

The angle θ, measured from the $\mathbf{s_1}$ axis in the Π-plane -which is also the projection of σ_1 on this plane-, is known as the Lode angle. Its expression depends on the second and third invariant. If one considers the units vector $\mathbf{e} = \left(\sqrt{\frac{2}{3}}, -\frac{1}{\sqrt{6}}, -\frac{1}{\sqrt{6}}\right)$ colinear to $\mathbf{s_1}$, θ can be expressed as:

$$\mathbf{s}.\mathbf{e} = \rho \cos(\theta) \tag{0.3}$$

i.e.:

$$\cos(\theta) = \frac{\sqrt{3} s_1}{2\sqrt{J_2}} \tag{0.4}$$

Besides:

$$\cos(3\theta) = 4\cos^3(\theta) - 3\cos(\theta) \tag{0.5}$$

Combining (0.4) and (0.5) yields:

$$\cos(3\theta) = \frac{27}{2}\frac{\det(\mathbf{s})}{\bar{\sigma}^3} = \frac{3\sqrt{3}}{2}\frac{J_3}{J_2^{3/2}} \tag{0.6}$$

The Lode angle θ ranges from 0 to π/3. The relationship between the principal stresses and the Haigh-Westergaard coordinates is:

$$\begin{pmatrix} \sigma_1 \\ \sigma_2 \\ \sigma_3 \end{pmatrix} = \frac{1}{\sqrt{3}} \begin{pmatrix} \xi \\ \xi \\ \xi \end{pmatrix} + \sqrt{\frac{2}{3}} \rho \begin{pmatrix} \cos(\theta) \\ \cos\left(\theta - \frac{2\pi}{3}\right) \\ \cos\left(\theta + \frac{2\pi}{3}\right) \end{pmatrix} \tag{0.7}$$

A dimensional analysis shows that the stress state can be characterized by two independent non-dimensional parameters. It is very frequent, in ductile fracture studies, to use the stress triaxiality ratio η, and the Lode angle parameter $\bar{\theta}$, defined as:

$$\eta = \frac{I_1}{3\sqrt{3J_2}} = \frac{\sigma_m}{\bar{\sigma}} \tag{0.8}$$

$$\bar{\theta} = 1 - \frac{6}{\pi}\theta \tag{0.9}$$

The stress triaxiality η is the ratio between the hydrostatic stress and the von Mises equivalent stress. The Lode angle parameter $\bar{\theta}$ ranges from -1 to 1. Sometimes, another definition of the Lode parameter, μ, is used (Lode, [1]):

$$\mu = \frac{2(\sigma_2 - \sigma_1 - \sigma_3)}{\sigma_1 - \sigma_3} = \sqrt{3}\tan(\theta) \tag{0.10}$$

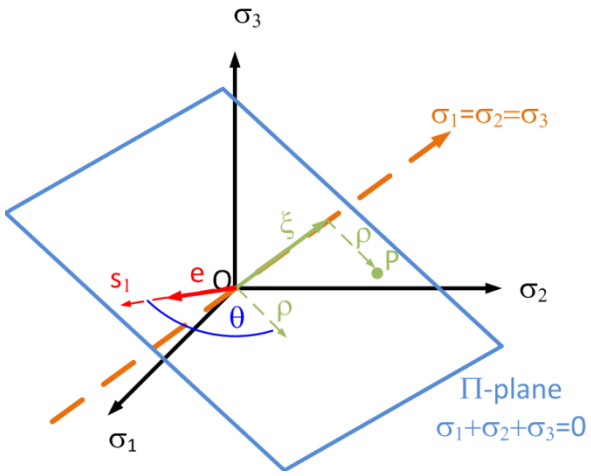

Fig. 0-1 Graphical representation of the stress state

It is difficult to design an experiment in which η and $\bar{\theta}$ are perfectly controlled and uncoupled. Indeed, for that to happen, a truly triaxial test would be necessary. One could imagine pulling a thick cube in three directions orthogonal to each face, but then, measurements on the specimen would be very tricky.

In practice, in most cases encountered in industrial contexts, metal sheets are used, so that plane stress states are predominant. In this case, only two principal stress values are non-zero, meaning that only one non-dimensional parameter can describe the stress state. Therefore, the stress triaxiality and the Lode angle parameter are not independent and are related in the following way:

$$\bar{\theta} = 1 - \frac{2}{\pi}\, a\cos\left[-\frac{27}{2}\eta\left(\eta^2 - \frac{1}{3}\right)\right] \tag{0.11}$$

Fig. 0-2 shows the graphical relationship between η and $\bar{\theta}$ in plane stress conditions for a range of stress triaxiality from uniaxial compression to equibiaxial tension.

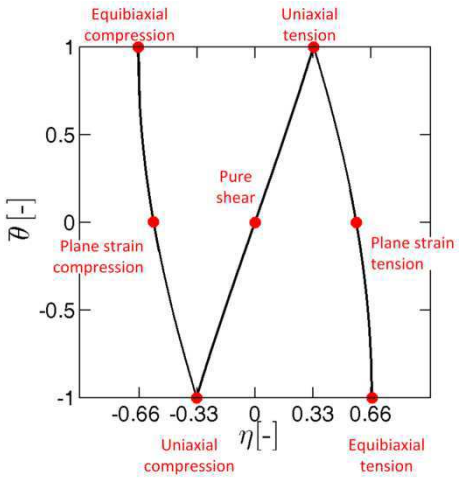

Fig. 0-2 Relationship between the stress triaxiality ratio and the Lode angle parameter in plane stress conditions.

2. Macroscopic aspects of ductile fracture

The influence of the stress state on ductility has been extensively documented. Tests have been performed on a variety of specimens allowing a wide range of stress triaxialities to be obtained. Among commonly used specimens are smooth and notched axisymmetric or plane strain specimens, and cracked specimens (Fig. 0-3).

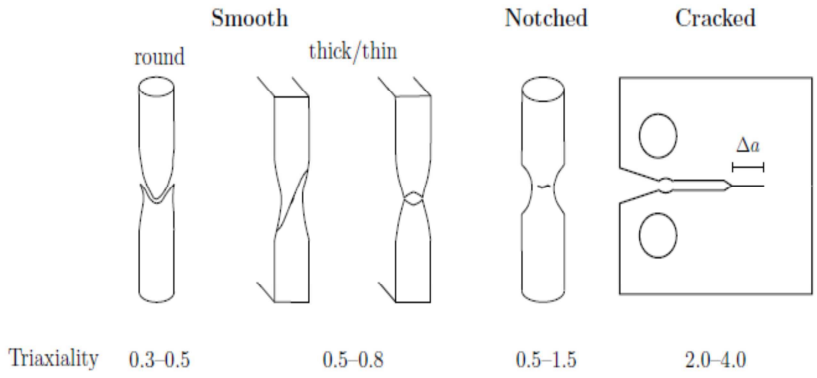

Fig. 0-3 Common specimens geometry (Benzerga and Leblond, [2])

Tests performed by Hancock and Mackenzie [3] on tensile notched steel specimens revealed a strong effect of the stress triaxiality on ductility, which decreases when the stress triaxiality increases. They used the results of Bridgman's analysis [4] to find a relationship

between the stress triaxiality and the fracture strain. Bridgman assumed a constant equivalent plastic strain across the minimum cross section:

$$\bar{\varepsilon}_f = 2\ln\left(\frac{r}{r_o}\right) \tag{0.12}$$

but a non-constant stress state, resulting in a stress triaxiality maximal on the specimen axis :

$$\eta = \frac{1}{3} + \ln\left(\frac{r}{2R} + 1\right) \tag{0.13}$$

Many further investigations have been performed. Most of them have confirmed the trend exhibited by Hancock and Mackenzie [3] for high levels of triaxialities. However, difficulties intrinsic to fracture tests and the need for more accurate failure prediction capability and improvements in the experimental and numerical fields have encouraged researchers to develop new techniques. For instance, Bridgman assumed a heterogeneous stress field in the gage section, but it is also the case for the strain field which, most of the time, is maximal in the bulk of the specimen. But most tests realized in the past (and some today) are monitored using extensometers or gauges, which only give an average information on the strain level on the surface of the gage section. To address these issues, several improvements have been brought on specimen geometries, experimental setups (multiaxial devices, full-field measurements) and post-processing.

Subsequently, hybrid experimental and numerical studies have become more and more frequent. This approach consists in performing a finite element analysis of the test yielding the strain and stress field in the bulk of the specimen. The onset of fracture is determined with the experiment (load peak, load drop, first crack visible during the test…). At the corresponding increment in the simulation, the point with maximal equivalent plastic strain is defined as the location of fracture and the local strain as the fracture strain $\bar{\varepsilon}_f$. Bao and Wierzbicki [5] have used this approach to investigate ductility of aluminum 2024-T351. They conducted a series of tests on several specimen geometries which allowed to explore a wide range of stress triaxialities, from -1/3 to 1. For negative stress triaxialities, they used upsetting specimens (Fig. 0-4a). For stress triaxialities from 0 to 0.4, they used butterfly specimens pulled through two pins in order to induce combined tension and shear in the gage section which featured various orientations with respect to the loading direction (Fig. 0-4b and c), and also central hole specimens for uniaxial tension (Fig. 0-4d). For stress triaxialities from 0.33 to 0.95, they used notched axisymmetric specimens with various radiuses (Fig. 0.4e). A few

years later, Barsoum and Faleskog [6] investigated ductile fracture of a mid-strength steel (Weldox 420) and a high-strength steel (Weldox 960), using a hybrid experimental and numerical analysis as well. To avoid misinterpretations due to the multiplication of specimen geometries, they designed a tubular specimen, featuring an external and internal circumferential notch, proportionally loaded under combined tension and torsion (Fig. 0-5). Different stress states were obtained by varying the proportions of tension and torsion. Fracture locuses obtained in both studies in the space of the equivalent plastic strain and the stress triaxiality are shown in Fig. 0-6a and Fig. 0-7a. For high values of triaxiality (higher than 0.4 for aluminum 2024-T351 and 0.8 for Weldow 420), the authors found a monotonic decrease of the ductility with stress triaxiality, again confirming known trends. Their studies however revealed a slope discontinuity in the fracture locus, occurring at a stress triaxiality of 0.4 for aluminum 2024 and 0.8 for Weldox 420. The locus of aluminum 2024-T351 even shows a complex evolution of ductility for low and negative ranges of stress triaxialities.

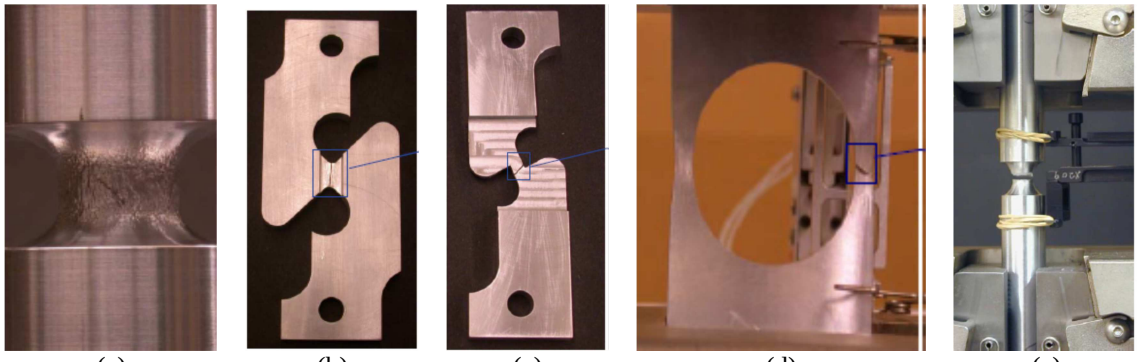

(a) (b) (c) (d) (e)

Fig. 0-4 Specimen geometries used by Bao and Wierzbicki [5]

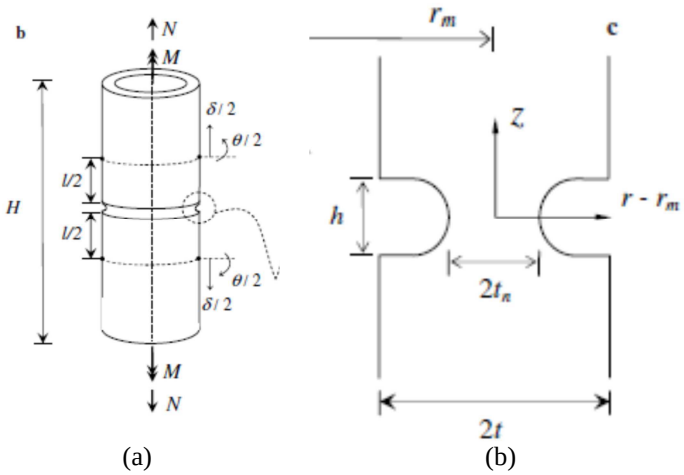

(a) (b)

Fig. 0-5 Tension-torsion specimen used by Barsoum and Faleskog [6]

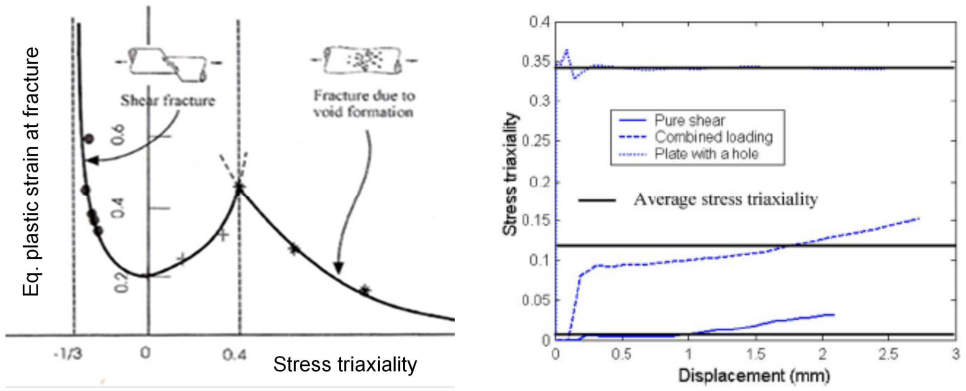

(a) (b)

Fig. 0-6 (a) Fracture locus of aluminum 2024-T351 (b) Variations of the stress triaxiality during tests at low and moderate stress triaxialities (Bao and Wierzbicki, [5]).

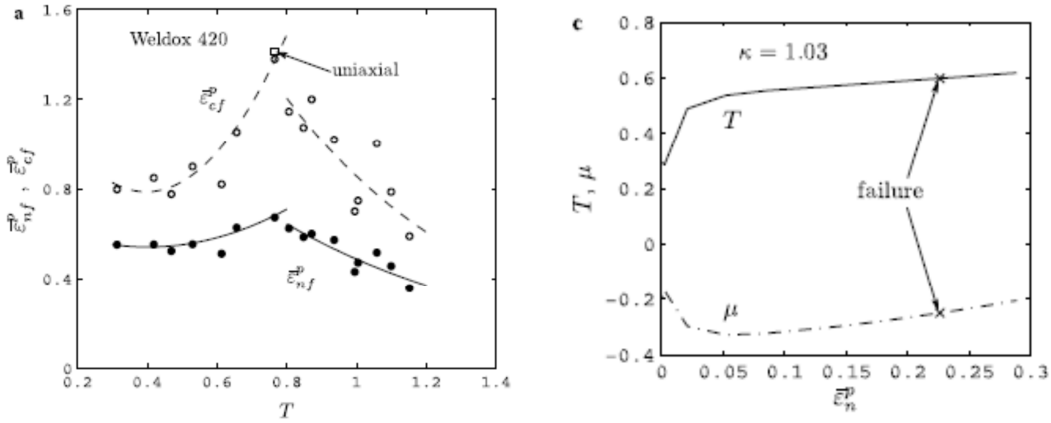

(a) (b)

Fig. 0-7 (a) Fracture locus of Weldox 420 (b) Variations of the stress triaxiality and the Lode parameter during tests at moderate stress triaxialities (Barsoum and Faleskog, [6])

Though simulations indicate the location where the plastic strain is maximal and where failure is thus likely to initiate, the choice of the pertinent values to plot on fracture locus remains tricky. Indeed, Bao and Wierzbicki [5] considered an average triaxiality, defined as:

$$\eta_{av} = \frac{1}{\bar{\varepsilon}_f} \int_0^{\bar{\varepsilon}_f} \eta d\bar{\varepsilon}_p \tag{0.14}$$

While Barsoum and Faleskog [6] considered the final value. However, the stress state is not necessarily constant throughout the test as can be seen in Fig. 0-6b and Fig. 0-7b. In particular, necking induces an increase in the stress triaxiality. It is not obvious to determine which value should be taken into account: indeed, considering an average triaxiality leads to an underestimation of this parameter, but if the loading path deviates substantially from a radial one, taking only the final value into account may not be pertinent either. Therefore, when conducting fracture tests and analyses, researchers are more and more careful to plot the

evolution of both the triaxiality and the Lode parameter all the way to fracture and to optimize the specimen geometry in order to limit the evolution of the stress state throughout the test (Dunand and Mohr [7]) (Fig. 0-8).

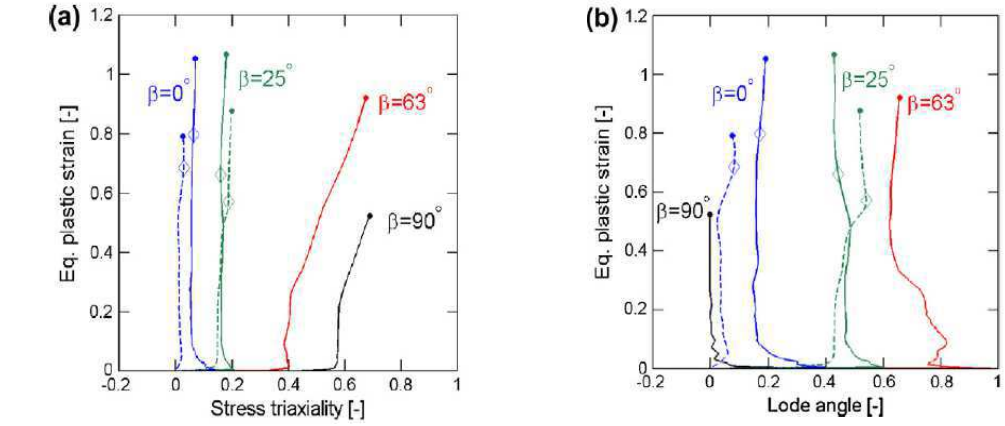

(a) (b)

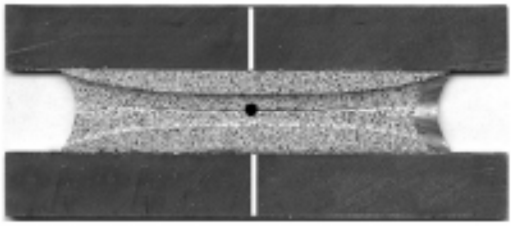

(c)

Fig. 0-8 (a) and (b) loading paths to fracture in the spaces $\{\eta, \bar{\varepsilon}_p\}$ and $\{\bar{\theta}, \bar{\varepsilon}_p\}$ (c) optimized butterfly specimen in combined shear and tension (Dunand and Mohr [7])

3. Microscopic aspects of ductile fracture

The stages of ductile failure have been studied since the 1970's. Their understanding has benefitted from the advent and progresses in optical microscopy, scanning electron microscopy (SEM), and, more recently, X-ray computed micro-tomography, which allows observations of the bulk of a specimen, provided that the latter is thin enough to be "X-ray transparent (500µm to 2mm, depending on the material density and beam energy) and the defects to be viewed are large enough with respect to the spatial resolution of the technique (about 1µm).

Metals are heterogeneous media: single or dual phase polycrystals containing ceramic or intermetallic particles or fine dispersoids. The brittle character of some inclusions and/or the

mismatch of their mechanical properties with those of the surrounding matrix make it the most favoured sites for void nucleation at large strains.

Ductile failure is a three stages process: voids nucleate, grow and coalesce. The presence of these voids is responsible for the dimpled aspect of fracture surfaces, very characteristic of ductile failure (Fig. 0-9).

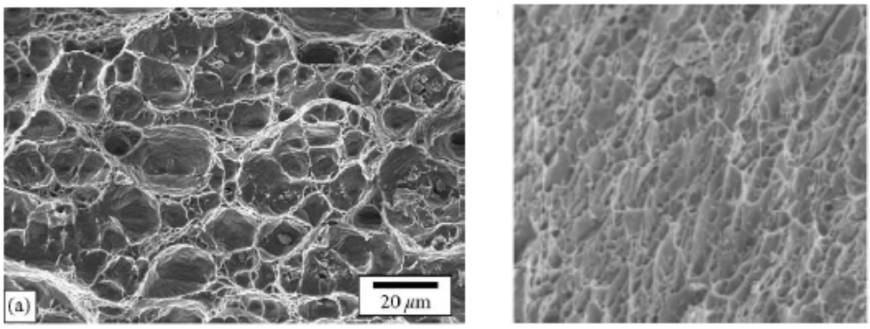

(a) (b)

Fig. 0-9 Ductile fracture surfaces of (a) an aluminum 2024-T351 sheet (Bron et al. [8]) and (b) a Weldox 420 tubular specimen with torsion-dominant loading (Barsoum and Faleskog [6])

The mechanisms of void nucleation depend on several factors, such as particle/matrix interface strength or stiffness mismatch, particle size, distribution, shape and orientation relative to the loading direction, matrix flow properties and stress state. Void nucleation occurs either by decohesion of the particle/matrix interface or by particle cracking (Argon and Im [9], Beremin [10], Babout et al. [11]) (Fig. 0-10). General trends have been observed: for instance, a matrix with high yield strength or hardening exponent will favor particle cracking, while a matrix with low yield strength or hardening exponent will favor particle/matrix decohesion. In some multiphase materials, damage can also initiate in a brittle phase or at the interface between two phases (Bugat [12], Maire et al. [13]). Sometimes, initial voids exist in the material.

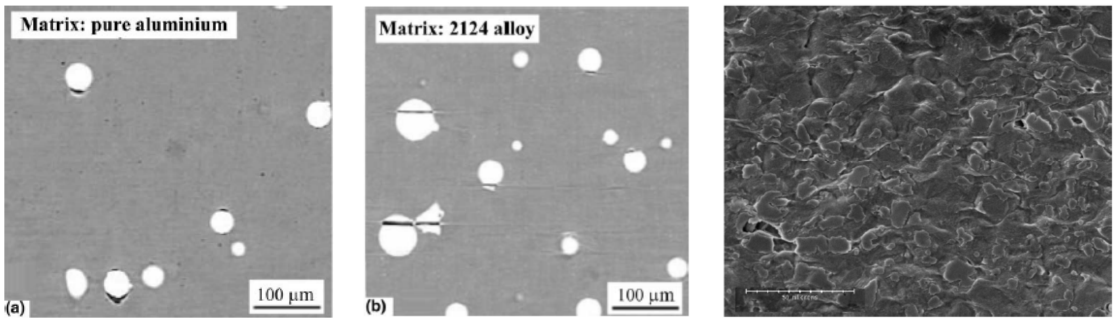

(a) (b) (c)

Fig. 0-10 Examples of (a) particle decohesion and (b) particle cracking in aluminum alloys with different matrix properties (Babout et al. [11]) (c) martensite fracture and ferrite/martensite decohesion in a DP steel (Maire et al. [13]).

During loading, voids grow and usually link. Different modes of coalescence exist. The most commonly observed are internal necking, where grown voids impinge each other, and void sheeting, in a micro-shear band (Fig. 0.11). Evidences of coalescence by void necklace formation have been reported by Benzerga [14] in steel containing elongated MnS inclusions and loaded in tension along the rolling direction.

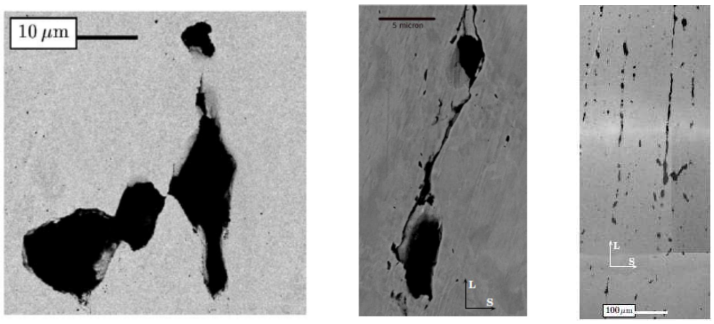

(a) (b) (c)

Fig. 0-11 Examples of coalescence by (a) internal necking (Benzerga et al. [15])(b) void sheeting (Benzerga [14]) (c) necklace columns (Benzerga [14])

The effect of the stress triaxiality on void growth and coalescence is strong and has been extensively investigated. At high levels of stress triaxiality (e.g. notched tensile or pre-cracked specimens), voids expansion is observed in most cases, and coalescence occurs by internal necking, while at low levels of stress triaxiality, voids evolve by rotation and distortion, and coalescence occurs by void-sheeting. The microstructural features also play an important role in void growth and coalescence. For instance, the anisotropy of initial void distribution of aluminum 2139 has been investigated by (Morgeneyer et al. [16]) using synchrotron radiation computed tomography, and was shown to have a strong influence on the toughness of the material. Thus, voids initially forming chains in the rolling direction grew and linked in the rolling direction when loaded in this direction, while, when loaded in the transverse direction, they also grew in the loading direction, but kept a high degree of alignment with the rolling direction. Besides, void sheeting coalescence is very much dependent on the void configuration and relative positions. This effect has been analyzed by Weck et al. [17] who conducted tensile experiments coupled with SEM and X-ray tomography on copper sheets in which they had introduced rows of artificial through holes, 10µm in diameter, equally spaced, and forming an angle of 15° or 45° with the loading direction. Coalescence occurred by internal necking between the holes for the 15° angle, while the 45° angle favoured intense shearing between the holes (Fig. 0-12).

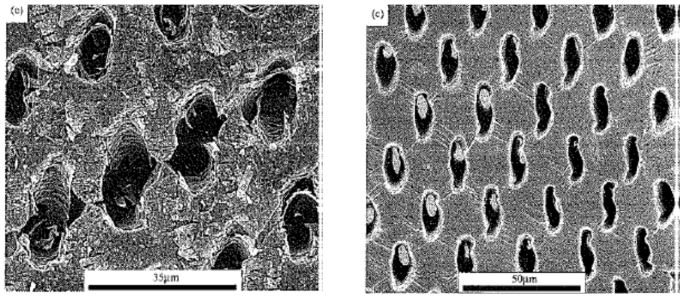

(a) (b)

Fig. 0-12 Coalescence by (a) internal necking and (b) void sheeting in copper sheets (Weck et al. [17])

Quantitative analyses of nucleation mechanisms have been undertaken. Among them, one can quote an estimate of the local stress necessary for void nucleation due to fracture of MnS inclusions by Beremin [10], based on experiments, finite element analysis and homogenization theory. Simultaneously, Le Roy et al. [18] estimated a strain for void nucleation due to Fe_3C in carbon steels. Smooth tensile bars were prestrained, restored, and then, reloaded to fracture. The nucleation strain was defined as the pre-strain necessary to cause a reduction in the fracture strain. A few years later, Pardoen and Delannay [19] used a similar technique, but also measured the effect of the stress triaxiality on the void nucleation strain in copper. Babout et al. [11] combined X-ray tomography and finite element analysis to establish a critical stress for particle cracking in aluminum matrixes artificially reinforced with spherical ceramic inclusions.

Void growth has been quantitatively analyzed as well. Marini et al. [20] measured cavities enlargement in a sintered-forged steel containing spherical alumina particles, using notched tensile specimens with various notch radii, pre-strained at different levels at room temperature and broken in liquid nitrogen. They estimated the void size on the fracture surface and found that the void growth rate increases exponentially with the stress triaxiality. Void dimension measurements have also been performed, using quantitative metallography or tomography. For instance, Chae and Koss [21] performed metallographic observations on polished sections of broken notched round bars, to assess the field of void area fraction using a fixed grid and determined the local area fraction at the onset of coalescence. Furthermore, they combined local measurements with finite element analysis to map the local strains and stress triaxiality to the local porosity. Maire et al. [13] performed non-proportional loading tests and X-ray tomography to quantify damage initiation and cavities rotation in aluminium matrixes artificially reinforced with hard spherical inclusions. They underlined the importance of taking into account the plastic strain hardening and the nucleation threshold in a damage model aimed at describing metal forming. Shen et al. [22] observed and quantified void

growth and coalescence in aluminum 6061 pre-cracked specimen via synchrotron laminography, and they identified the critical void volume fraction for coalescence, which they used in a micromechanical damage model. Ghahremaninezhad and Ravi-Chandar [23,24] conducted a series of interrupted tests on aluminum 6061 as well, for moderate stress triaxialities (smooth and notched tensile specimens) and low stress triaxialities (Arcan specimens loaded in combined tension/shear or compression/shear), to characterize damage in a multiscale framework. Analysis of polished and etched sections with optical microscopy showed signs of flow localization (Fig. 0-13). Changes in grain size at various stages were used to estimate local strain levels, which were shown to be much larger than those estimated from strains averaged over a characteristic specimen dimension and used to calibrate strain-to-failure criteria. Damage was found to occur quite late, at plastic strain levels of about 1 at the grain scale and the ductility was found to be a monotonic decreasing function of the stress triaxiality even in the range of low triaxiality, conversely to most macroscopic observations. More specifically, for low stress triaxialities, final failure was reduced to a narrow region within a localized deformation band.

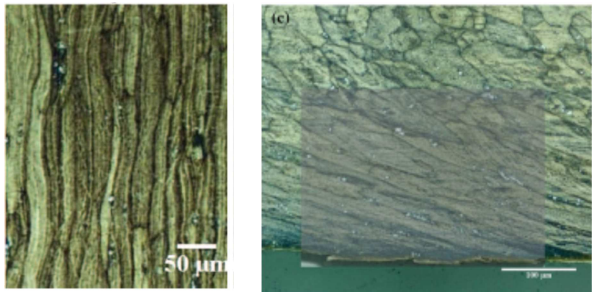

(a) (b)

Fig. 0-13 (a) Flow localization at the center of an aluminum 6061-T6 tensile notched specimen (Ghahremaninezhad and Ravi-Chandar [23]) (b) Shearing in an aluminum 6061-T6 Arcan specimen near the fracture surface (Ghahremaninezhad and Ravi-Chandar [24])

4. Modeling of ductile damage

The literature on ductile failure modeling is extremely large. Some models have been proposed for damage initiation, in particular, to distinguish between particle cracking and decohesion. Among them, Argon and Im [9] proposed a nucleation criterion depending on the interface strength and strength of the brittle particle, which they identified experimentally as was mentioned in section 3. Beremin [10] proposed an improved criterion which, assuming a homogeneous stress field in the particle and using Eshelby's theory for ellipsoidal inclusions,

accounts for plastic strain incompatibility and particle shape effect. Lee and Mear [25] found numerical solutions for stress concentrations factors K_I and K_P at the interface and in the particle; these factors depend on the particle aspect ratio, the remote stress triaxiality, the elastic modulii mismatch and the matrix flow properties. They found that as the stress triaxiality increases, particles tend to debond from the matrix rather than to crack; when the particle aspect ratio increases, the difference between K_P and K_I increases as well, an so does the ratio K_P/K_I, meaning that the larger the particle aspect ratio, the more likely the particle to crack.

A series of models of void growth have been proposed and improved in the past decades. Cockcroft and Latham [26] proposed an empirical model based on a void growth mechanism controlled by the maximum principal stress. Rice and Tracey [27] analyzed a spherical cavity in an infinite rigid and perfectly plastic medium, loaded axisymmetrically. They came up with an analytical expression of the void growth rate as a function of the stress triaxiality and the equivalent plastic strain rate.

$$\frac{dR}{R} = 0.283 \exp\left(\frac{3}{2}\eta\right) d\bar{\varepsilon}_p \tag{0.15}$$

Their model was modified by Thomason [28] to account for the change of shape of the initial spherical void. Later on, Gurson [29] proposed a homogenized behaviour of porous plastic metals based on a micromechanical study of a spherical cavity in an infinite rigid and perfectly plastic medium obeying J_2 plasticity and of yield stress σ_o, loaded axisymmetrically. Damage is accounted for via the void volume fraction f. The subsequent yield surface reads:

$$\frac{\bar{\sigma}_{eq}^{\,2}}{\sigma_o^{\,2}} + 2f\cosh\left(\frac{1}{2}\frac{tr(\boldsymbol{\sigma})}{\sigma_o}\right) - 1 - f^2 = 0 \tag{0.16}$$

Subsequent extensions of this model have been proposed. σ_o was replaced by a yield stress with the possibility of isotropic hardening. Tvergaard and Needleman [30] introduced two parameters q_1 and q_2 to account for the interaction between voids: it is the Gurson-Tvergaard-Needleman model (GTN). The dependency of these parameters on the geometry, the matrix flow properties and the ratio between yield stress and elastic modulus, has been investigated by Faleskog et al. [31].

Analytical methods for ductile damage analysis become rapidly limited due to the complexity of the criteria derivation. Indeed, simplifying assumptions are necessary. Therefore, such methods are not always suitable in most real cases. Numerical methods, such

as finite element analysis, prove very useful to describe more accurately ductile failure. In particular, unit cell models are much popular in this field. Such models consist in meshing a three dimensional box inside which lies a void with periodic boundary conditions. Mean stress components are prescribed on the boundary of the box, with control of both the triaxiality and the Lode angle parameter. Such analysis allows a verification of analytical solutions, gives a point of comparison with a model, or just brings an understanding of some damage processes, but, due to the periodic boundary conditions, does not capture the influence of a heterogeneous distribution of voids.

The Gurson model captures quite well the effects of the stress triaxiality on void growth, for high levels of triaxialities. However, comparison with unit cell computations such as Koplik and Needleman [32] revealed that the Gurson model predictions of void growth rates are inaccurate; for example the void growth for $\eta = 1/3$ is overestimated (Fig. 0-14). Another limitation is its unability to predict shear localization and fracture under low triaxiality, unless void nucleation is introduced. Thus, for pure shear, the Gurson model predicts no damage change, which is in contradiction with unit cell studies and experimental observations. Zhang et al. [33] and Barsoum and Faleskog [34] conducted unit cell studies, under different stress states and found that not only does damage evolve under low triaxiality, but also, the Lode angle parameter has a strong effect on the rate of void expansion and coalescence, and on strain localization, especially the stress triaxiality is low (Fig. 0-15). Hence a recent extension of the GTN model was proposed by Nahshon and Hutchinson [35] who introduced the Lode parameter to represent damage growth under shear-dominated stress states. This efficient but phenomenological approach has been criticized since the damage parameter, *f*, loses its physical meaning. Tomography observation of arrested cracks in Kahn tear test samples Morgeneyer and Besson [36] have shown that the flat to slant transition and slant propagation of the crack result from a change in micromechanisms from high stress triaxiality to shear coalescence. The incorporation in the GTN model of a nucleation term controlled by the Lode parameter of the plastic strain rate tensor allows to account for this transition and to reproduce the slant propagation of the crack in FE simulations.

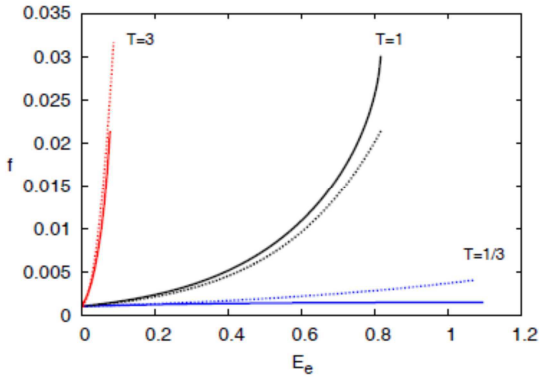

Fig. 0-14 Evolution of the void volume fraction with respect to the deformation for different values of stress triaxiality. Comparison between the Gurson model (dashed line) and unit cell calculations of Koplik and Needleman [32] (plain line). Source Benzerga and Leblond [2]

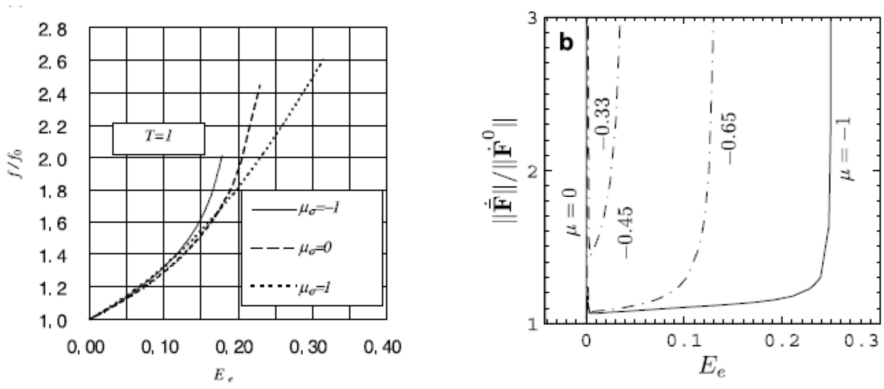

(a) (b)

Fig. 0-15 Unit cell calculations : (a) evolution of the void volume fraction with respect to the deformation for a fixed triaxiality and different values of the Lode parameter (Zhang et al. [33]) (b) evolution of a localization indicator with respect to the deformation for a fixed triaxiality and different values of the Lode parameter (Barsoum and Faleskog [34]).

The Gurson model also assumes initially spherical voids, which remain spherical throughout the loading, which, in practice, is hardly true for stress triaxiality around 1.5. Gologanu et al. [37,38,39] derived a model which accounts for void shape effects (GLD model). It assumes axisymmetric prolate or oblate ellipsoidal cavities loaded axisymmetrically. An initially spherical cavity tends to become prolate at low triaxiality and oblate at high triaxiality (Fig. 0-16a). In comparison with the Gurson model, it does not overestimate the void growth rate when $\eta = 1/3$ (Fig. 0.16b).

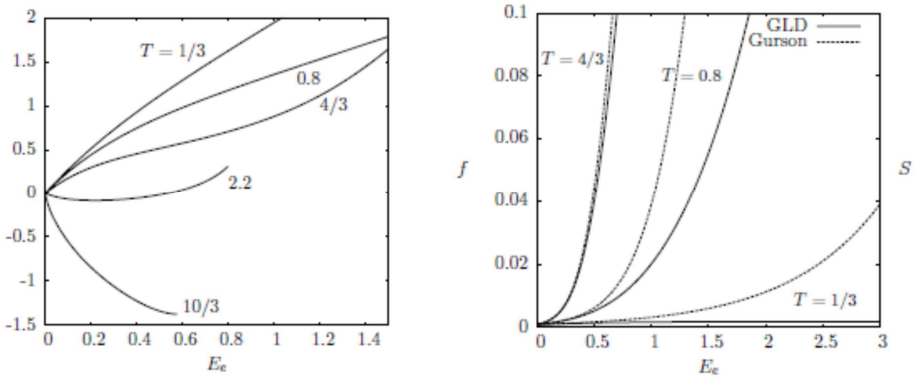

(a) (b)

Fig. 0-16 (a) Shape variation of an initially spherical cavity predicted by the GLD model (b) Evolution of the void volume fraction with respect to the deformation for various stress triaxialities; comparison between the GLD and Gurson model (Benzerga and Leblond [2])

Benzerga and Besson [40] proposed another extension of the Gurson model to account for plastic anisotropy, while combined plastic anisotropy and void shape effects were implemented by Keralavarma and Benzerga [41,42] for non-axisymmetric loading.

One can note that models such as Rice and Tracey [27] or Gurson [29] and its extensions do not take into account the presence of a particle within the voids. Bordreuil et al. [43] modified the Rice and Tracey [27] void growth model to take into account the contact between an inclusion and the matrix. In connection with a specific plastic potential, their analysis led to a compressible plastic constitutive law, which predicts void growth even at zero stress triaxiality.

Models resulting from homogenization techniques have been proposed. Aravas and Ponte-Castañeda [44] developed a model for the viscoplastic behaviour of a porous medium that predicts the anisotropy induced by the changes in the shape and orientation of the voids. Danas and Ponte-Castañeda [45] derived a model dependent on the porosity and average pore shape (Fig. 0-18 and Fig. 0-19).For high stress triaxialities, their model predicts void growth, and a decrease evolution in ductility as the stress triaxiality rises. The stress versus strain curve features a peak load, and a subsequent decrease. The Lode parameter in this range has a weak influence. For low stress triaxialities, an abrupt collapse of the voids is predicted, along with a simultaneous strain localization and a sudden drop in the material load-carrying capacity. The strain at the onset of this unstability is found to be highly dependent on the Lode parameter. Such softening is not predicted by Nahshon and Hutchinson's extension of the Gurson model [35] and was criticized by Hutchinson and Tvergaard [46] who assert that

void collapse will, on the contrary, produce larger localization strains, due to the surface contact of collapsed voids.

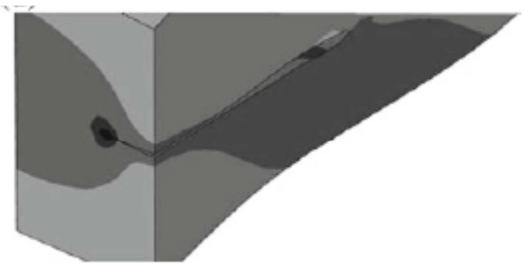

Fig. 0-17 Collapse of an initially spherical void predicted by unit cell calculation for shear-dominant loading (Nielsen et al. [47])

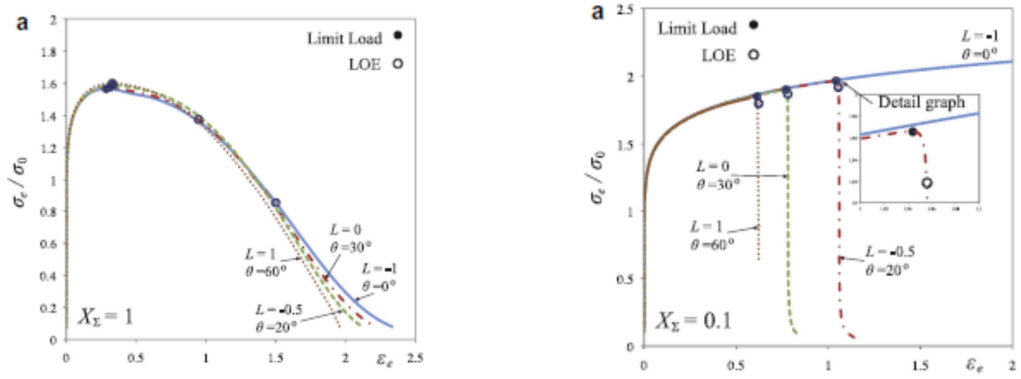

(a) (b)

Fig. 0-18 Influence of the Lode parameter on the stress-strain curve for a fixed value of stress triaxiality (a) high triaxiality (b) low triaxiality (Danas and Ponte-Castañeda [45])

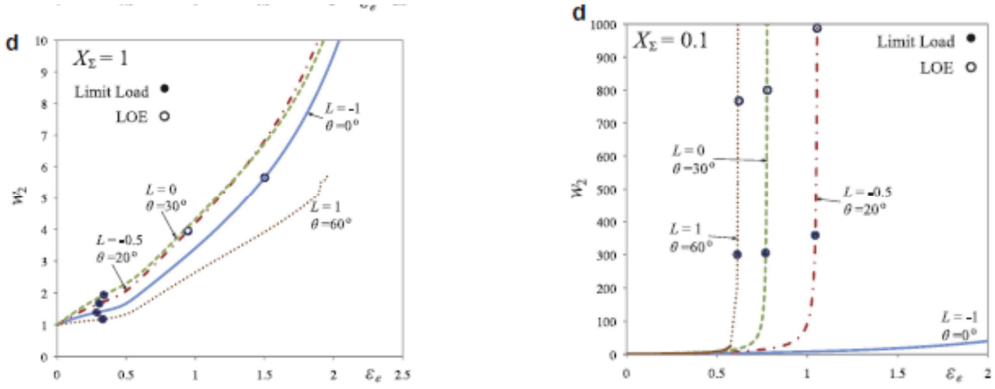

(a) (b)

Fig. 0-19 Influence of the Lode parameter on void aspect ratio curve for a fixed value of stress triaxiality (a) high triaxiality (b) low triaxiality (Danas and Ponte-Castañeda [45])

The necessity of accounting for the Lode parameter in ductile failure is now accepted. Besides models resulting from micromechanics or homogenization, phenomenological models have been developed as well in this direction. For instance, Gao et al. [48] proposed an elasto-plastic model depending on I_1, J_2 and J_3, and extended the GTN model applicability by

replacing the Mises equivalent stress by the new equivalent stress, to include the effect of the third invariant on ductile failure. Bai and Wierzbicki [49] proposed a model of metal plasticity and fracture with pressure and Lode dependence, which allows to distinguish between materials that depend weakly or strongly on I_1 or the Lode parameter.

Bai and Wierzbicki [49] showed the applicability of the Mohr-Coulomb (MC) [50,51] fracture criterion, extensively used in soil mechanics, to ductile fracture of uncracked bodies. This criterion accounts for the dependency of failure to both the triaxiality and the Lode angle parameter. According to the MC criterion, fracture occurs when the combination of normal stress σ_n and tangential stress τ on a plane of normal **n** arbitrarily cutting a material element reaches a critical value:

$$\max_{\mathbf{n}} \tau + c_1 \sigma_n = c_2 \tag{0.17}$$

which yields:

$$\sqrt{1+c_1^{\,2}}\left(\sigma_1-\sigma_3\right)+c_1\left(\sigma_1+\sigma_3\right)=2c_2 \tag{0.18}$$

One can recognize the Tresca equivalent stress $\left(\sigma_1-\sigma_3\right)$ in Eq. (0.18). Using successive transformations (Bigoni and Piccolroaz [52]) and the hardening law, Bai and Wierzbicki [49] expressed this stress-based criterion in the mixed stress-strain space $\left\{\bar{\varepsilon}_f,\eta,\bar{\theta}\right\}$. This criterion was extended by Mohr and Marcadet [53] to the Hosford-Coulomb criterion (HC) by replacing the Tresca stress in the MC model by the Hosford equivalent stress in order to improve its predictions.

5. Goal of the study

As mentioned in the previous sections, the effect of the stress state on ductile failure has kept many researchers busy for several decades. Until recently, experimental studies focused on high triaxiality levels and very little was said of the Lode parameter. Controlling both the stress triaxiality and the Lode parameter experimentally is tricky, especially as most tests are conducted in a plane stress context. However, numerical and theoretical investigations showing that the Lode parameter should be taken into account when modeling ductile fracture, especially for low levels of stress triaxiality, have drawn the attention on the necessity of monitoring the history of both these parameters when constructing a material fracture locus.

While the possibilities given by unit cell models are very rich, the comparison between the many modeling approaches that exist in this field and the experiments is challenging, at the macro scale where accurate quantitative fracture prediction is not always achieved, and at the micro scale, where mechanisms differ according to the microstructural features.

The work that has been undertaken in this thesis aims at contributing to a better understanding of ductile damage mechanisms in metallic materials. A contribution is the design of a specimen for fracture testing of bulk materials that will allow a wide range of stress states to be obtained, the effect of the stress state on the ductility to be investigated and fracture criteria to be calibrated, and at the microscopic scale, the effect of the stress state on damage mechanisms to be clarified.

The first chapter will present thoroughly the experimental protocol that was developed and applied successfully to 36NiCrMo16 steel to investigate, at the macroscopic scale, the influence of the stress state on the material ductility. In the second chapter, the same protocol will be applied to obtain the fracture locus of aluminum alloy 2024-T351 for proportional and non-proportional loading. This fracture locus will be compared to that obtained by Bao and Wierzbicki [5] and extensively quoted in literature. A recently-proposed shear localization criterion, the Hosford-Coulomb criterion (Mohr and Marcadet [53]), will be calibrated and validated for each material. The third chapter will investigate the damage mechanisms for stress triaxialities lower than 1/3, for 36NiCrMo16 steel and 2024-T351 aluminum alloy, by means of microscopy on tests to fracture, interrupted tests or in-situ tests in a SEM. Finally, the fourth chapter will bring insight on the damage mechanisms of aluminum 2024-T351 analyzed by X-ray laminography at intermediate stress triaxialities, by means of an in-situ test performed on a CT specimen. The mechanisms highlited in the third and fourth chapter justify the use of a shear localization criterion such as the Hosford-Coulomb criterion.

I. Determination of the Effect of Stress State on the Onset of Ductile Fracture through Tension-Torsion Experiments

---

In this chapter, a tubular tension-torsion specimen is proposed to characterize the onset of ductile fracture in bulk materials at low stress triaxialities. The specimen features a stocky gage section of reduced thickness. The specimen geometry is optimized such that the stress and strain fields within the gage section are approximately uniform prior to necking. By applying different combinations of tension and torsion, the material response can be determined for stress triaxialities ranging from zero (pure shear) to about 0.58 (transverse plane strain tension), and Lode angle parameters ranging from 0 to 1. The relative displacement and rotation of the specimen shoulders as well as the surface strain fields within the gage section are determined through stereo digital image correlation. Multi-axial fracture experiments are performed on a 36NiCrMo16 high strength steel. A finite element model is built to determine the evolution of the local stress and strain fields all the way to fracture. Furthermore, the newly-proposed Hosford-Coulomb fracture initiation model [53] *is used to describe the effect of stress state on the onset of fracture.*

Recent research on ductile fracture emphasizes the effect of the third stress invariant on the onset of ductile fracture in metals. Examples include the recent studies by Barsoum and Faleskog [6], Nahshon and Hutchinson [35], Bai and Wierzbicki [49] and Nielsen and Tvergaard [54] which all hypothesize on the dependence of the equivalent plastic strain to fracture on the third stress tensor invariant in addition to the stress triaxiality. Micromechanical demonstrations of the effect of the Lode parameter have been presented among others by Barsoum and Faleskog [34], Danas and Ponte Castaneda [45] and Dunand and Mohr [55].

At this stage, it is still very difficult to draw concrete conclusions on the effect of the Lode angle on the onset of fracture based on experiments. Reliable experiments characterizing the effect of stress state on the onset of ductile fracture are difficult to achieve, in particular due to necking prior to the onset of fracture in thin-walled specimens. Hybrid experimental-numerical techniques have been developed to address this issue. Mohr and Henn [56] subjected flat butterfly-shaped specimens to combined tension and shear loading. Due to the heterogeneity of the stress and strain fields in the specimen gage section, they made use of a finite element model to determine the stress and strain histories at the location of fracture initiation. This technique has been developed further by Teng et al. [57] and Dunand and Mohr [7] by optimizing the specimen shape to reduce experimental errors, and through the use of more advanced plasticity models for the identification of the loading path to fracture. In the case of sheet materials, the butterfly testing technique requires a local reduction of the initial specimen thickness. This machining procedure may affect the mechanical properties of the specimen material (see Mohr and Ebnoether, [58]) which adds to the uncertainty in the experimental results. Flat notched specimens provide a robust alternative to this technique to characterize the fracture response at stress triaxialities above 0.33. It is now common practice to take a hybrid experimental-numerical approach to analyze notched tensile experiments (e.g. Dunand and Mohr, [59]). Similarly, other sheet specimen geometries are being used to cover different stress states. The maturation of digital image correlation techniques (e.g. Bornert et al., [60], Sutton et al., [61]) also contributed significantly to the success of hybrid experimental-numerical approaches.

In the case of bulk materials, tubular specimens can be extracted to perform combined tension-torsion experiments. The first experiments of this type have been performed already one century ago. The most prominent are those by Taylor and Quinney [62] which were instrumental in the development of multi-axial plasticity models of metals. Taylor and

Quinney [62] used rather slender thick-walled tubes, while more stocky thin-walled tubes are used today. For example, Nouailhas and Cailletaud [63] used 1mm thick tubes with an inner diameter of 14mm and a free length of 24mm to investigate the tension-torsion response of single crystal superalloys. Zhang and Jiang [64] studied the propagation of Lüders bands in 1045 steel using a 1.1mm thick tension-torsion specimen of an inner diameter of 20.2mm and a gage section length of 25.4mm. Khan et al. [65,66] used a tubular specimen of 12.7mm inner diameter with a 50.8mm long, 1.4mm thick gage section to perform tension-torsion experiments on Al6061-T6511 and annealed Al-1100.

Multi-axial stress states in tubular specimens may also be achieved through combinations of tension and internal pressure. While the above experimentalists used tension-torsion experiments for plasticity characterization, tension-internal pressure experiments have been performed to study both the plasticity and ductile fracture of metals. For example, Kuwabara et al. [67] tested Al 5154-H112 tubes of 76.3mm outer diameter and 3.9mm wall thickness under tension and internal pressure. Korkolis et al. [68] subjected Al-6061-T6 tubes to internal pressure and axial load to investigate the plasticity and fracture under biaxial loading. Their specimens featured a nominal diameter of 51mm, a wall thickness of 1.65mm and a test section length of 229mm.

Shear buckling often limits the validity of tension-torsion experiments to moderate strains. In order to test engineering materials all the way to fracture under combined tension-torsion loading, Barsoum and Faleskog [6] introduced a symmetric circumferential notch into the tube wall, thereby concentrating plastic deformation into a very narrow region. To investigate the ductile fracture of Weldox steels, they used a nominal specimen diameter of 24mm, a wall thickness of 1.2mm within the notched section and of 3.2mm outside the notch. The notch radius was only 0.5mm, which creates substantial radial stresses when tension is applied. Their experimental program covered stress triaxialities (at the onset of fracture) from about 0.3 to 1.2. Another strategy for preventing shear buckling is to shorten the specimen gage section. This approach has no obvious negative effect when applying torsion only, but it changes the stress state in tension. For pure tension applied to the specimen boundaries, the stress state in the tube walls is no longer uni-axial tension, but close to transverse plane strain tension instead, as circumferential deformation is prohibited by the boundary conditions in stocky tension-torsion specimens.

Lindholm et al. [69] designed a stocky tubular specimen for dynamic torsion testing of metals. It featured an inner diameter of 12.9mm, a gage section length of 3.1mm and a gage

section thickness of 0.8mm. Note that the choice of a very short gage section in a specimen for dynamic testing is not only driven by stability considerations, but also necessary to ensure locally quasi-static loading conditions. Gao et al. [70] modified the Lindholm specimen to perform static fracture experiments on Al 5053-H116 (extracted from plate stock). The specimen gage section was 2.5mm long and 0.75mm thick. The tube inner diameter was 13.1mm, the outer diameter 25.4mm. In a follow-up paper, Graham et al. [71] show that this experimental technique covers a range of stress triaxiality from 0 to 0.6. A very recent study on the ductile failure of aluminum 60161-T6 under combined tension and shear has been completed by Haltom et al. [72]. They used a tubular specimen of a uniform inner diameter of 44.3mm and a wall thickness of 1mm within the 10mm long test section.

In this chapter, a stocky tubular specimen is presented for characterizing the onset of fracture in bulk materials at low stress triaxialities. Combined tension-torsion fracture experiments are performed on an initially isotropic high strength steel. Using a hybrid numerical-experimental procedure, the loading paths up to the onset of fracture are determined and presented in the space of stress triaxiality, Lode angle parameter and equivalent plastic strain. These results are subsequently used to identify the parameters of an Hosford-Coulomb fracture initiation model.

1. Specimen design

1.1. Specimen geometry

Fig. I-1 shows a sketch of the axisymmetric specimen geometry proposed for the testing of metals under combined tension and torsion. The specimen geometry is characterized by five parameters (Fig. I-1b): the inner diameter D, the gage section thickness t, the gage section height h, the wall thickness e of the shoulder region, and the fillet radius a (Fig. I-1b). The main considerations in specifying the specimen dimensions are:

(1) the maximum axial force and torque may not exceed 100kN and 600Nm, respectively; this limitation along with the availability of suitable specimen clamps led to the choice of D=20mm.

(2) the thickness-to-diameter ratio, t/D, needs to be small to reduce the gradients in the stress and strain fields along the radial direction; a minimum thickness of t=1mm is

chosen in view of uncertainties in the experimental results associated with dimensional inaccuracies in the initial specimen geometry (for example, a machining tolerance of $\pm 50 \mu m$ equates to an uncertainty of 5% in the reported average stress fields)

(3) the shoulder-to-gage section thickness ratio, e/t, needs to be sufficiently large to prevent the plastic deformation of the shoulder region; a shoulder thickness of $e = 2\ mm$ is chosen to prevent the plastic deformation of the shoulders even for high strain hardening materials.

(4) the height-to-thickness ratio, h/t, needs to be small to prevent buckling under torsion;

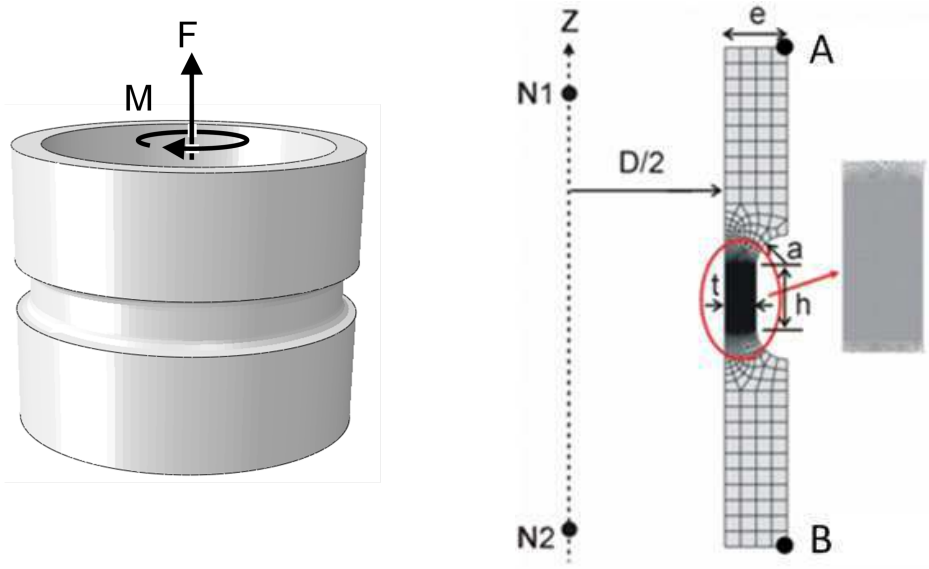

(a) (b)

Fig. I-1 (a) Schematic of specimen geometry, (b) geometry parameters and FE mesh.

In addition, the results from a finite element study revealed that

(5) the greater the height-to-thickness ratio, h/t, the smaller the radial gradient in stress triaxiality (Fig. I-2a). Based on (4) and (5), a gage section height of $h = 2\ mm$ is chosen.

(6) The greater the fillet radius a, the more uniform the stress fields. However, a should be small to keep the effective buckling length short. We chose a radius of $a = 1mm$; for this radius, there is no noticeable notch effect when tension is applied to the specimen, i.e. the radial stresses are still negligibly small as compared to the axial and circumferential stress components (Fig. I-2b).

Fig. I-4c provides a summary of the final specimen dimensions. The overall length of the specimens is 90mm with a free length between the specimen clamps of 40mm.

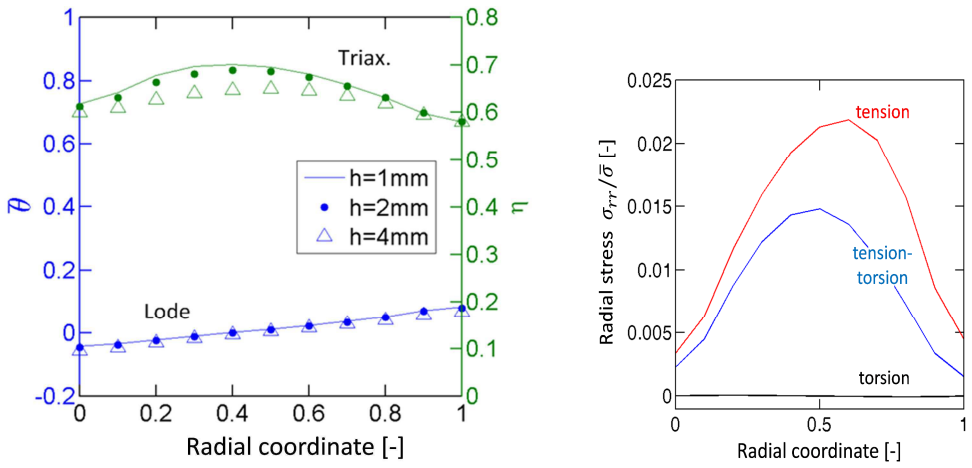

(a) (b)

Fig. I-2 Stress distribution inside the gage section prior to necking: (a) Influence of the gage section height *h* on stress state uniformity along the radial direction (b) variation of the radial stress along the radial direction. A radial coordinate of 0 and 1 corresponds to the inner and outer gage section surface, respectively. Note that the free surface condition $\sigma_{rr} = 0$ appears to be only approximately fulfilled due to the normalized ordinate axis. These profiles are obtained by FE calculations, using a Levy – von Mises material and a isotropic Swift hardening law, with a hardening exponent of 0.2.

1.2.Analytical estimate of the achievable stress states

Given the stockiness of the specimen gage section, the achievable stress states are computed assuming zero plastic circumferential strain. Furthermore, plane stress conditions (along the radial direction) are assumed. For a Levy-von Mises material, the flow rule yields

$$\sigma_{\theta\theta} = 0.5\sigma_{zz}. \tag{1.1}$$

The Cauchy stress tensor may thus be written as

$$\boldsymbol{\sigma} = \sigma \mathbf{e}_Z \otimes \mathbf{e}_Z + 0.5\sigma \mathbf{e}_\Theta \otimes \mathbf{e}_\Theta + \tau(\mathbf{e}_Z \otimes \mathbf{e}_\Theta + \mathbf{e}_\Theta \otimes \mathbf{e}_Z) \tag{1.2}$$

where σ denotes the stress along the $\mathbf{e}_Z$-direction, and τ is the shear stress in the $(\mathbf{e}_Z, \mathbf{e}_\Theta)$-plane.

The stress state is characterized through the stress triaxiality and the Lode angle parameter, which were defined in (0.8), (0.10) and (0.11), in the Introduction. The stress state in the specimen gage section is controlled by the ratio of torsion and axial loading. Based on the specimen diameter D, the axial force F and the torque M, the biaxial loading angle β is defined as

$$\tan\beta = \frac{FD}{2M} \cong \frac{\sigma}{\tau}. \tag{1.3}$$

Combining Eqs. (0.8), (0.9), (0.10) and (1.3), the stress triaxiality and the Lode angle parameter can be expressed in terms of the biaxial loading angle,

$$\eta = \frac{1}{\sqrt{3}} \frac{\tan\beta}{\sqrt{\tan^2\beta + 4}} \tag{1.4}$$

$$\bar{\theta} = 1 - \frac{2}{\pi} a\cos\left(\frac{6\sqrt{3}\tan\beta}{\left(\tan^2\beta + 4\right)^{3/2}} \right). \tag{1.5}$$

The Lode angle parameter is plotted as a function of the stress triaxiality in Fig. I-3, while β is used as curve parameter. Note that this relationship between the Lode angle and the stress triaxiality is only valid for plane stress conditions. For $\beta = 0°$ (torsion only), the stress state corresponds to pure shear which is characterized by $\eta = 0$ and $\bar{\theta} = 0$. The same Lode angle parameter value is achieved for β=90° (tension only) where the stress state corresponds to transverse plane strain tension. A uniaxial stress state ($\eta = 0.33$ and $\bar{\theta}$=1) prevails for combined tension-torsion loading at $\beta \cong 55°$.

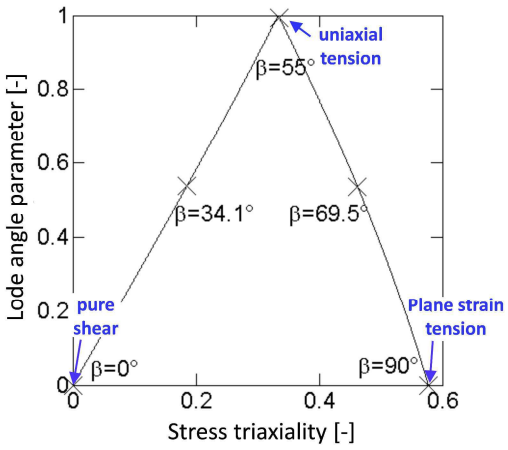

Fig. I-3 Theoretical range of stress states achievable with the current geometry.

2. Experiments

2.1. Material

All specimens are extracted from an annealed 30mm diameter bar of the high strength steel 36NiCrMo16. Tab. I-1 shows the chemical composition as provided by the manufacturer

ThyssenKrupp. Large strain compression tests on 13mm-large cubes extracted along the bar axis and the transverse direction revealed no noticeable anisotropy in the material behavior at the macroscopic level.

C	Mn	Si	S	P	Cr	Ni	Mo	Cu	Al
0.37	0.41	0.25	0.016	0.011	1.72	3.74	0.28	0.25	0.03

Tab. I-1 Chemical composition of 36NiCrMo16 provided by ThyssenKrupp Steel (in weight %)

2.2.Experimental procedure

A servo-hydraulic axial/torsion and internal pressure loading frame (TEMA Concept, France) is used to perform all experiments (Fig. I-4a). The vertical and rotational actuators cover a range of ±100kN and ±600Nm, respectively. The specimens (part #1 in Fig. I-4b) are attached to the testing machine using annular pressure clamps (part #3 in Fig. I-4b). The mechanical connection between the testing machine and the specimen is established through tangential frictional stresses between the contact surfaces only. For this, a female connector matching the exact dimensions of the specimen shoulder region is rigidly connected to the testing machine (part #2 in Fig. I-4b). The alignment of the upper and lower connector is verified prior to testing using a short tube of constant wall thickness. After verifying the alignment and degreasing all surfaces, the specimen is inserted in the lower and upper connectors. Due to the tight fit of the specimen into the testing machine (no longer movable by hand), both actuators can already be put into force control mode to avoid any straining of the specimen gage section during set-up. Subsequently, the outer pressure ring is tightened (part #4 in Fig. I-4b) to apply a normal pressure to all connecting surfaces. Note that the inner piece of the female connectors is also rigidly connected to the machine, i.e. the shear stresses are transmitted between the specimen and the testing machine through both the inner and outer specimen surfaces, thereby reducing the maximum shear stresses in the mechanical connections by about a factor of two.

Throughout the experiments, the biaxial loading angle is kept constant using different control settings:

- For $\beta = 0°$, the rate of rotation is prescribed (0.019°/s), while operating the vertical actuator under force control ($F = 0$).

- For $0 < \beta \leq 55°$ (shear-dominated), the rate of rotation is prescribed (0.019°/s), while the axial position is incrementally adjusted such that β remains constant.
- For $55° < \beta < 90°$ (tension-dominated), the axial displacement rate is prescribed (0.002mm/s), while the rotation is incrementally adjusted such that β remains constant.
- For $\beta = 90°$, the axial velocity is prescribed (0.002mm/s), while operating the rotational actuator under torque control ($M = 0$).

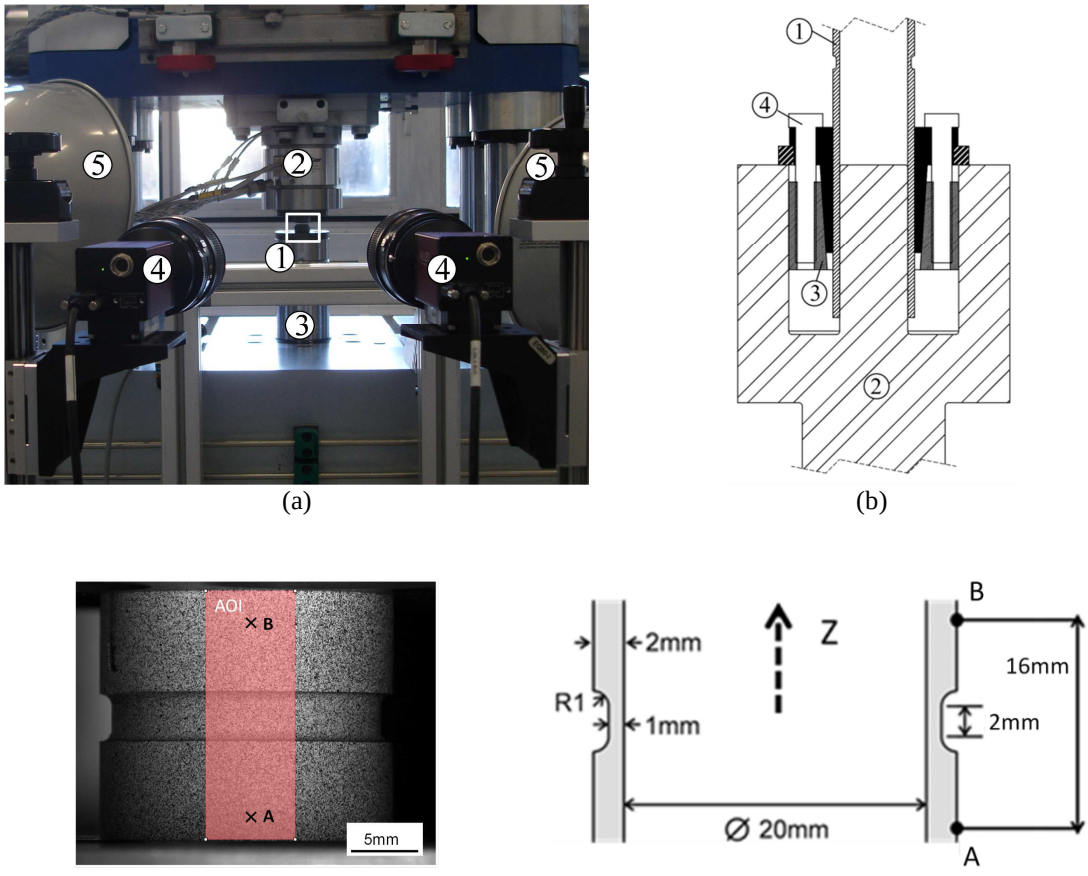

(a) (b)

(c) (d)

Fig. I-4 (a) Photograph of the experimental setup showing 1-specimen, 2-axial/torsion load cell, 3-piston, 4-cameras, 5-lighting, (b) clamping device (c) left camera view of the specimen with DIC area of interest (AOI) highlighted, (d) specimen dimensions.

2.3. Displacement and strain measurement

The displacement fields within the gage section and a part of the shoulder regions are measured using stereo Digital Image Correlation (DIC). A thin layer of matt white paint is applied onto the specimen surface along with a black speckle pattern (Fig. I-4c). Two digital cameras Pike F505B 2452x2054 equipped with 90mm macro lenses (Tamron, model SP Af90mm F/2.8 Di) are used to monitor the specimen surface from two different radial perspectives at a frequency of 1Hz. The camera sensors are positioned at a distance of about 800mm from the specimen surface with an F11 aperture to ensure sufficient depth of field for measuring large rotations. The relative position of the cameras and the respective focal lengths are identified from preliminary measurements on a rigid target. The displacement field is computed based on the acquired images using the VIC3D software (Correlated Solutions) assuming an affine transformation of a 21x21 pixel subset (with $24\mu m$ per pixel).

Based on the measured initial shape, a cylindrical coordinate system $(\mathbf{e}_R, \mathbf{e}_\Theta, \mathbf{e}_Z)$ is established such that the $\mathbf{e}_Z$ -vector coincides with the specimen axis (Fig. I-4d). The initial position of a point on the specimen surface is then given by the position vector

$$\mathbf{X} = R\mathbf{e}_R[\Theta] + Z\mathbf{e}_Z , \tag{1.6}$$

while its current position on the deformed specimen surface reads

$$\mathbf{x} = r\mathbf{e}_R[\theta] + z\mathbf{e}_Z . \tag{1.7}$$

The functions

$$r = r[R, \Theta, Z] \tag{1.8}$$
$$\theta = \theta[R, \Theta, Z] \tag{1.9}$$
$$z = z[R, \Theta, Z] \tag{1.10}$$

are obtained from stereo digital image correlation.

The DIC position measurements serve two purposes. Firstly, the relative motion of two points A and B positioned on the respective upper and lower specimen shoulder (Fig. I-4d) is determined,

$$\Delta U(t) = z_A(t) - z_B(t) , \tag{1.11}$$
$$\Delta\theta(t) = \theta_A(t) - \theta_B(t) . \tag{1.12}$$

Secondly, the surface strain field is computed from the position measurements. Re-writing the vector of the current position in terms of the base vectors associated with the initial configuration,

$$\mathbf{x} = x_R \mathbf{e}_R[\Theta] + x_\Theta \mathbf{e}_\Theta[\Theta] + x_z \mathbf{e}_Z \,, \tag{1.13}$$

with

$$x_R = r\cos(\theta - \Theta), \quad x_\Theta = r\sin[\theta - \Theta] \quad \text{and} \quad x_Z = z \tag{1.14}$$

the surface deformation gradient is given as

$$\mathbf{F} = \begin{bmatrix} \frac{1}{R}\left(\frac{\partial x_\Theta}{\partial \Theta} + x_R\right) & \frac{\partial x_\Theta}{\partial Z} \\ \frac{1}{R}\frac{\partial x_Z}{\partial \Theta} & \frac{\partial x_Z}{\partial Z} \end{bmatrix}. \tag{1.15}$$

The nominal strain tensor is then computed as

$$\boldsymbol{\varepsilon} = \tfrac{1}{2}(\mathbf{F} + \mathbf{F}^T) - \mathbf{1} \tag{1.16}$$

after verifying that $\partial x_Z / \partial \Theta \cong 0$ holds true for all measured deformation fields. In an attempt to compensate for fluctuations in the strain field due to the polycrystalline nature of the microstructure (and the noise in the DIC measurements), we report the spatial average of the surface strain fields over a square area of $A = 200 \times 200 \mu m$,

$$< \boldsymbol{\varepsilon} > = \frac{1}{A}\int_A \boldsymbol{\varepsilon} dZ = \begin{bmatrix} \varepsilon_\theta & \gamma/2 \\ \gamma/2 & \varepsilon_z \end{bmatrix}. \tag{1.17}$$

In the sequel, the components ε_θ, ε_z and γ of this average nominal strain tensor are referred to as circumferential, axial and shear strain, respectively.

In addition to the nominal strains, we also evaluate the average logarithmic surface strain tensor $< \boldsymbol{\varepsilon}_{\ln} >$. For this, $\mathbf{F}$ is decomposed into a rotation $\mathbf{R}$ and the right stretch tensor,

$$\mathbf{U} = \mathbf{R}^T \mathbf{F} = \sum_{i=1}^{2} \lambda_i \mathbf{u}_i \otimes \mathbf{u}_i \tag{1.18}$$

which yields

$$\boldsymbol{\varepsilon}_{\ln} = \sum_{i=1}^{2} \ln(\lambda_i) \mathbf{u}_i \otimes \mathbf{u}_i \,. \tag{1.19}$$

2.4. Average Cauchy stress estimates

Throughout the experiments, the axial force F and the torque M are measured. Neglecting the radial gradient in the mechanical fields within a cross-section, the average true axial stress σ and the average true shear stress τ can be estimated,

$$\sigma = \frac{F}{\pi(D+t)t}(1+\varepsilon_z) \quad (1.20)$$

and (using Bredt's approximation)

$$\tau = \frac{2M}{\pi(D+t)^2 t}\frac{1+\varepsilon_z}{1+\varepsilon_\theta} \quad (1.21)$$

with D and t denoting the initial inner diameter and initial thickness, respectively.

2.5. Experimental results

2.5.1. Overview

Experiments are performed for five distinct biaxial loading angles: $\beta = 0°$, $\beta = 34.1°$, $\beta = 55°$, $\beta = 69.5°$ and $\beta = 90°$. As illustrated in Fig. I-3, $\beta = 0°$ corresponds approximately to pure shear, $\beta = 55°$ to uniaxial tension, and $\beta = 90°$ to transverse plane strain tension. The experiments for the intermediate loading angles $\beta = 34.1°$ and $\beta = 69.5°$ feature approximately the same Lode angle parameter ($\bar{\theta} = 0.54$), but two distinct stress triaxialities ($\eta = 0.18$ and $\eta = 0.49$).

The measured force-displacement curves ($F - \Delta u$) and moment-rotation curves ($M - \Delta\theta$) are shown as dashed lines in Fig. I-5. Relative displacements are measured between two points A and B, located on the shoulder section of the specimen, at a distance of 8mm from the symmetry plane (Fig. I-4d). The end of each dashed curve corresponds to the point where a sudden drop in force/torque occurs. At this instant, a macroscopic crack becomes visible on the specimen surface (specimen fracture). A monotonically increasing moment-rotation curve is measured for pure torsion ($\beta = 0°$). In all experiments with tension applied, we observe a modest decrease in the axial force-displacement curve prior to specimen fracture. At the macroscopic level, it is interesting to observe that a higher axial displacement can be achieved when applying torsion in addition to tension (compare $F - \Delta u$ curve for $\beta = 69.5°$ with that for $\beta = 90°$).

The loading paths in terms of the measured nominal surface strains are shown in Fig. I-6a and b. The maximum shear strain under pure torsion is $\gamma = 1.55$, while a maximum axial strain of $\varepsilon_z = 0.45$ is observed for $\beta = 69°$. The plot of the evolution of the circumferential strain (Fig. I-6b) reveals that the assumption of plane strain conditions along the circumference is

not full-filled in reality. According to the stereo DIC measurement, the magnitude of the circumferential strain (contraction) is about 10% of the axial strain. The loading paths in terms of the average true shear and axial stresses (Fig. I-6c) are approximately linear which is an immediate consequence of keeping the loading angle β constant throughout loading. From a theoretical point of view, the non-linearity in the average true stress loading paths is only due to the non-zero circumferential strain (see Eqs. (1.22) and (1.23)).

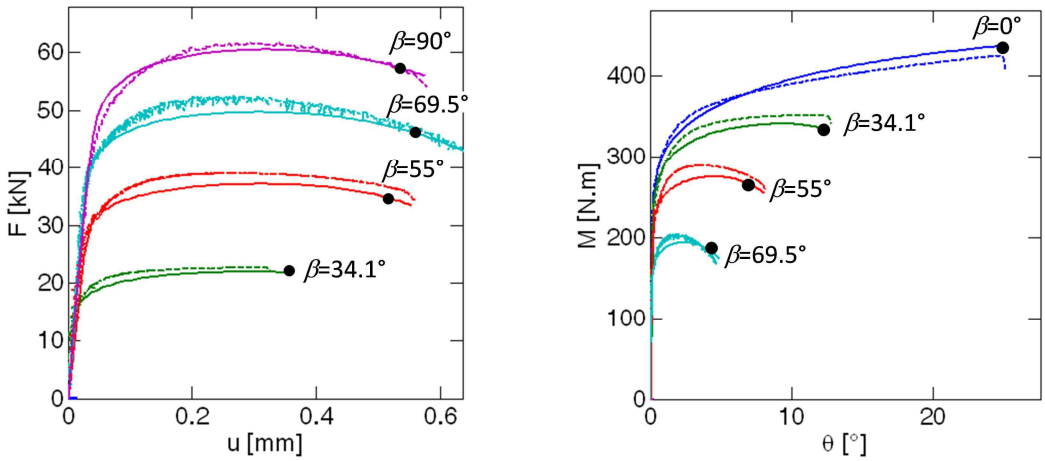

(a) (b)

Fig. I-5 (a) Axial force-displacement and (b) torque-rotation curves for different biaxial loading angles. Dashed lines stand for experiments, while solid lines stand for simulations. The solid black dots on the simulation curves indicate the instant of onset of fracture as predicted by the HC model.

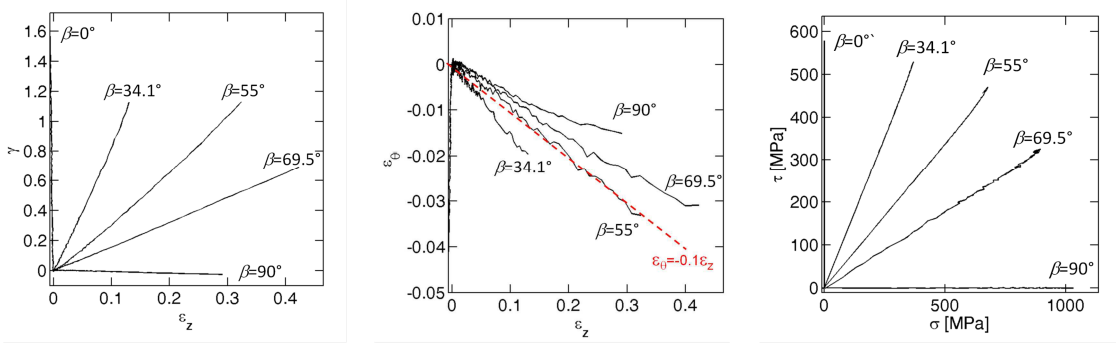

(a) (b)

Fig. I-6 Loading paths: (a) nominal shear versus axial strain, (b) nominal circumferential versus axial strain, (c) average true shear versus true normal stress.

2.5.2. Surface strain fields and localization

Selected strain fields just prior to the onset of fracture are shown in Fig. I-7 next to the photographs of the fractured specimens. The contour maps demonstrate the uniformity of the strain field along the circumference up to fracture initiation. For $\beta = 90°$ the final crack is

located near the plane $Z = 0$ which is attributed to the localization of plastic deformation at the specimen center. The same observation and argument hold also true for $\beta = 55°$ (Fig. I-7c and d). However, the final crack meanders along the circumference for $\beta = 0°$ (Fig. I-7e), where the strain field remains more or less uniform up to the onset of fracture (Fig. I-7f).

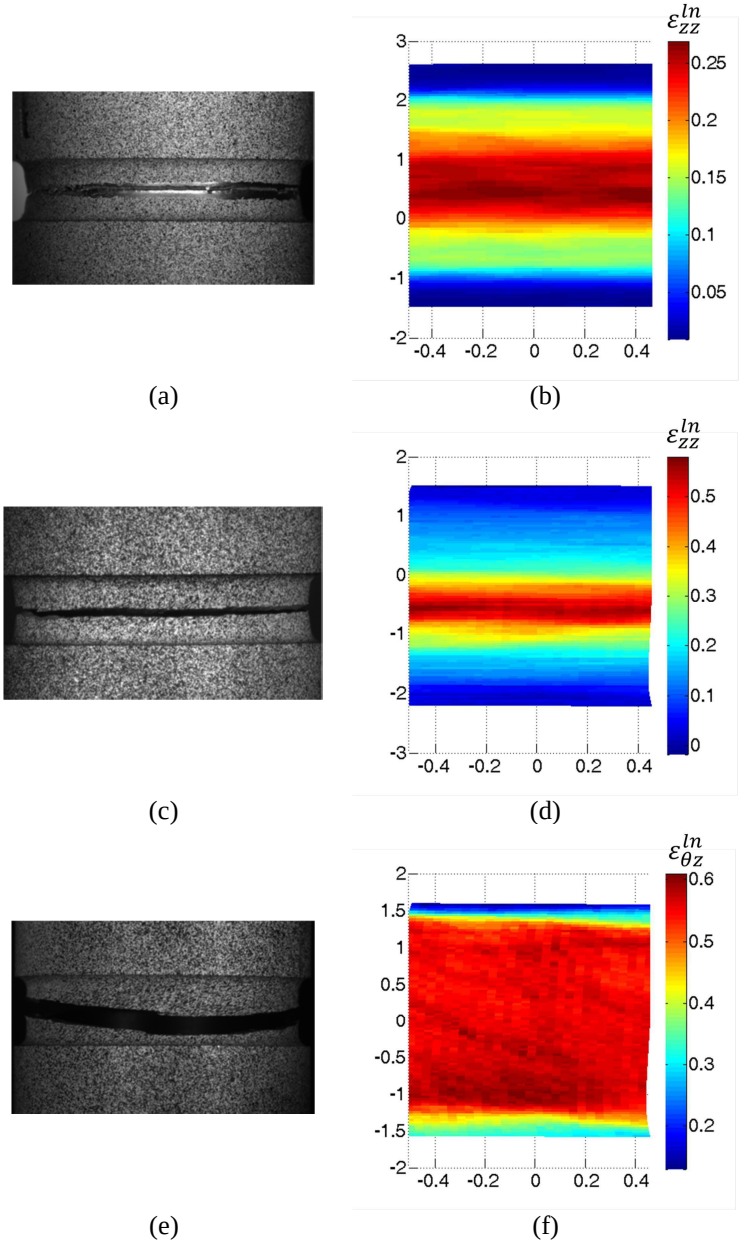

Fig. I-7 Photographs of the fractured specimens and measured surface strain fields at the onset of fracture. (a)-(b) $\beta = 90°$, (c)-(d) $\beta = 55°$, (e)-(f) $\beta = 0°$.

To shed some light on the localization of deformation prior to specimen fracture, we extracted the distribution of selected components of the logarithmic surface strain tensor along the z-axis from the digital image correlation results (Fig. I-8):

- Fig. I-8a to c summarize the results for $\beta = 90°$. At force maximum (point ① in Fig. I-8a) and slightly beyond (point ②), the distribution of $\varepsilon_{zz}^{\ln}$ along the z-axis is approximately uniform. Note that we plotted the unfiltered strain distribution (dashed lines) along with that obtained after applying a moving spatial average filter on a 200μm kernel (solid line). When the strain exceeds about 0.15, the strains tend to localize within an about $1\,mm$ long region of the gage section (necking). This observation is consistent with the cross- sectional view of the fractured specimen (Fig. I-8c) which shows a pronounced through-thickness neck.
- For tension-torsion loading at $\beta = 55°$ (Fig. I-8d to f), the localization of plastic deformation occurs at a surface strain of about $\varepsilon_{zz}^{\ln} \cong 0.2$. The zone of plastic localization is only about $0.5\,mm$ wide and therefore more narrow than for $\beta = 90°$. A maximum surface strain of about $\varepsilon_{zz}^{\ln} \cong 0.5$ is reached prior to specimen fracture, which is twice as high as that for $\beta = 90°$.
- For $\beta = 0°$ (pure shear), the variation of the shear component $\varepsilon_{\theta z}^{\ln}$ of the logarithmic strain tensor is plotted as a function of Z (Fig. I-8g to j). The plots at different stages of loading show a more or less uniform distribution at all stages of loading. Specimen fracture occurs at a surface strain of about $\varepsilon_{\theta z}^{\ln} = 0.58$. Unlike for $\beta = 55°$ and 90°.The corresponding fracture surface is not inclined, but perpendicular to the $\mathbf{e}_Z$ -axis.

3. Finite element analysis

Necking prior to the onset of fracture appears to be unavoidable for biaxial loading angles greater than $55°$ (except for low ductility, high strain hardening materials). As a result, the mechanical fields exhibit significant variations along the radial directions. In order to obtain accurate estimates of the stress and strain fields inside the specimen, a finite element analysis of each experiment is performed.

3.1. Finite element model

The specimen geometry is discretized with four-node axisymmetric elements with a twist degree of freedom (type CGAX4R of the Abaqus/standard element library, Abaqus, 2011).

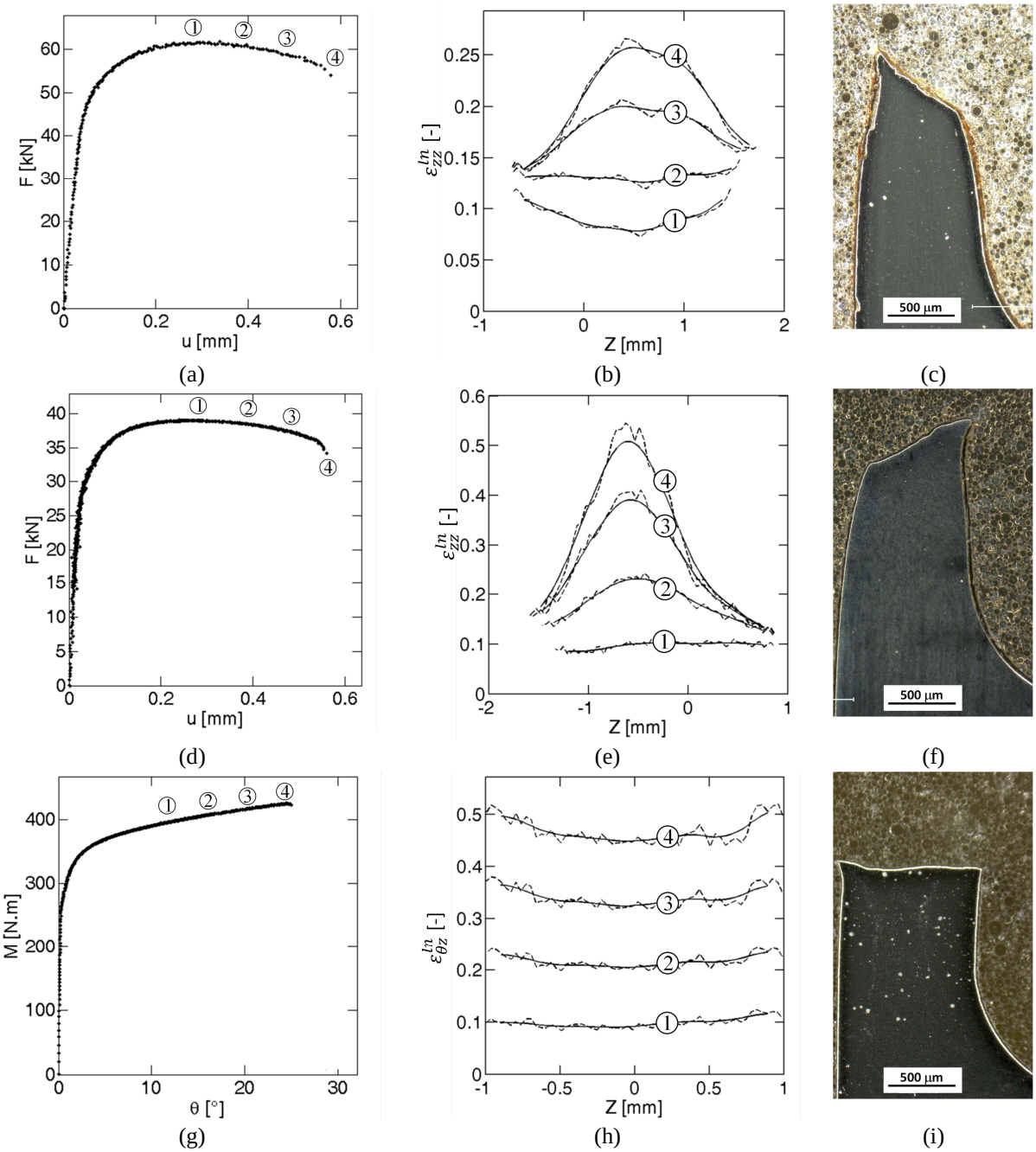

Fig. I-8 Evolution of the surface strains throughout loading: (a)-(c) $\beta = 90°$, (d)-(f) $\beta = 55°$, and (g)-(i) $\beta = 0°$. The solid (dashed) lines in the central plots correspond to the strains obtained from the displacement measurements with (without) averaging over a $200\ \mu m$ period. The rightmost column shows longitudinal cuts through the fractured specimens.

Based on a mesh size convergence study with respect to the evolution of the equivalent plastic strain in the specimen center, the specimen gage section is discretized with 40 first-order elements along the radial direction (Fig. I-1b). The degrees of freedom of the nodes on the top surface are all coupled in a virtual rigid body via one reference node on the axis of rotation (node N1 in Fig. I-1 b). Similarly, the degrees of freedom of the nodes on the bottom surface are coupled to those of the reference node N2. All displacements and rotations are set to zero for the latter. A tension (respectively torsion) test is simulated by applying an axial displacement (respectively rotation) on the reference node N1, as measured by DIC. For combined loading, a user subroutine (UAMP) is employed to mimic the experimental procedure: for $\beta \geq 55°$, the axial displacement is prescribed and the rotation history is incrementally adjusted such that β remained constant. Analogously, for $\beta < 55°$, the rotation is prescribed while the axial displacement is adjusted incrementally. At least 100 implicit time steps are performed to complete a simulation.

3.2.Constitutive equations

A basic J_2-plasticity model is used to describe the elasto-plastic response of the material in an approximate manner. The isotropic yield function is expressed in terms of the equivalent von Mises stress $\bar{\sigma} = \bar{\sigma}[\boldsymbol{\sigma}]$ and a deformation resistance $k = k[\bar{\varepsilon}_p]$,

$$f[\boldsymbol{\sigma}, \bar{\varepsilon}_p] = \bar{\sigma}[\boldsymbol{\sigma}] - k[\bar{\varepsilon}_p] = 0 \,. \tag{1.22}$$

Furthermore, an associated flow rule is assumed,

$$d\boldsymbol{\varepsilon}^p = (d\bar{\varepsilon}_p)\frac{\partial \bar{\sigma}}{\partial \boldsymbol{\sigma}} \,. \tag{1.23}$$

with $d\bar{\varepsilon}_p$ defining the increment in the equivalent plastic strain. Only monotonic loading paths are considered and we thus limit our attention to a simple isotropic hardening model. Following the work of Sung et al. [73] and Mohr and Marcadet [53], a combined Voce-Swift model is used,

$$k = k[\bar{\varepsilon}_p] = k_0 + Q\left(1 - e^{-b\bar{\varepsilon}_p}\right) + A(\bar{\varepsilon}_p + \varepsilon_0)^n \tag{1.24}$$

with the Swift parameters $\{A, \varepsilon_0, n\}$ and the Voce parameters $\{k_0, Q, b\}$.

3.3. Identification of the plasticity model parameters

The isotropic hardening parameters $\chi = \{A, n, \varepsilon_0, k_0, Q, b\}$ are determined through inverse analysis. For this, a virtual extensometer is defined between two nodes of the finite element mesh which measures the same relative displacement as the optical extensometer between the points A and B specimen shoulders in the experiments (Fig. I-4d). The residual identification error is defined as the sum of the relative difference between the predicted and measured forces and moments,

$$\psi[\chi] = \sum_{\beta_i} \sum_{k} \left(\frac{F_{\exp}^{\beta_i,k} - F_{sim}^{\beta_i,k}[\chi]}{F_{\exp}^{\beta_i,k}} \right)^2 + \left(\frac{M_{\exp}^{\beta_i,k} - M_{sim}^{\beta_i,k}[\chi]}{M_{\exp}^{\beta_i,k}} \right)^2 . \tag{1.25}$$

The residual is minimized using a derivative-free Nelder-Mead algorithm (Matlab Optimization Toolbox). Tests corresponding to $\beta = \{0°, 55°, 90°\}$ are used for the identification. An initial guess of the hardening parameters is obtained from a separate fit of the Voce and Swift models to the approximate stress-strain curve obtained from the torsion experiment (assuming $\bar{\sigma} \cong \sqrt{3}\tau$, $\bar{\varepsilon}_p \cong \gamma/\sqrt{3}$) as shown in Fig. I-9. The same figure also shows the combined Swift-Voce hardening curve that is obtained after optimization (red solid curve). A comparison of the seed and final hardening parameters is shown in Tab. I-2. A plot of the simulations results for the final set of parameters (solid lines in Fig. I-5) shows reasonable agreement with the experimental results, although there could be room for improvement on the yield surface front, as the simulation tends to underestimate the values of the force and the torque for multiaxial tests.

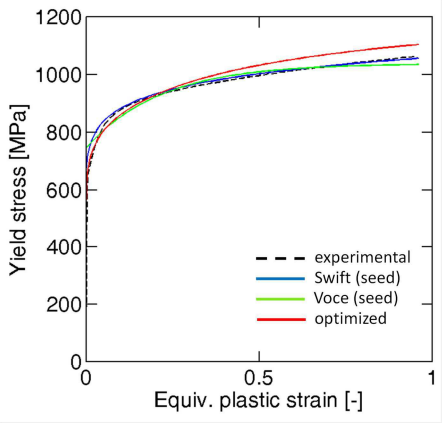

Fig. I-9 Identification of the isotropic hardening law.

E (GPa)	ν	A (MPa)	ε_o	n	k_o (MPa)	Q (MPa)	b
200	0.3	529.4	3.10^{-3}	0.08	372.3	146.4	4.64
200	0.3	712	7.10^{-5}	0.13	307	92	3.24

Tab. I-2 Hardening parameters before (first line) and after optimization (second line)

4. Determination of the loading paths to fracture

The term *loading path to fracture* is used to make reference to the evolution of the stresses and strains at the point(s) within the specimen where fracture initiates. At the macroscopic level the polycrystalline material is considered as homogeneous solid. The macroscopic material description becomes invalid after the eventual formation of shear bands. However, at the macroscopic level, the onset of fracture is expected to be imminent with the onset of shear localization. It is emphasized that all fracture strains reported in this work correspond to macroscopic strains which are expected to be significantly lower than the strains to fracture at the microscale (see Haltom et al. [72] for a comparison of measured macroscopic and grain strains). In the sequel, two different methods are considered to determine the loading paths to fracture.

4.1. Method I: Surface-strain based estimates

Several simplifying assumptions are made to obtain a first estimate of the loading path to fracture:

(A1) Small elastic strains;

(A2) the Levy-von Mises flow rule applies;

(A3) the circumferential strain is zero;

(A4) the mechanical fields do not vary along the radial direction and plane stress conditions prevail within the gage section;

(A5) the stress-state remains constant throughout loading;

With the above assumptions in place, Eqs. (1.6) and (1.7) are applied to calculate the stress triaxiality and the Lode angle parameter. Furthermore, the equivalent plastic strain at the onset of specimen fracture may be calculated as

$$\bar{\varepsilon}_f = \sqrt{\frac{2}{3}}\sqrt{\boldsymbol{\varepsilon}_{\ln} : \boldsymbol{\varepsilon}_{\ln} + (tr\boldsymbol{\varepsilon}_{\ln})^2} \tag{1.26}$$

after evaluating the logarithmic surface strain tensor based on the surface deformation gradient

$$\mathbf{F}_f \cong \begin{bmatrix} 1 & \gamma_f \\ 0 & 1+\varepsilon_{zf} \end{bmatrix}. \tag{1.27}$$

In (1.29), γ_f and ε_{zf} denote the measured shear and axial surface strains at the specimen center at the instant of specimen fracture. According to (A5) the loading path corresponds to a vertical line in the plot of the equivalent plastic strain as a function of the stress triaxiality (red dashed lines in Fig. I-10a).

Fig. I-10a also includes error bars for the estimated equivalent plastic strains to fracture. As an alternative to Method I, the strains to fracture have been computed using the complete measured loading history which accounts for the non-zero circumferential strain and the small non-linearity of the loading path in true strain space (integration of equivalent strain increments instead of using (1.26)). The comparison shows that Method I systematically underestimates the surface strains to fracture. The uncertainty in the stress triaxiality (not shown) is associated with assumption (A3). Evaluation of the stress triaxiality for $d\varepsilon_\theta / d\varepsilon_Z \neq 0$ yields

$$\eta = \frac{1}{3}\frac{(1+\kappa)\tan\beta}{\sqrt{(1+\kappa^2-\kappa)\tan^2\beta+3}} \tag{1.28}$$

with

$$\kappa = \frac{2\left(\dfrac{d\varepsilon_\theta}{d\varepsilon_Z}\right)+1}{2+\left(\dfrac{d\varepsilon_\theta}{d\varepsilon_Z}\right)} \tag{1.29}$$

Assuming $d\varepsilon_\theta / d\varepsilon_Z = -0.1$ corresponds to an uncertainty of about 5% in the stress triaxiality, irrespective of the biaxial loading angle. For example, for $\beta = 90°$ the stress triaxiality estimated by Eq. (1.28) is 0.54 as compared to 0.58 according to Eq. (1.4).

4.2.Method II: full FEA analysis

Assumptions (A1) through (A5) can be omitted with the availability of finite element simulations. However, it is necessary to speculate on the exact location of the onset of fracture. Formally, we note the two key assumptions of Method II as

(A6) the finite element simulations provide an accurate description of the experiments (even for very large strains)

(A7) fracture initiates at the point of maximum equivalent strain within the central specimen section

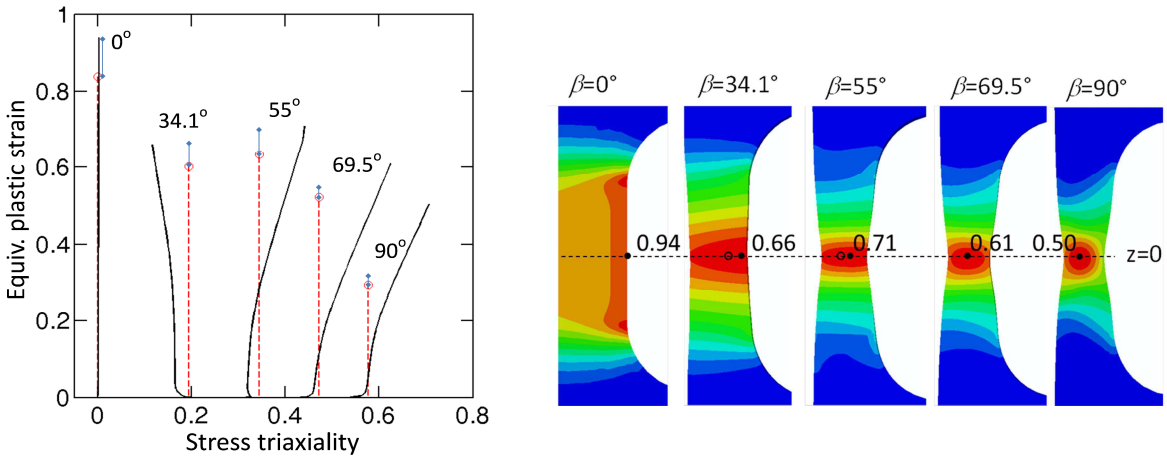

(a) (b)

Fig. I-10 (a) Loading paths to fracture as determined using the (i) Surface-strain based method (dashed red lines), and (ii) full FEA method; (b) distribution of the equivalent plastic strain within the specimen cross-section at the onset of fracture as obtained from FEA. The solid dots indicate the locations of loading path extraction. For $\beta = 34.1°$ and $55°$, an open dot highlights the location of onset of fracture as predicted by the HC model.

Assumption (A6) is partially validated by the agreement of the measured and simulated force-displacement and torque-rotation curves. This agreement is rather difficult to achieve as the results from multi-axial experiments are sensitive to small changes in the yield surface/flow potential assumptions. It appears to be very difficult to confirm assumption (A7) with state-of-the-art experimental techniques. The fact that the observed fracture plane of each specimen intersects the plane Z=0 is one minor partial validation. The analysis of marks and features on the fracture surface did not yield any valuable information. Thus, unless the experiment can be stopped right at the onset of fracture or high speed tomography becomes available, assumption (A7) will be one of the key sources of uncertainty in the reported loading paths to

fracture.[1] When using the experimental data to calibrate a fracture model, it is recommended to repeat all finite element simulations with the calibrated fracture initiation model active to make sure that the onset of fracture indeed occurs at the location assumed during calibration.

Fig. I-10b shows the specimen cross-sections at the instant where the equivalent plastic strain on the specimen surface equals that measured experimentally. The contour plots clearly illustrate the gradient in equivalent plastic strain along the axial as well as the radial direction. Black solid dots in Fig. I-10b highlight the locations where fracture initiates according to assumption (A7). The corresponding loading paths obtained from Method II are shown as black solid lines in Fig. I-10a. The comparison with the loading paths obtained by Method I shows a significant difference between the loading path to fracture on the specimen surface and that at the point of the highest equivalent plastic strain inside the specimen. The only exception is the pure torsion experiment where the highest equivalent plastic strain is reached on the specimen surface. For β=34.1°, 55° and 69°, a triaxiality-offset can be noticed between methods I and II, even for small strains. This offset is due to a gradient of axial stress in the radial direction, which is about 10% of the maximal axial stress. For $\beta \geq 55°$, the triaxiality increases throughout loading due to necking. For β=34.1°, the stress triaxiality decreases as the equivalent plastic strain exceeds 0.2. This decrease is due to an increasing radial gradient of axial stress field which decreases the axial stress near the external gage section surface.

5. Fracture modeling

The Hosford-Coulomb fracture initiation model (HC) was introduced by Mohr and Marcadet [53] to predict the onset of fracture in advanced high strength steel sheets (DP590, DP780, TRIP780) under monotonic loading. It is based on the assumption that ductile fracture is imminent with the shear/normal localization of deformation within a narrow band (Barsoum and Faleskog [34], Dunand and Mohr [55]).

The recently proposed Hosford-Coulomb (HC) fracture initiation model is used to describe the reported experimental data. We briefly recall the model formulation before identifying the three model parameters. Readers are referred to Mohr and Marcadet [53] for details on the HC model.

[1] It is worth noting that Mohr and Henn [56] addressed this issue by reporting the loading paths for all elements within the specimen gage section, knowing that at least one of the reported paths must have led to the onset of fracture.

5.1. Hosford-Coulomb (HC) fracture initiation model

According to the HC model, fracture is said to initiate for proportional loading when the linear combination of the Hosford equivalent stress and the normal stress acting on the plane of maximum shear reaches a critical value,

$$\bar{\sigma}_{HF} + c(\sigma_1 + \sigma_3) = \sigma_c \tag{1.30}$$

where

$$\bar{\sigma}_{HF} = \left\{ \frac{1}{2} \left((\sigma_1 - \sigma_2)^a + (\sigma_1 - \sigma_3)^a + (\sigma_2 - \sigma_3)^a \right) \right\}^{\frac{1}{a}} \tag{1.31}$$

with $a > 0$ denoting the Hosford exponent of the fracture initiation model, the friction coefficient $c \geq 0$, and the cohesion $\sigma_c > 0$. Mohr and Marcadet [53] transformed the above criterion from the ordered principal stress space $\{\sigma_1, \sigma_2, \sigma_3\}$ to the mixed stress-strain space $\{\eta, \bar{\theta}, \bar{\varepsilon}_p\}$ for a von Mises plasticity material with isotropic hardening. The transformation is performed below.

Eq. (1.31) is subsequently rewritten in terms of the modified Haigh-Westergaard coordinates $\{\bar{\sigma}, \eta, \bar{\theta}\}$,

$$\bar{\sigma} = \bar{\sigma}_f[\eta, \bar{\theta}] = \frac{\sigma_c}{\left\{ \frac{1}{2} \left((f_1 - f_2)^a + (f_1 - f_3)^a + (f_2 - f_3)^a \right) \right\}^{\frac{1}{a}} + c(2\eta + f_1 + f_3)} \tag{1.32}$$

using the Lode angle parameter dependent functions

$$f_1(\bar{\theta}) = \tfrac{2}{3} \cos\left[\tfrac{\pi}{6}(1 - \bar{\theta})\right], \quad f_2(\bar{\theta}) = \tfrac{2}{3} \cos\left[\tfrac{\pi}{6}(3 + \bar{\theta})\right] \text{ and } \quad f_3(\bar{\theta}) = -\tfrac{2}{3} \cos\left[\tfrac{\pi}{6}(1 + \bar{\theta})\right] \tag{1.33}$$

Using the inverse of the isotropic hardening law (1.24), the fracture criterion (1.32) is transformed from the stress space $\{\eta, \bar{\theta}, \bar{\sigma}\}$ to the mixed strain/stress space $\{\eta, \bar{\theta}, \bar{\varepsilon}_f\}$,

$$\bar{\varepsilon}_f^{\,pr} = k^{-1}\left[\bar{\sigma}_f[\bar{\theta}, \eta]\right]. \tag{1.34}$$

which defines the macroscopic strain at the onset of fracture for proportional loading. Note that (1.32) and (1.34) are fully equivalent for proportional loading. For non-proportional loading, the strain to fracture $\bar{\varepsilon}_f$ is defined through the integral extension (Fischer et al., [74])

$$\int_0^{\bar{\varepsilon}_f} \frac{d\bar{\varepsilon}_p}{\bar{\varepsilon}_f^{\,pr}[\bar{\theta}, \eta]} = 1. \tag{1.35}$$

5.2. Fracture model parameter identification

The HC fracture initiation model features three material parameters: the Hosford exponent a, the cohesion σ_c, and the friction coefficient c. These parameters are determined based on the loading paths to fracture for $\beta = 0°$ (pure shear), $\beta = 55°$ (uniaxial tension) and $\beta = 90°$ (plane strain tension). The parameters $a = 1.6$, $\sigma_c = 1132.7\,\text{MPa}$ and $c = 0.053$ are identified by minimizing the following residual:

$$R = \sum_{\beta \in \{0°,55°,90°\}} \left(\int_0^{\bar{\varepsilon}_{f,II}} \frac{d\bar{\varepsilon}_p}{\bar{\varepsilon}_f^{pr}[\bar{\theta},\eta]} - 1 \right) \quad \text{for} \quad \beta_i = \{0°,55°,90°\} \tag{1.36}$$

with $\bar{\varepsilon}_{f,II}$ denoting the strain at the onset of fracture determined using Method II (section 4.2). The instants at which the calibrated HC model predicts the onset of fracture are highlighted by blue solid dots in Fig. I-11a. These instants coincide with the ends of the loading paths to fracture for the three calibration experiments ($\beta = 0°, 55°$ and $90°$) whereas the HC model overestimates the strain to fracture for $\beta = 34°$, and underestimates that for $\beta = 69°$. The underlying fracture criterion for proportional loading (Eq. (1.34)) is depicted in Fig. I-11b, showing the monotonic dependence of the strain to fracture on the stress triaxiality and the characteristic asymmetric dependence on the Lode angle parameter with a minimum at $\bar{\theta} = 0$.

We also implemented the HC model into a user material subroutine and repeated the simulations of all experiments with the fracture initiation criterion being active (Eq. (1.35)). The solid black dots on the curves in Fig. I-5 show the instant of fracture as predicted by the HC model. The reasonable agreement with the respective displacements and rotations to fracture partially confirms the applicability of the HC fracture initiation model and the validity of the underlying identification procedure. For each loading case, we also compared the location of the critical element at which fracture initiates according to the model with that assumed throughout calibration. These locations coincide for $\beta = 0°, 69.5°$ and $90°$. However, for $\beta = 34°$ and $\beta = 55°$, the HC model predicts fracture at slightly different locations as shown by the comparison of the open and solid dots in Fig. I-10b. It is thus expected that the model accuracy could be improved further by repeating the model parameter identification based on the loading paths to fracture extracted from the predicted locations of onset of fracture.

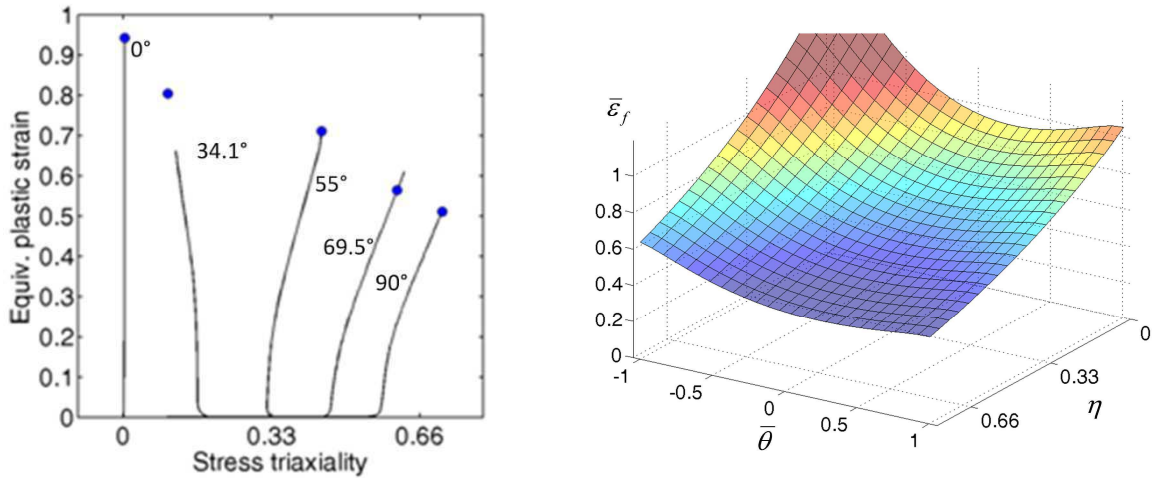

(a) (b)

Fig. I-11 (a) Predictions of the onset of fracture according to the calibrated HC model (blue dots), (b) 3D plot of the fracture initiation model for proportional loading.

6. Conclusions

A tubular specimen with a stocky gage section of uniform thickness is proposed to characterize the effect of stress state on the onset of ductile fracture under tension-torsion loading. Prior to the onset of necking, the radial gradient in the mechanical fields is small and plane stress conditions prevail throughout the gage section. At the same time, the circumferential strain is approximately zero. The theoretical range of achievable stress triaxialities is -0.58 to 0.58 for a Levy-von Mises material.

Static experiments are performed on specimens extracted from an annealed high strength steel bar (36NiCrMo16) for positive stress triaxialities. The relative motion of the specimen shoulders as well as the surface strain fields are determined through stereo digital image correlation. Finite element simulations are performed of all experiments to estimate the stresses and strains away from the specimen surface. From each experiment, a loading path to fracture is determined in terms of equivalent plastic strain, stress triaxiality and Lode angle parameter. It is found that the loading paths obtained from finite element analysis are substantially different from those determined directly from surface strain measurements. Except for pure torsion, the equivalent plastic strain reaches its maximum away from the specimen surface. Furthermore, the stress triaxiality is significantly higher near the specimen

center when fracture initiates after necking. A hybrid experimental-numerical procedure is outlined and applied to determine the parameters of the Hosford-Coulomb fracture initiation model.

II. Bao-Wierzbicki revisited: Ductile Fracture of Al2024-T351 under Proportional and Non-proportional Loading

---

The present chapter is devoted to an investigation of the effect of the stress state on the strain to fracture of the aerospace aluminum alloy 2024-T351 at low stress triaxialities using the hybrid experimental-numerical technique developed in Chapter I. The ductility of this material has been studied by Bao and Wierzbicki [5] *in a wide range of stress states. The outcome of this extensive experimental campaign was a fracture locus which has been cited in many papers ever since, as it is a very good illustration of the complexity of the relationship between the stress state and the ductility. In this chapter, proportional and non-proportional loading cases are applied to the stocky tubular specimen, and a fracture locus is determined, and compared with the fracture locus obtained by Bao and Wierzbicki* [5]. *In particular, higher strain to fracture is found for pure shear than for uniaxial tension, which is consistent with the results for many other alloys, but contradicts the important results reported by Bao and Wierzbicki* [5]. *The data from the stocky tubular specimen is then used to calibrate the Hosford-Coulomb criterion, introduced in Chapter I. The necessity to extend the Hosford-Coulomb model with a non-linear damage accumulation rule to predict failure for complex stress states history is outlined.*

The work of Bao and Wierzbicki [5] has contributed significantly to the development of ductile fracture initiation models that depend on the Lode angle in addition to the stress triaxiality. Bao and Wierzbicki [5] performed experiments on a variety of specimens of different geometry to quantify the effect of stress triaxiality on the equivalent strain at the onset of fracture. Their results suggested that the stress triaxiality is a non-monotonic, non-smooth function of the stress triaxiality with a local maximum in ductility at a stress triaxiality of about 0.4 and local minimum in ductility at a stress triaxiality of zero (pure shear).

The apparent decrease in ductility for shear-dominant loading has been particularly intriguing since conventional Gurson-type of models predict a monotonically decreasing strain to fracture as a function of the stress triaxiality. In the shear-modified Gurson model proposed by Nahshon and Hutchinson [35], the evolution of the void volume fraction is not only a function of the equivalent plastic strain, but also sensitive to the Lode number. Unlike conventional Gurson models, the Nahshon-Hutchinson model can predict fracture through shear and normal localization at very low stress triaxialities. Danas and Ponte Castaneda [45] made use of a homogenization model that accounts for the Lode angle dependent evolution of the pore shape in porous metals. Their approximate analysis suggests a reduction in ductility as the stress triaxiality decreases to zero due to collapsing voids. Both models can explain the trends observed in the experimental data of Bao and Wierzbicki [5] for aluminum 2024-T351 and that of Barsoum and Faleskog [6] for Weldox steel. Benzerga et al. [75] investigated theoretically the effect of the loading paths on the fracture locus by means of unit cell calculations for proportional and non-proportional loading, for axisymmetric stress states. Their investigation suggests that the utilization of averaged values of stress triaxiality to construct the fracture locus using tests in which deviations from proportionality is likely to occur could have a role in the non-monotonic relationship between the ductility and the stress triaxiality for low values of the stress triaxiality.

Ductile damage indicator models have also been modified to describe the apparent non-monotonic relationship between the strain to fracture and the stress triaxiality. Bao and Wierzbicki [5] proposed a multi-branch model to explain this relationship. However, as shown by Xue [76], a smooth relationship among the equivalent plastic strain, the stress triaxiality and the Lode angle parameter can explain an apparent non-monotonic fracture strain versus stress triaxiality relationship. For example, assuming a monotonic decrease of the strain to fracture in stress triaxiality and a monotonic increase as function of absolute

value of the Lode number can explain the local minimum in ductility for pure shear and a maximum (kink point) for uniaxial tension.

The experimental data of Bao and Wierzbicki [5] has also been explored to develop stress-based fracture initiation models. Stoughton and Yoon [77] made use of their data to show that a Mohr-Coulomb criterion can describe the onset of fracture in stress space. Another criterion in stress space has been proposed by Khan and Liu [78] after supplementing Bao and Wierzbicki's [5] data with additional experimental data points. Bai and Wierzbicki [49] also explored the idea of a Mohr-Coulomb fracture model in stress space to come up with the corresponding damage indicator model in the combined strain-stress space of equivalent plastic strain, stress triaxiality and Lode angle parameter. A micro-mechanism inspired ductile fracture model was proposed by Lou et al. [79,80]. Their model had also been validated using the data reported for aluminum 2024-T351 by Bao and Wierzbicki [5].

The non-uniformity of the stress and strain fields in ductile fracture experiments typically requires a hybrid experimental-numerical analysis of the measurements (e.g. Mohr and Henn [56], Barsoum and Faleskog [6,81], Dunand and Mohr [59]). The data of Bao and Wierzbicki [5] for aluminum 2024-T351 was obtained using a J2-plasticity model with power-law hardening. As demonstrated for a variety of aluminum alloys (e.g. Barlat et al. [82], Karafillis and Boyce [83], Bai and Wierzbicki [84], Bron and Besson [85], Giagmouris et al. [86]), non-quadratic yield functions and their anisotropic counter parts appear to be more suitable for describing the plastic response of polycrystalline FCC materials. However, a possibly more important source of uncertainty in the hybrid experimental-numerical analysis of fracture initiation experiments is the speculation on the location of onset of fracture. For instance, in case significant barreling occurs in an upsetting test, fracture may not start under uniaxial compression at the specimen center, but under biaxial loading at the specimen surface.

In the present work, tension-torsion experiments are performed on stocky tubular aluminum 2024-T351 specimens. It is found that an isotropic Hosford plasticity model with combined Swift-Voce hardening provides a satisfactory approximation of the multi-axial material response of the onset of fracture. Using the hybrid experimental-numerical procedure presented in Chapter I, the loading paths to fracture are determined in terms of the equivalent plastic strain, the stress triaxiality and the Lode angle parameter. The calibration of the Hosford-Coulomb fracture initiation model suggests that the ductility of aluminum 2024-T351 decreases monotonically as a function of the stress triaxiality, whereas it is a non-symmetric convex function of the Lode angle parameter.

1. Experiments

We closely follow the experimental procedure for tension-torsion fracture testing described in Chapter I. Using a dual actuator system, selected combinations of tension and torsion loading are applied to a stocky tubular specimen.

1.1. Material and specimen

All specimens are extracted from the same square bar of aluminum 2024-T351 supplied by the distributor McMaster Carr. A 900mm long bar with a 100mm x 100mm square cross-section is chosen instead of a plate or tube product in an attempt to minimize the effects of initial anisotropy. The chemical composition according to the provider is given in Tab. II-1. More details on the material microstructure will be considered in Chapter III.

The exact geometry of the stocky tubular specimen is shown in Fig. I-1. It features a constant inner initial diameter of 20mm. The wall thickness is 2mm in the shoulder area, while it is only $e_{ini} = 1mm$ within the 4mm high gage section. The transition from the 22mm to the 24mm outer diameter is achieved through a toroidal surface of 1mm radius. The specimen axis is always parallel to the longitudinal bar direction. Except for the area that is inserted into the machine clamps, a thin layer of white paint is applied on the specimen surface along with a fine black speckle paint pattern.

-	Si	Fe	Cu	Mn	Mg	Cr	Zn	Ti	Other	Al
Min	/	/	3.8	0.3	1.2	/	/	/	/	remain
Max	0.5	0.05	4.9	0.9	1.8	0.1	0.25	0.15	0.15	remain

Tab. II-1 Chemical composition of aluminum 2024-T351 from the square bar, according to McMaster-Carr, in weight %

1.2.Experimental procedure

Readers are referred to Chapter I for details about the experimental procedure.

1.3.Measured force-displacement curves

Two different series of experiments are performed: proportional loading experiments (monotonic loading with $\beta = const.$) and non-proportional loading experiments (non-monotonic loading with $\beta = \beta(t)$). The testing program for the first series of experiments covered seven distinct biaxial loading angles: $\beta = 0°$, $\beta = 21.9°$, $\beta = 34.1°$, $\beta = 45°$, $\beta = 55°$, $\beta = 69.5°$ and $\beta = 90°$. The specific actuator control settings were:

- for $\beta = 0°$, (pure shear) the rate of rotation is (0.019°/s) while a zero axial force is imposed.
- for $21.9° \leq \beta \leq 55°$ (shear-dominated), the rate of rotation is prescribed (0.019°/s) while the axial position is incrementally adjusted so as to keep β constant.
- for $\beta = 69.5°$, (tension-dominated), the rate of axial displacement is prescribed (0.002mm/s) while the rotational position is incrementally adjusted so as to keep β constant.
- for $\beta = 90°$ (transverse plane strain), the rate of axial displacement is prescribed (0.002mm/s) while a zero torque is imposed.

The non-proportional loading experiments involved two proportional loading steps:

- Pre-loading: the specimen is pre-loaded either in compression ($\beta = -90°$), tension ($\beta = +90°$) or torsion ($\beta = 0°$) using the actuator settings as for proportional loading. The pre-loading is monitored by 3DIC, and is stopped when the equivalent plastic strain on the symmetry plane of the gage section surface reaches approximately 5%.
- Elastic unloading: the specimens are unloaded to zero force and torque.
- Re-loading: The pre-deformed specimens are re-loaded all the way to fracture under proportional loading for either torsion ($\beta = 0°$), uniaxial tension ($\beta = 55°$) and plane strain tension ($\beta = 90°$). As during the first phase of loading, the corresponding actuator settings for proportional loading are used.

In sum, seven non-proportional experiments are performed. Fig. II-1 shows a summary of loading paths in terms of the relative shoulder motions u and θ. The measured force-displacement and torque-rotation curves are plotted in dashed lines in Fig. II-2 (proportional loading) and Fig. II-3 (non-proportional loading). For the latter, the pre-loading curves (pre-

compression, pre-torsion or pre-tension) are not shown as these match the corresponding recordings for proportional loading shown in Fig. II-2.

All force-displacement curves increase monotonically, and drop abruptly with the onset of specimen fracture. No sign of necking prior to fracture is observed in any of the experiments performed. Note that fracture initiated in all experiments before reaching a maximum in axial force or torque. The force and torque measurements exhibit a Portevin-Le-Chatelier type of serration as the gage section begins to deform plastically for $\beta = 69.5°$ and $\beta = 90°$. It was shown in literature that for a fixed strain rate and temperature, an increase in stress triaxiality leads to more important PLC serrations (Wagner et al [87], Benallal et al [88]).

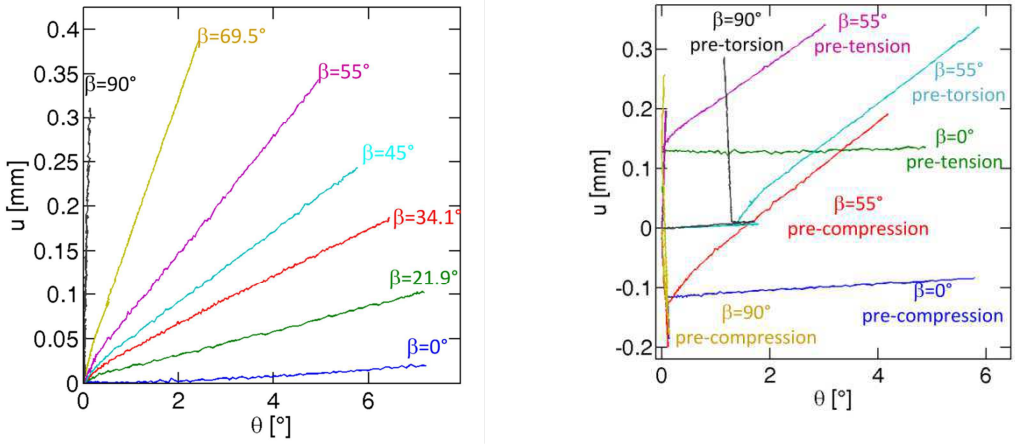

(a) (b)

Fig. II-1 Applied axial displacement and rotation histories: (a) proportional loading experiments, (b) non-proportional loading experiments.

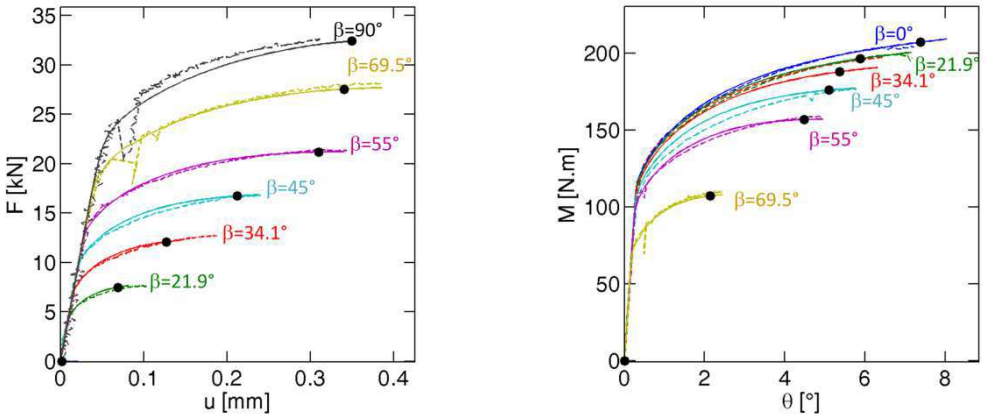

(a) (b)

Fig. II-2 Force-displacement and torque-rotation curves for proportional loading. Dotted lines: experimental data. Solid lines: simulations.

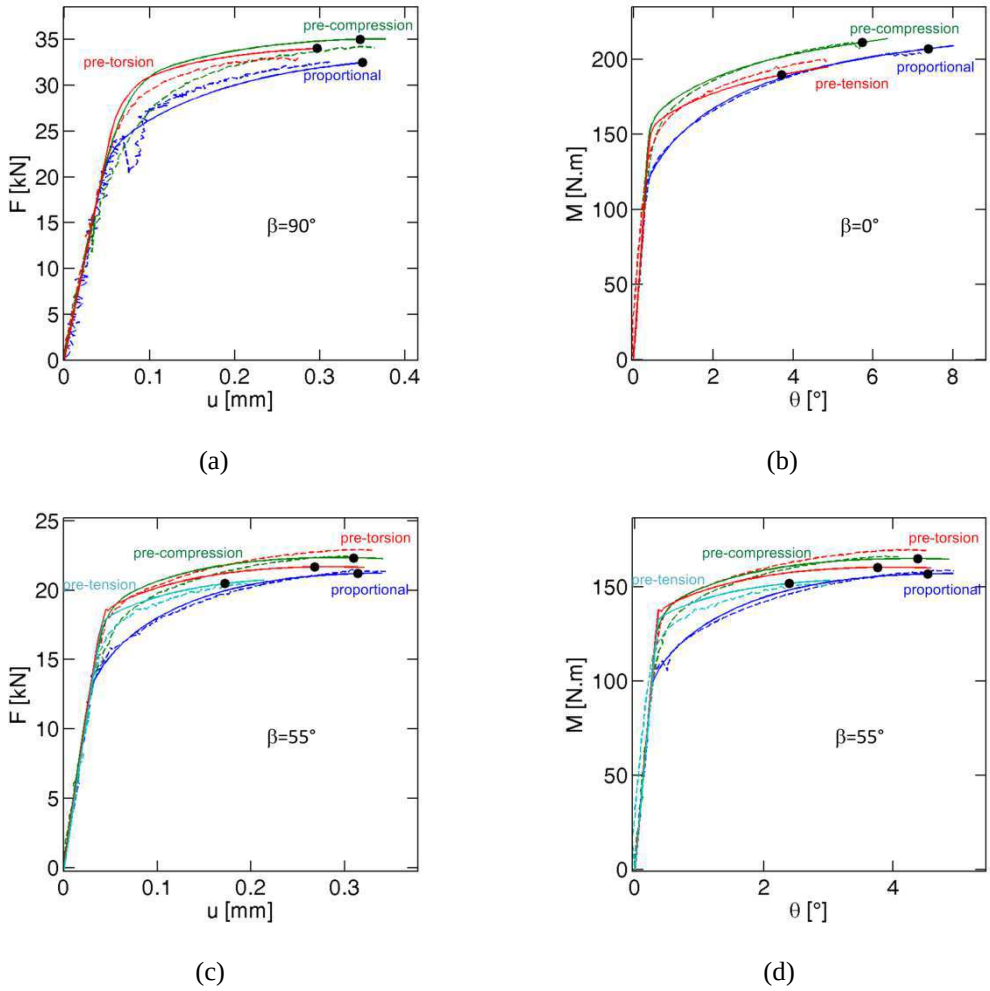

Fig. II-3 Force-displacement and torque-rotation curves for non-proportional loading. Dotted lines: experimental data. Solid lines: simulations.

2. Hybrid experimental-numerical results

As discussed in Chapter I, the direct estimation of the stress state and the strains to fracture based on surface strain measurements provides only a poor approximation of the loading path to fracture. As an alternative, we perform a finite element simulation of each experiment to obtain accurate estimates of the loading paths to fracture.

1.1. Plasticity model

Due to the apparent initial isotropy and the moderate strains involved in our fracture experiments on aluminum 2024-T351, an isotropic plasticity model is employed to describe

the material response. Formally, the yield surface is defined in terms of the Hosford [89] equivalent stress $\bar{\sigma}_{Hf}$ and a deformation resistance k,

$$f(\boldsymbol{\sigma}) = \bar{\sigma}_{Hf} - k = 0 \tag{2.1}$$

with

$$\bar{\sigma}_{Hf} = \left(\frac{1}{2} \left((\sigma_1 - \sigma_2)^p + (\sigma_1 - \sigma_3)^p + (\sigma_2 - \sigma_3)^p \right) \right)^{1/p} \tag{2.2}$$

In the definition of the Hosford equivalent stress, σ_1, σ_2 and σ_3 are the ordered principal values of the Cauchy stress tensor; p is the Hosford exponent which is a real within the interval $1 \leq p \leq \infty$. For the two limiting cases $p = 1$ and $p = \infty$, the Tresca yield surface is retrieved, while for $p = 2$ and $p = 4$, the Mises yield surface is retrieved (Fig. II-4a).

Isotropic hardening is defined through a linear combination of the Swift and Voce laws,

$$k = k[\bar{\varepsilon}_p] = k_0 + Q\left(1 - e^{-b\bar{\varepsilon}_p}\right) + A(\bar{\varepsilon}_p + \varepsilon_0)^n \tag{2.3}$$

with the Swift parameters $\{A, \varepsilon_0, n\}$ and the Voce parameters $\{k_o, Q, b\}$.

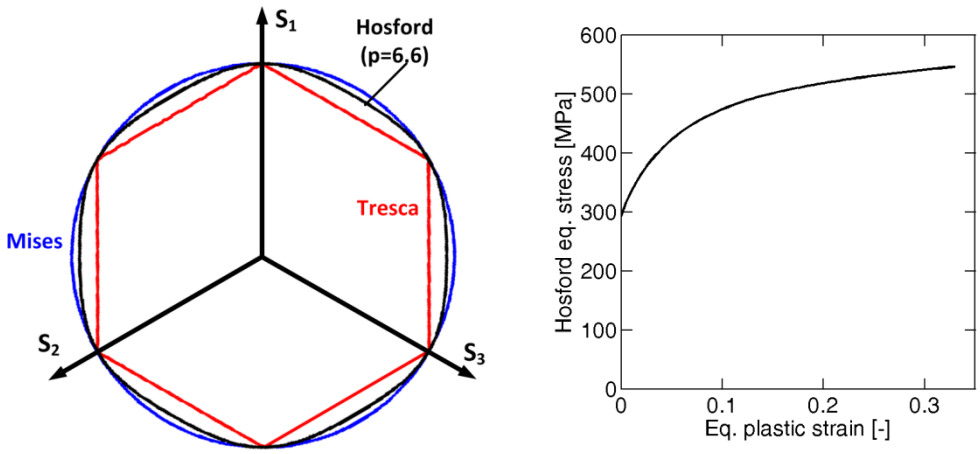

(a) (b)

Fig. II-4 (a) Yield surfaces plotted in the Π-plane : Mises, Tresca and the identified Hosford surface. (b) Hardening curve for aluminum 2024-T351 identified by inverse analysis.

2.1. Finite element model

The tests are simulated using Abaqus Standard 6.9EF2 in conjunction with the Zmat material library (Centre de Materiaux, Ecole des Mines, France). The finite element model is shown in Fig. I-1b. The part of the specimen lying between A and B is discretized using four-node generalized axisymmetric elements (CGAX4), which account for twist around the z-

axis. Based on a study of the mesh-convergence with respect to the local deformation fields, an element size of $25\mu m$ is chosen within the gage section. The axial and rotational displacement of two reference nodes (N1 and N2 in Fig. I-1b) is coupled to those of the top and bottom surface of the model. Displacements and loads are applied on N1, while node N2 is fully clamped.

One hundred implicit time steps are performed to simulate proportional loading. Closely mimicking the experimental procedure, the boundary conditions for proportional loading are applied as follows:

- for $\beta = 0°$, θ is imposed on *N1* as measured by 3DIC, while zero axial load is imposed on *N1*
- for $21.9° \leq \beta \leq 55°$, the rotation θ is imposed on *N1* as measured by 3DIC. A numerical sensor is created to get the value of the torque, and the UAMP subroutine is used to apply the correct proportion of force on *N1*.
- for $\beta = 69.5°$, the displacement u is imposed on *N1* as measured by 3DIC. A numerical sensor is created to get the value of the force, and the UAMP subroutine is used to apply the correct proportion of torque on *N1*.
- for $\beta = 90°$, the displacement u is imposed on *N1* as measured by 3DIC, while zero torque is imposed on *N1*·

For non-proportional loading, 100 time implicit time steps are performed during each phase of loading. Recall that the first phase involves pre-compression, pre-torsion or pre-tension and unloading applying either u (pre-compression or pre-tension) or θ (pre-torsion) as measured by 3DIC. Then, for the second step, the boundary conditions are applied similarly to those of proportional loading for $\beta=0°$, $\beta=55°$ and $\beta=90°$.

2.2.Identification of the plasticity model parameters

The six hardening parameters $\{A,\varepsilon_0,n,k_o,Q,b\}$ are first identified using the stress-strain curve obtained from uniaxial tension tests on dogbone specimens along the L direction of the bar. Then, the plasticity parameter p is identified through inverse analysis, while the hardening parameters are refined, by minimizing the difference between the measured and computed force-displacement and moment-rotation curves for proportional loading, as

explained in Chapter I (section 3.3). The final set of parameters corresponding to the hardening curve and the plasticity parameter are shown in Fig. II-4 and listed in Tab. II-2. Good agreement of the experimental curves (dashed lines) and the simulation results (solid lines) is observed for all biaxial loading angles for proportional loading (Fig. II-2). Furthermore, despite the simplicity of the hardening model, the model also provides reasonable predictions of the global specimen response to non-proportional loading (compare solid and dashed lines in Fig. II-3).

p	A (MPa)	ε_o	n	k_o (MPa)	Q (MPa)	b
6.6	357.8	0.00795	0.189	149.5	105.2	18.9

Tab. II-2 Plasticity model parameters identified by inverse analysis

2.3.Location of onset of fracture

It is assumed that fracture initiates at the instant of a drop in the measured force-displacement curves. An attempt is made to identify the location of onset of fracture based on (1) photographs of the specimens right after the onset of fracture (Fig. II-5) and (2) SEM pictures of the fracture surfaces (Fig. II-6). In particular, abrasive marks on the latter are seen as indicator of the zones where fracture initiated. For proportional loading within the range $0° \leq \beta \leq 45°$, and for selected cases of non-proportional loading ($\beta=0°$ after pre-compression, $\beta=0°$ after pre-tension, $\beta=55°$ after pre-torsion), the upper and lower parts of the specimen remained partially attached despite the abrupt load drop. The z-coordinate of the location of onset of fracture can therefore be determined from the pictures of the specimen (e.g. Fig. II-5a). For all other tests, the specimen separated in two parts brutally as the loads dropped. With regards to the location of onset of fracture, the following observations are made:

- Fracture initiated near the fillet radius for $0° \leq \beta \leq 34.1°$ (Fig. II-5a). Furthermore, SEM observations provide evidence that crack propagated earlier near the outer surface, where clear abrasive marks can be seen, and that the inner surface was the last to fail, as shear dimples can still be seen near the internal radius (Fig. II-6a). For non-proportional $\beta=0°$ (after pre-compression, after pre-tension) (Fig. II-5d) and $\beta=55°$ after pre-tension (Fig. II-5e) and after pre-compression, the crack also clearly initiated near the fillet radius.

- For proportional loading within the range $45° \leq \beta \leq 69.5°$, the crack meanders within a narrow band around the symmetry plane (Fig. II-5b). Abrasive marks as well as dimples are visible on many regions of the fracture surface for proportional $\beta=45°$ and 55° and do not allow for the determination of the radial coordinate of the location of onset of fracture (Fig. II-6b). Almost no abrasive marks for $\beta=69.5°$.
- For proportional $\beta=90°$, the crack meanders within a narrow band near the upper fillet (Fig. II-5c). Almost no abrasive marks are visible on the fracture surface (Fig. II-6c).
- For non-proportional $\beta=90°$ (after pre-compression and after pre-torsion), the crack meanders within the entire gage section (i.e. between the upper and lower fillet, see Figs. 6f) with no visible abrasive marks on the SEM pictures of the fracture surface.
- For $\beta=55°$ after pre-torsion, the crack meanders between the lower fillet and the symmetry plane (Fig. II-5g).

The corresponding spatial distributions of the equivalent plastic strain within the specimen gage section as obtained from finite element analysis are shown in Fig. II-7 for all experiments performed. Observe that the locations of onset of fracture identified experimentally (which was only possible for $\beta=0°$ proportional and non-proportional, and for $\beta=55°$ after pre-tension and pre-compression) coincide with the location of maximum equivalent plastic strain in the simulations. For each experiment, the loading path to fracture is therefore extracted at the integration point which featured the highest equivalent plastic strain at the instant of onset of fracture. The corresponding points are highlighted in Fig. II-7.

2.4.Loading paths to fracture

In this section, we are interested in the stress state history to fracture during the tests.

As mentioned in the previous subsection, the evolutions of η, $\bar{\theta}$ and $\bar{\varepsilon}_p$ are extracted at the integration point where the Hosford equivalent plastic strain is maximal. The corresponding loading paths to fracture in the $(\eta,\bar{\varepsilon}_p)$ and $(\bar{\theta},\bar{\varepsilon}_p)$-planes are shown in Fig. II-8 for proportional loading. Observe that the stress state remains remarkably constant throughout the experiments. The highest ductility (i.e. strain to fracture) ductility is achieved for $\beta=0°$ ($\bar{\varepsilon}_f = 0.29$). The lowest ductility is observed for $\beta = 90°$ ($\bar{\varepsilon}_f = 0.13$). Between the

limit stress states of pure shear ($\beta = 0°$) and plane strain tension ($\beta = 90°$), the present results suggest a local maximum in ductility for uniaxial tension ($\beta = 55°$, $\bar{\varepsilon}_f = 0.24$).

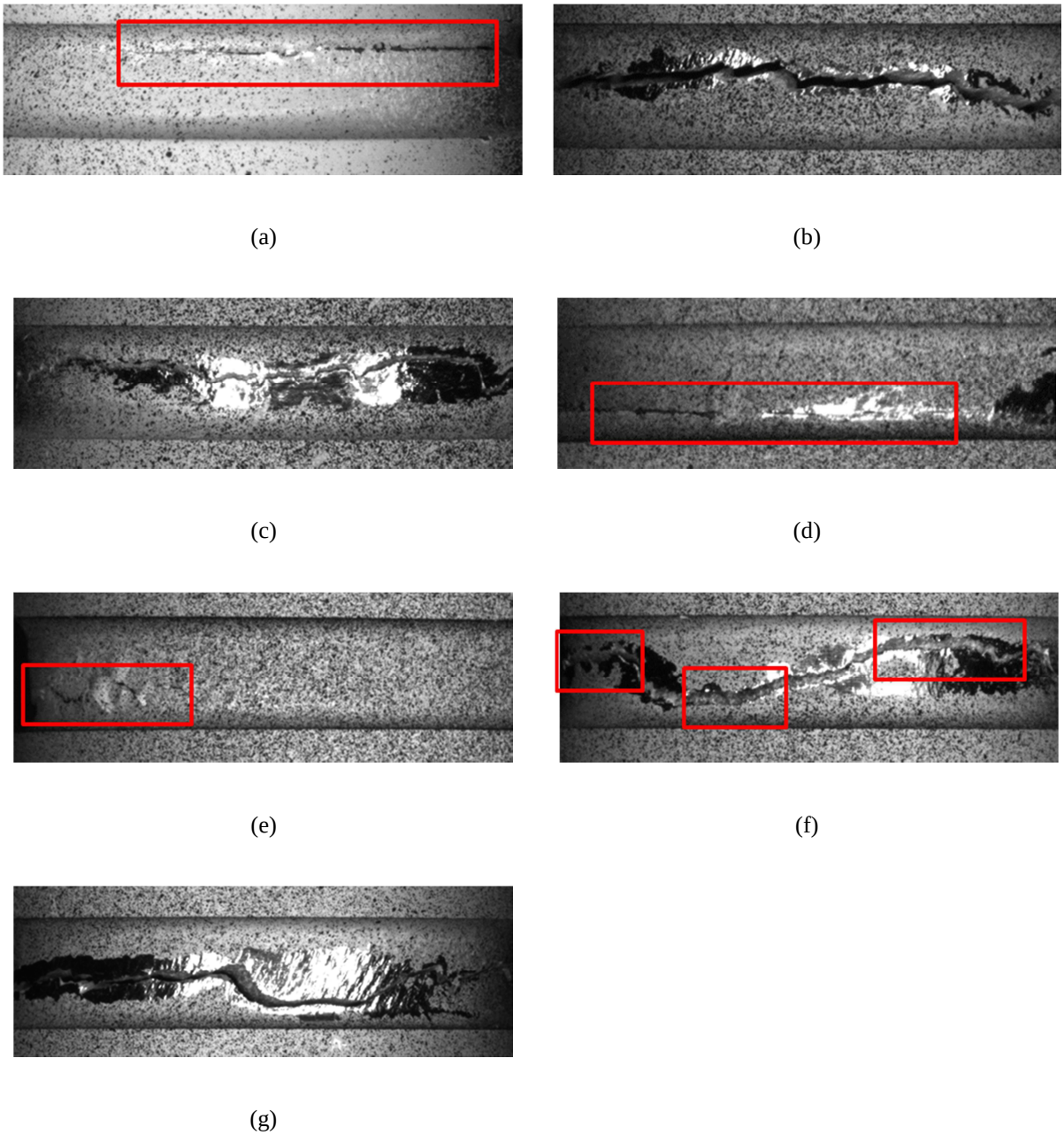

(a) (b) (c) (d) (e) (f) (g)

Fig. II-5 Pictures of a few broken specimens (a) proportional β=0° (b) proportional β=55° (c) proportional β=90° (d) β=0° with pre-compression (e) β=55° with pre-tension (f) β=90° with pre-torsion (g) β=55° with pre-torsion.

The loading paths for non-proportional loading (Fig. II-9) elucidate the effects of pre-compression, pre-torsion and pre-tension on the strain to fracture for pure shear ($\beta = 0°$), uniaxial tension ($\beta = 55°$), and plane strain tension ($\beta = 90°$):

- Applying pre-compression increases the material ductility in all cases. For β=0°, the strain to fracture increases from 0.29 (proportional loading) to 0.32 (after pre-compression). For $\beta = 55°$, it increases from 0.24 to 0.27. The most significant increase is observed for $\beta = 90°$: the ductility increases from 0.13 to 0.24, i.e. by more than 80%.
- Applying pre-torsion also appears to increase the ductility: from 0.24 to 0.29 for β=55°, and from 0.13 to 0.18 for β=90°.
- Applying pre-tension appears to decrease the ductility. The strain to fracture decreases from 0.29 to 0.25 for β=0°, and from 0.24 to 0.19 for β=55°.

A summary of these results in reported in Tab. II-3 and Tab. II-4.

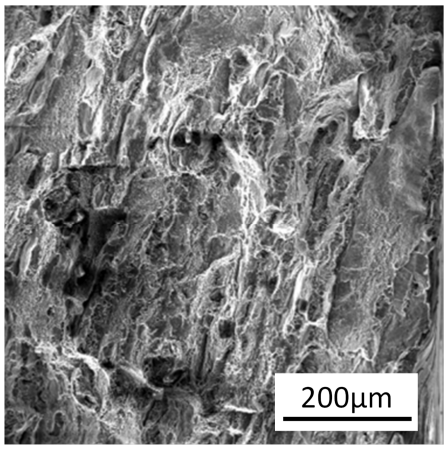

(a)

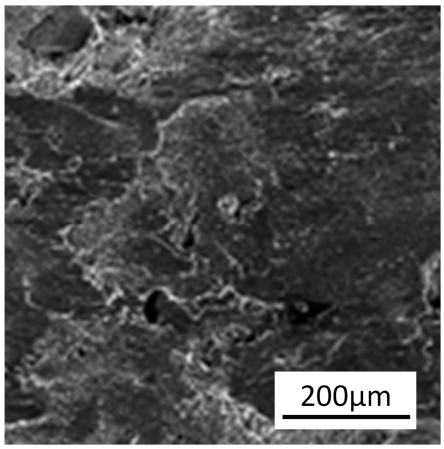

(b)

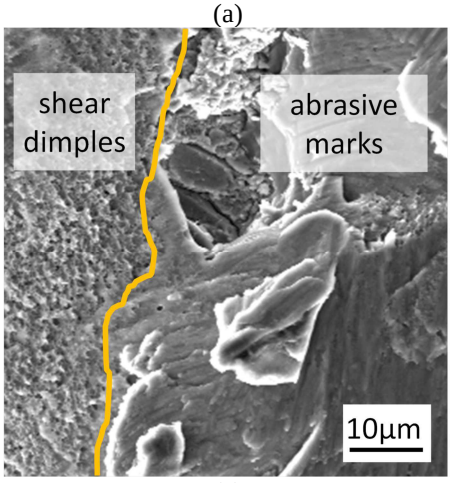

(c)

Fig. II-6 SEM view of fracture surfaces: (a) dimpled surface as observed for β=90°, (b) abrasive marks as observed for β=55°, (c) shear dimples and abrasive marks observed for β=0°.

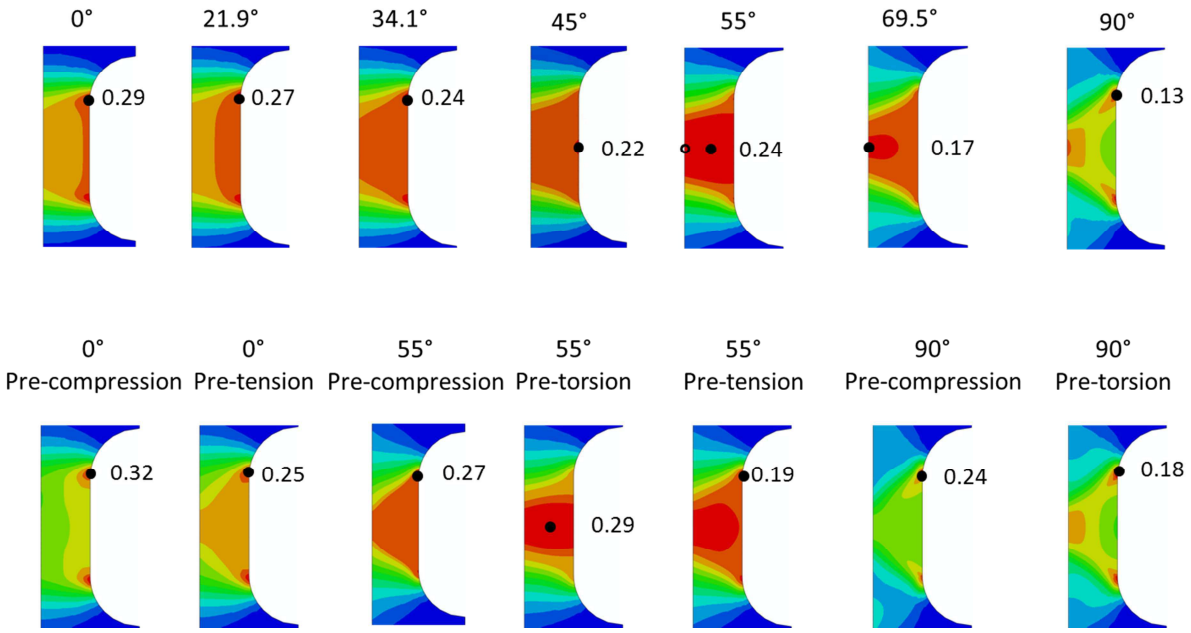

Fig. II-7 Equivalent plastic strain fields from FEA at the onset of fracture. The solid black dots indicate the location of maximum equivalent plastic strain at the onset of fracture, defined as the sudden load drop. The open black dot indicates the location where D first reaches the value 1, if different from the location of maximum equivalent plastic strain.

	$\langle\eta\rangle$	$\langle\overline{\theta}\rangle$	$\bar{\varepsilon}_{final}$	η_{final}	$\overline{\theta}_{final}$
0°	0.003	0.01	0.29	0.004	0.01
21.9°	0.14	0.39	0.27	0.14	0.40
34.1°	0.22	0.62	0.24	0.22	0.63
45°	0.25	0.74	0.22	0.25	0.73
55°	0.33	0.98	0.24	0.35	0.98
69.5°	0.45	0.57	0.17	0.44	0.60
90°	0.57	0.11	0.13	0.58	0.09

Tab. II-3 Summary of results for proportional loading.

	$\langle\eta\rangle_{step1}$	$\langle\bar{\theta}\rangle_{step1}$	$\langle\eta\rangle_{step2}$	$\langle\bar{\theta}\rangle_{step2}$	$\bar{\varepsilon}_{pre-loading}$	$\bar{\varepsilon}_{final}$	η_{final}	$\bar{\theta}_{final}$
0° pre-compression	-0.58	-0.07	0.04	0.12	0.071	0.32	0.007	0.019
0° pre-tension	0.57	0.13	-0.04	-0.11	0.074	0.25	0.0003	0.0006
55° pre-compression	-0.58	-0.07	0.36	0.94	0.071	0.27	0.38	0.89
55° pre-torsion	0.002	0.005	0.34	0.99	0.042	0.29	0.36	0.98
55° pre-tension	0.57	0.13	0.34	0.94	0.075	0.19	0.37	0.91
90° pre-compression	-0.58	-0.07	0.58	0.11	0.071	0.24	0.58	0.08
90° pre-torsion	0.002	0.005	0.58	0.08	0.071	0.18	0.58	0.08

Tab. II-4 Summary of results for non-proportional loading

The loading path to fracture for $\beta = 55°$ (after pre-torsion) is shown as a dashed line in Fig. II-9b to indicate a lack of certainty in this hybrid experimental-numerical result. Fig. II-3c shows a substantial difference in the hardening of the measured and computed force-displacement curves (compare solid and dashed red lines). In particular, the simulation curve exhibits a maximum prior to the onset of fracture which is an indicator of localization within the gage section. Consequently, the strain to fracture reported in Fig. II-9b for this loading case is expected to be too large. Another particular feature of this experiment is that the maximum equivalent plastic strain is reached away from the specimen surface, and not near the fillet, like all other tests. The loading path to fracture therefore needs to be extracted at a point where the pre-loading had not yet reached an equivalent plastic strain of 0.07.

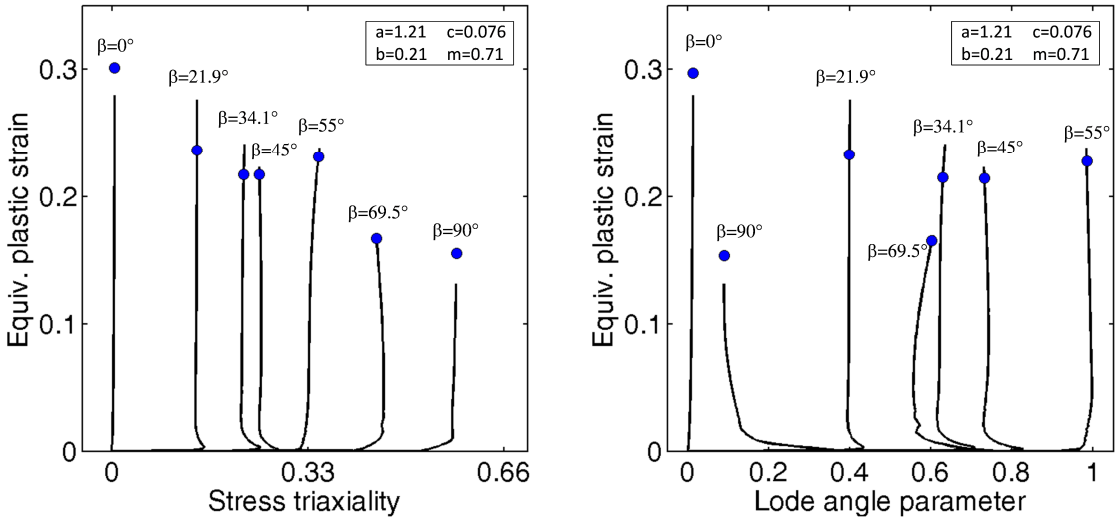

(a) (b)

Fig. II-8 Loading paths for proportional loading. Black line represent the loading history computed from FE simulations, while blue dots represent the fracture strain indicated by the Hosford-Coulomb model (a=1.21, b=0.21, c=0.076, m=0.71).

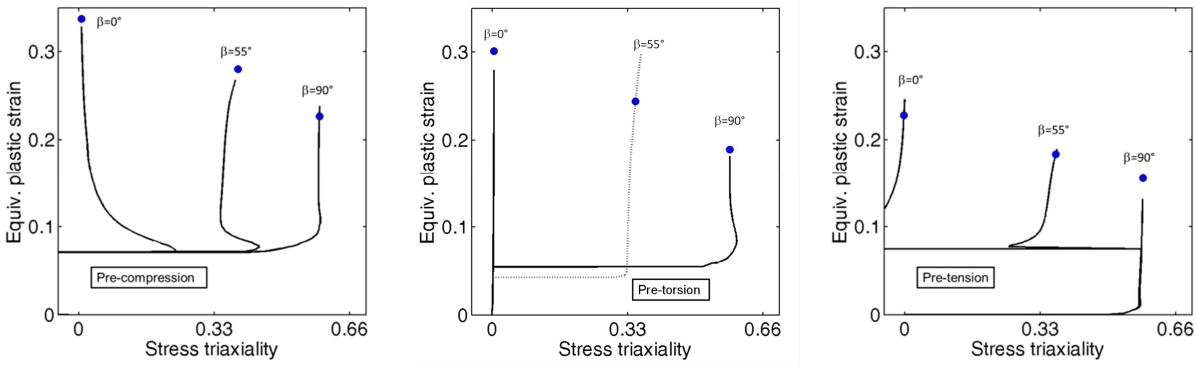

(a) (b) (c)

Fig. II-9 Loading paths for non-proportional loading. Black line represent the loading history computed from FE simulations, while blue dots represent the fracture strain indicated by the Hosford-Coulomb model. Tests with (a) pre-compression (b) pre-torsion (c) pre-tension (a=1.21, b=0.21, c=0.076, m=0.71).

3. Hosford-Coulomb fracture initiation model

The phenomenological HC fracture initiation model (Mohr and Marcadet [53]) calibrated and validated in Chapter I in the case of 36NiCrMo16 steel, will also be used here for aluminum 2024-T351. In the present work, a self-consistent framework will be used to account for the plasticity –which, for this material, is not a Levy – Von Mises model anymore. Furthermore, it will be extended further to account for the effect of severe loading path changes.

3.1. Effect of stress state

We refer to Eq. (1.32) for the expression of the HC criterion in the mixed stress-strain space $\{\eta, \bar{\theta}, \bar{\varepsilon}_p\}$ for a von Mises plasticity material with isotropic hardening. Here, a subsequent transformation is performed for a Hosford plasticity material. Thus, the Hosford equivalent stress at the onset of fracture reads:

$$\bar{\sigma}_{Hf} = \frac{\sigma_c \left\{ \frac{1}{2} \left((f_1 - f_2)^p + (f_1 - f_3)^p + (f_2 - f_3)^p \right) \right\}^{\frac{1}{p}}}{\left\{ \frac{1}{2} \left((f_1 - f_2)^a + (f_1 - f_3)^a + (f_2 - f_3)^a \right) \right\}^{\frac{1}{a}} + c(f_1 + f_3 + 2\eta)} \tag{2.4}$$

Using the isotropic hardening law (Eq. (2.3)), the resulting expression of the Hosford equivalent strain to fracture for proportional loading, $\bar{\varepsilon}_f^{pr}$ is obtained:

$$\bar{\varepsilon}_p^{pr}[\eta, \bar{\theta}] = k^{-1} \left(\frac{k[\lambda](1+c) \left\{ \frac{1}{2} \left((f_1 - f_2)^p + (f_1 - f_3)^p + (f_2 - f_3)^p \right) \right\}^{\frac{1}{p}}}{\left\{ \frac{1}{2} \left((f_1 - f_2)^a + (f_1 - f_3)^a + (f_2 - f_3)^a \right) \right\}^{\frac{1}{a}} + c(f_1 + f_3 + 2\eta)} \right) \tag{2.5}$$

In the above operation, without changing the mathematical form of the model, we substituted the coefficient λ through λ in a way that λ is equal to the strain to fracture for uniaxial tension. In summary, the above isotropic fracture initiation model for proportional loading features three free parameters: a, λ and c. Fig. II-10 shows a plot of the "fracture surface" defined by Eq. (2.5). The dependence on the stress triaxiality is controlled by the friction parameter $c \geq 0$ with stress triaxiality independence for $c = 0$. The parameter λ (strain to fracture for uniaxial tension) controls the overall strain to fracture.

The corresponding criterion for plane stress conditions is shown in Fig. II-11. Recall that the Lode angle parameter is a function of the stress triaxiality in the case of plane stress. Irrespective of the choice of parameters, the model features the characteristic plane strain valley for biaxial tension $(1/3 \leq \eta \leq 2/3)$, i.e. the strain to fracture is the lowest for plane strain tension $(\eta = 1/\sqrt{3})$, and the highest for uniaxial $(\eta = 1/3)$ and equi-biaxial tension $(\eta = 2/3)$.

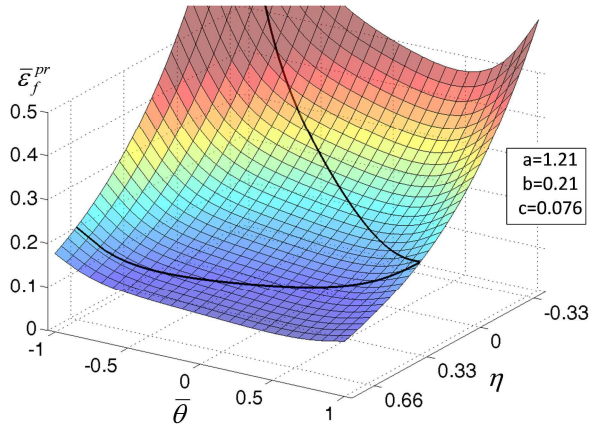

Fig. II-10 Hosford-Coulomb fracture envelope identified for aluminum 2024-T351 (a=1.21, b=0.21, c=0.076, m=0.71)

3.2. Modeling of the effect of loading path

3.2.1. Linear damage accumulation law

The direct application of (2.5) as fracture initiation criterion is only valid for proportional loading (constant stress triaxiality and Lode angle parameter throughout loading). For non-proportional loading, a linear damage accumulation law is used (Fischer et al., [74]). Let D denote a damage indicator of initial value $D=0$; fracture is then assumed to initiate when $D=1$ after accumulating damage according to the evolution equation

$$dD = \frac{d\bar{\varepsilon}_p}{\bar{\varepsilon}_f^{pr}[\eta,\bar{\theta}]} \tag{2.6}$$

The term damage is introduced in quotes as D only partly represents physical damage due to progressive void nucleation (which triggers the localization of deformation at the microscale, and whose effect on the plastic material response is neglected). The above evolution is linear in the sense that D is a linear function of the equivalent plastic strain for proportional loading.

To illustrate the effect of the loading path on the strain to fracture, we computed the fracture envelope for proportional loading all the way to fracture after three different pre-loadings up to a strain of 0.07 (Fig. II-11b):

1. Pre-compression: the strain to fracture for proportional loading at $\eta = -1/\sqrt{3}$ is much higher than that for proportional loading within the range $0 \leq \eta \leq 2/3$ (a). As a result, less damage is accumulated during pre-loading as compared to direct loading within the range $0 \leq \eta \leq 2/3$. The fracture envelope for two-step loading with pre-compression (red curve) therefore lies above the envelope for single-step proportional loading (black curve). In other words, the total equivalent plastic strain that can be accumulated prior to the onset of fracture increases after compression.
2. Pre-tension: plane strain tension is the most critical stress state. As a result, more damage is accumulated during pre-tension as compared to loading at any other plane stress state. The fracture envelope for two-step loading with pre-tension (blue curve) therefore lies below the envelope for single-step proportional loading (black curve). In other words, pre-loading under plane strain tension reduces the overall ductility of the material.
3. Pre-torsion: pre-loading under torsion increases the ductility for subsequent proportional loading at stress triaxialities above 0.

The above model response is in remarkable qualitative agreement with the experimental observations for two-step loading. The comparison with the experimental results shows that the main effect of pre-loading on the subsequent fracture response under proportional loading is captured by the model, i.e. pre-compression and pre-torsion increase the ductility, whereas pre-tension decreases the ductility.

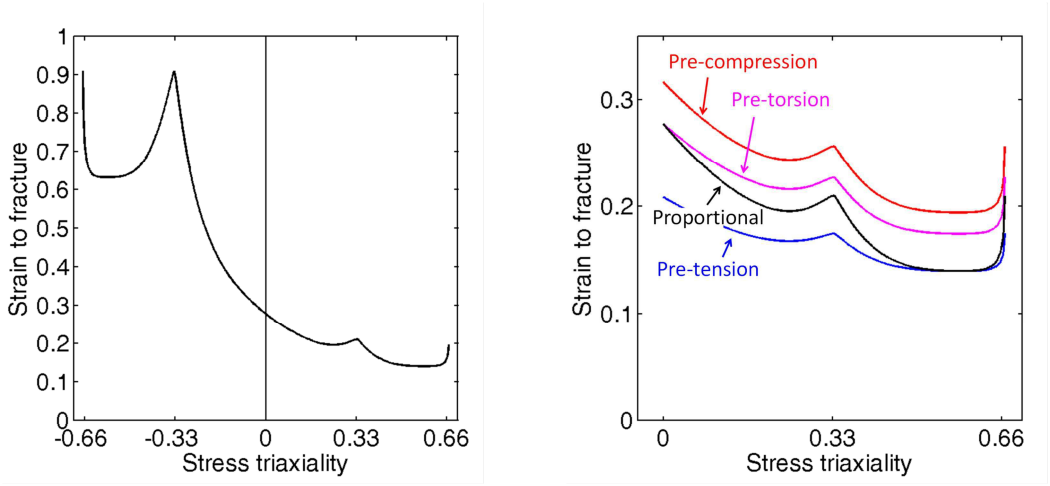

(a) (b)

Fig. II-11 (a) Hosford-Coulomb fracture envelope for proportional plane stress loading; (b) Fracture envelope for $\eta \geq 0$ after pre-loading up to $\bar{\varepsilon}_p = 0.07$ under uniaxial compression ($\eta = -0.33$, red curve), uniaxial tension ($\eta = 0.33$, blue) and transverse plane strain tension ($\eta = 0.58$, magenta). (a=1.21, b=0.21, c=0.076, m=0.71)

3.2.2. Non-linear damage accumulation law

The application of the linear damage accumulation law to our experimental data for non-proportional loading resulted only in poor estimates of the strain to fracture. A non-linear damage accumulation model is proposed to address this issue. Instead of assuming a linear relationship between the damage indicator and the equivalent plastic strain for proportional loading (black curve in Fig. II-12), we assume a non-linear relationship as shown by one of the dashed curves in Fig. II-12. In differential form, the corresponding evolution equation reads

$$dD = m\left(\frac{\bar{\varepsilon}_p}{\bar{\varepsilon}_f^{pr}[\eta,\bar{\theta}]}\right)^{m-1} \frac{d\bar{\varepsilon}_p}{\bar{\varepsilon}_f^{pr}[\eta,\bar{\theta}]} \tag{2.7}$$

with the exponent $m>0$. Fig. II-12b shows the damage evolution for a torsion experiment (i) after pre-loading under compression up to $\bar{\varepsilon}_p = 0.07$, (ii) pre-loading under tension up to $\bar{\varepsilon}_p = 0.07$, and (iii) without any pre-loading.

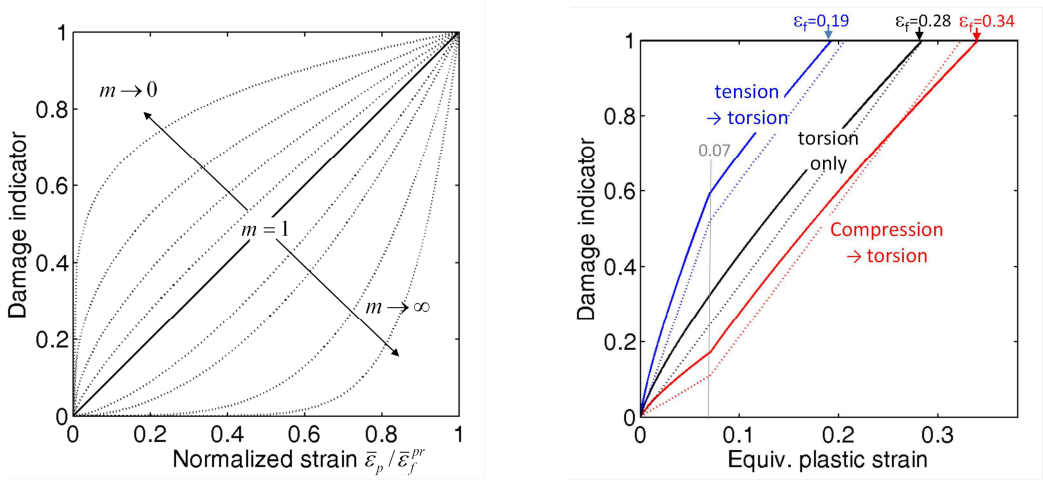

(a) (b)

Fig. II-12 Non-linear damage accumulation law: (a) Effect of the exponent m including the special case of linear damage accumulation for m=1, (b) Evolution of damage in a torsion experiment after pre-loading under tension (blue) and compression (red), as well as for proportional loading (black); the dashed lines show the predictions for linear damage accumulation (m=1), the solid lines depict the results for non-linear damage accumulation (m=0.8).

3.3. Model calibration

In a first step, the fracture initiation model parameters $\{a, \lambda, c\}$ are calibrated based on the proportional experiments for $\beta = 0°$, $\beta = 55°$ and $\beta = 90°$ assuming $m = 1$. Recall that the parameter λ is equal to the strain to fracture for uniaxial tension. Consequently, the strain to fracture for $\beta = 55°$ provides a good starting value for λ. A quick optimization showed that the parameters $a = 1.13$, $\lambda = 0.24$ and $c = 0.085$ provide an exact prediction of the strain to fracture for all three proportional experiments.

In second step, all four model parameters $\{a, \lambda, c, m\}$ are identified through inverse analysis using the loading paths for non-proportional loading shown in Fig. II-9. The exact integral criterion (2.7) is evaluated for each calibration experiment. The difference between the experimental and predicted strains to fracture is then minimized using a derivative-free simplex algorithm. The "optimal" model parameters are $a = 1.21$, $\lambda = 0.21$, $c = 0.076$ and $m = 0.71$.

3.4. Model validation

The comparison of the experimental and predicted strains to fracture allows for a first validation of the fracture initiation model. Recall that the end points of the loading paths

shown in Fig. II-8 and Fig. II-9 correspond to the measured instants of onset of fracture. The corresponding model predictions are shown as solid blue dots. Overall the model predictions agree well with the experimental results. The largest differences are observed for β=21.9° ($\bar{\varepsilon}_f^{\exp} = 0.29$ vs. $\bar{\varepsilon}_f^{\mathrm{mod}} = 0.24$) under proportional loading (Fig. II-8), and for β=0° after pre-tension ($\bar{\varepsilon}_f^{\exp} = 0.29$ vs. $\bar{\varepsilon}_f^{\mathrm{mod}} = 0.24$) for non-proportional loading (Fig. II-9c).

The numerical simulations of all experiments are also repeated with the fracture initiation model active at each integration point. The predicted instants of onset of fracture are highlighted by solid black dots in Fig. II-2 and Fig. II-3. The overall agreement is good for all loading cases. For proportional loading, the displacement/rotation to fracture is slightly overestimated for $\beta = 90°$ and $\beta = 0°$, and underestimated for all other cases. This result is consistent with the "local" validation shown in Fig. II-8, where the strain to fracture is overestimated for $\beta = 90°$ and $\beta = 0°$. This consistency may be seen as a partial validation of the assumption of the location of onset of fracture made during model calibration. It is validated more accurately by comparing the assumed location of onset of fracture (solid dots in Fig. II-7) with the locations at which the damage indicator reached unity first (open dots in Fig. II-7). These locations coincide for all loading cases except for $\beta = 55°$ where the model predicts fracture initiation on the inner specimen surface while the maximum equivalent plastic strain is reached within the bulk of the gage section.

4. Discussion

As outlined in the introduction, the experimental results of Bao and Wierzbicki [5] (B&W) on aluminum 2024-T351 served frequently as the basis for the validation of fracture initiation models in the past. It is therefore worth confronting the present results on aluminum 2024-T351 with those from Bao and Wierzbicki (B&W).

Following the processing procedure proposed by Bao and Wierzbicki (B&W), we calculated the average stress triaxiality throughout loading,

$$< \eta >= \frac{1}{\bar{\varepsilon}_f} \int_0^{\bar{\varepsilon}_f} \eta (d\bar{\varepsilon}_p) \tag{2.8}$$

and computed the von Mises equivalent plastic strain to fracture,

$$\bar{\varepsilon}_{vm}^{f} == \int_{0}^{\bar{\varepsilon}_f} \left(\frac{\bar{\sigma}_{Hf}}{\bar{\sigma}} \right) d\bar{\varepsilon}_p \tag{2.9}$$

The corresponding data points $\{<\eta>, \bar{\varepsilon}_{vm}^{f}\}$ from our proportional loading experiments (blue dots) are plotted next to the Bao-Wierzbicki (B&W) data (red dots) for the same range of average stress triaxialities in Fig. II-13. We also included the calibrated Hosford-Coulomb envelope for plane stress (blue line) as well as the criterion suggested by B&W[2] (red line) in Fig. II-13. The quantitative comparison reveals that the strains reported by B&W are often much higher (up to 0.46) as compared to the present tension-torsion results (up to 0.30). This might be possibly due to differences in the microstructures of the tested aluminum 2024-T351 alloys. More importantly, the B&W data suggests a dramatic decrease of the strain to fracture between uniaxial tension and pure shear, while our data suggests an increase in ductility instead. This qualitative discrepancy is particularly important as the decrease in ductility for pure shear reported by B&W motivated many recent theoretical developments. It is speculated that the experimental techniques employed by B&W might not have been fully adequate for measuring the strain to fracture:

- Uncertainty in the assumed location of onset of fracture: B&W used a flat specimen with cut-outs and thickness reduction for measuring the strain to fracture at low stress triaxialities. As pointed out by Mohr and Henn [90,56] and Dunand and Mohr [7], fracture in shear experiments on flat specimens is likely to initiate away from the specimen center at a stress state that is very different from pure shear. The processing of the experimental results based on the assumption of fracture initiation near the specimen center will result in an underestimation of the strain to fracture for pure shear (see data point ① in Fig. II-13). Unfortunately, the exact dimensions of the B&W specimen for shear testing have not been reported in the open literature which makes it difficult to validate or not the above speculation;
- Uncertainties in the displacement measurements: it appears that B&W measured the cross-head displacement to fracture for their shear-dominated experiments (data ① and ②). Extensometer measurements had probably not been possible due to the specimen shoulder rotation. The distance between the pin attachments was more than ten times longer than the gage section, i.e. a significant portion of the measured

[2] We encountered a small discrepancy between the curves shown in Fig. 20 of Bao and Wierzbicki [5] and the corresponding criteria given by Eqs. (8) and (9) of their paper. To ensure the continuity of the failure envelope at a stress triaxiality of 0.4, we adjusted the parameter of the criterion given by Eq. (9).

displacement to fracture is due to the deformation of the specimen shoulders and rigid body rotation. The accuracy of the extracted strain to fracture from such measurements depends on the accuracy of the mechanical model of the entire specimen and the testing system.

- Uncertainties in the boundary conditions: Figs. 10 and 11 of B&W's paper bring up questions regarding the rotational rigidity and alignment of the specimen grips. For example, the top and bottom parts of the axisymmetric specimens are no longer aligned after fracture. If the specimens were slightly bent during the tensile experiment, the strain to fracture calculated with an axisymmetric finite element model might actually be larger than that at the onset of fracture in the experiment. This argument could explain the reported high strains for axisymmetric tension (points ④ and ⑤ in Fig. II-13).

- Uncertainties in the post-necking response: B&W identified the stress-strain curve through inverse calibration using the force-displacement curve for smooth round bars as reference. The size of the zone of localized necking in their experiment was very small as compared to the extensometer length which results in a poor sensitivity of the cost function to variations in the strain field inside the neck. Small uncertainties in this procedure might have contributed to an overestimation of the strains to fracture for experiments ③ to ⑤ of B&W.

It is reemphasized that the above points are speculations only which need to be clarified by future research. Here, we continue our discussion by reviewing the experimental data of others. According to Luo et al. [91], Khan and Liu [78] measured an equivalent strain to fracture of 0.29 in torsion experiments on 2024-T351 aluminum. In their paper, Khan and Liu [78] also show that the strain measured through strain gages (0.2) is significantly lower than that observed in micrographs. Abi Akl [92] made use of various butterfly specimen geometries to perform shear experiments on aluminum 2024-T351. He found an equivalent plastic strain to fracture of about 0.3 irrespective of the specimen geometry.

Experimental data for other aluminum alloys also suggest a higher strain to fracture for pure shear than for uniaxial tension. For example, Mohr and Henn [90,56] observed an increase in ductility from uniaxial tension to pure shear in their results from butterfly specimens for a cast aluminum alloy. The experimental results from Bruenig et al. [93] for an unspecified aluminum alloy also show a higher ductility for pure shear than for uniaxial

tension. A more comprehensive experimental study has been performed for aluminum 6061-T6 by Haltom et al. [72]. Their tension-torsion tests generated 13 data points between pure shear and uniaxial tension that suggest a decrease in ductility as function of stress triaxiality in that range.

From a modeling point of view, our current understanding of the fracture initiation at low stress triaxialities leaves space for justifying the plausibility of the B&W results. Note that both the stress triaxiality and the Lode angle parameter decrease between uniaxial tension and pure shear. According to the Hosford-Coulomb model, there is a competition of the effects of stress triaxiality and Lode angle parameter: a decrease in stress triaxiality increases the ductility, a decrease in Lode angle from $\bar{\theta}=1$ to $\bar{\theta}=0$ decreases the ductility. For advanced high strength steels, both scenarios have been observed experimentally (see Mohr and Marcadet [53]). However, except for the results of B&W, all of the above experimental data for aluminum alloys suggests a higher strain to fracture for pure shear than for uniaxial tension.

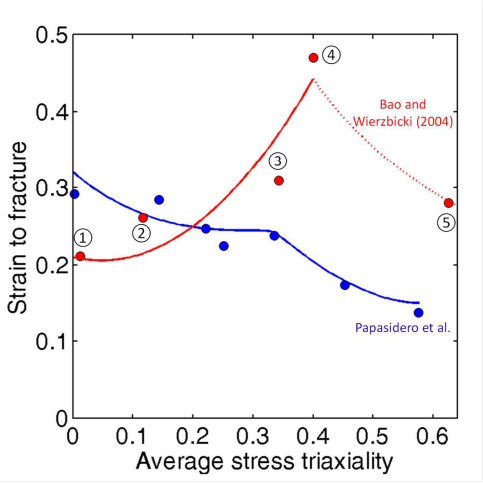

Fig. II-13 Comparison of present experimental results (blue data points) with experimental results of Bao and Wierzbicki [5] for the same aluminum alloy. Different from the previous figures, the von Mises equivalent plastic strain us shown on the ordinate. The solid (dashed) lines show the fracture envelopes as fitted to data for plane stress (axisymmetric) loading.

5. Conclusions

Tension-torsion experiments to fracture are performed on stocky tubular aluminum 2024 T351 specimens. Different loading conditions are applied: proportional loading conditions,

where the ratio between the axial force and the torque is kept constant throughout the tests, and non-proportional loading conditions, where a pre-loading – pre-compression, pre-shear or pre-tension – is applied. A hybrid experimental-numerical approach is used in both cases to investigate the effect of the stress state on the material ductility. The fracture locus obtained from proportional loading tests is compared with that obtained by Bao and Wierbicki [5] and an explanation is proposed to account for the discrepancies between the two fracture locuses. The pre-loading is shown to have a considerable effect on the material ductility. An extension of the Hosford-Coulomb fracture initiation model (Mohr and Marcadet [53]) using a non-linear accumulation damage rule is calibrated from part of the experiments, and is shown to predict fairly well the onset of fracture.

III. Ductile damage mechanisms and strain localization in 2024-T351 aluminum alloy and 36NiCrMo16 steel at low stress triaxiality

---

In this chapter, the ductile damage mechanisms of 2024-T351 aluminum alloy and 36NiCrMo16 steel are investigated at the microscopic scale for stress triaxialities lower than 1/3. To this purpose, combined tension and torsion tests are performed with the stocky tubular tension-torsion specimen used in Chapters I and II. These tests are run to fracture, or interrupted and followed by SEM observations. As the final failure is found to occur very quickly just before the end of the test, subsequent insight on damage mechanisms under pure shear loading is brought through direct monitoring during torsion tests in a SEM. The trend towards localized deformation –observed already at meso-scale for aluminum 2024-T351 but also at micro and sub-grain scale- increases as the stress triaxiality ratio decreases. A significant axial elongation is measured in both materials, even in torsion. This Swift effect might explain why most voids elongate in one direction and shrink in the orthogonal one but do not collapse and why some even grow in nominally pure shear loading. Quantitative data on damage in the aluminum alloy is obtained. The crystallographic texture and its evolutions are shown to play an important role in the steel: as stress triaxiality decreases, texture evolutions become more and more important and larger and larger clusters of grains sharing the same orientation form, this making shear bands development easier and easier. The coalescence mechanisms observed in aluminum 2024-T351 suggest that the use of the shear localization Hosford-Coulomb as a failure criterion is reasonable.

The participation of master student Sébastien LEPEER in the present work is acknowledged.

For several decades, advanced micromechanical studies have been performed to shed more light on ductile failure under low triaxialities, especially, shear-dominant loading. McClintock [94] analytical analysis of void growth in shear bands predicts that an initially circular void elongates in the direction of the first principal stress, rotates and tends to close. Sometimes, total closure is achieved (especially if compression exists), but past a certain void rotation angle, the hole opens up again. Anderson et al. [95] considered microcraks incled by 45° with respect to the shearing direction in their analysis of strain localization in shear. They found that the strain to localization depends on the crack size-to spacing ratio (the lower this ratio, the earlier the localization), crack face friction, material hardening but also, to a large extent, on the initial crack orientation. This important aspect should thus not be neglected in micromechanical models.

More recent numerical analyses resulting from homogenization (Danas and Ponte-Castañeda [96]) or unit cell analyses (Nielsen [47]) predict void collapse under pure shear. In Danas and Ponte-Castañeda [96], the void aspect ratio is predicted to vary by a factor of about 3-5 as the plastic strain increases. According to Nielsen [47] an initially spherical void elongates and collapses so much that it closes completely and the surfaces of the void touch. McVeigh et al [97] investigated numerically the evolution of voids under pure shear loading in a high strength steel, where damage occurs by TiC particles debonding. A unit-cell model containing a particle with an interfacial cohesion law showed that once debonding occurs, it propagates rapidly along the particle/matrix interface, and even under pure shear, undergoes limited growth, due to elastic deformation of the matrix and the presence of the particle, which props the void open and prevents it from collapsing altogether. They also observed that shear localization is to a large extent controlled by interactions between cavities, and therefore, strongly depends on the size-to-spacing ratio of the second-phase particles. Considering a cluster of prone-to-debonding particles under pure shear, they found that voids grow at about 45° to the shear plane, that particles are driven towards each other while voids turn and take a tail-like elongated form. Rahman et al [98] studied numerically void evolution and coalescence in simple shear as well, without considering particles embedded in a matrix, but laying emphasis on the effect of void shape and spacing on their evolution and coalescence. They found that when the voids are widely separated, they rotate significantly and the influence of their shape is very strong (prolate voids will favor coalescence); on the contrary, when the voids are close to each other, they can interact more easily and their shape and rotation are less important.

Although unit-cell models are very useful to analyze the effects of the stress state, void shape or spatial distribution on void growth and coalescence, to determine critical porosities or to discuss the quality of model predictions, they remain artificial microstructures and do not account for microstructural heterogeneity, nor for the fact that different microstructures may respond in diverse ways to a same loading. Hence the necessity of developing reliable experiments and post-processings to justify the choice of a ductile failure model, and provide the necessary data for models validation at the appropriate micro-scale. Recently, experimental studies investigated ductile failure micromechanims for low triaxialities and brought interesting insight, especially on strain localization through multi-scale strain measurements. Tucker et al. [99] investigated the effect of stress state on damage for three aluminum alloys: A356-T6, 5083-H131 and 6061-T6. They assessed the evolution of void density with respect to the effective strain. All three aluminums exhibited void nucleation, growth and coalescence. However, the void density levels and evolution rates differed for these materials which had been processed differently and possessed different microstructures and flow properties. Ghahremaninezhad and Ravi-Chandar [24] or Haltom et al. [72], who used changes in grain thickness to measure the strains at a small scale, for an aluminum 6061-T6. The former used Arcan specimens, and the latter used tubular tension-torsion specimens. The strain levels measured at the micro-scale were much higher than those measured on a macroscopic gage length. They observed evidences of strain localization in a very narrow band (a few hundreds of microns wide) and reported that void coalescence was limited to a very narrow region within the localized deformation band. Khan and Liu [78] performed pure torsion tests on thin-walled tubular specimens of 2024-T351 aluminum alloy and also reported shear localization into a 100µm-high layer adjacent to the fracture surface, and homogeneous deformation outside this layer. Taylor and Sherry [100] analyzed ductile fracture mechanisms of aluminum 2024-T351 using both synchrotron X-ray and focused ion beam tomography. They performed tensile tests on notched bars and pre-cracked CT specimens and observed post-mortem sections of broken specimens. Contrary to what was reported in literature they found that damage was quite diffuse in notched-specimens, as it extended over 4mm from the fracture surface. However, for CT specimens, damage was localized in a zone of 200µm adjacent to the fracture surface. They also noticed significant differences in damage mechanisms between the two geometries, as concerns cracking or debonding of dispersoids and the final stages of failure. They interpreted these differences in terms of stress and strain gradients, much more severe in the CT specimen than in the blunt-

notched bars. Therefore, specimen geometry can play a role in the mechanisms, distribution and evolution of damage, which complexifies the experimental studies in this field.

The present study aims at providing information of the same nature on strain localization and damage mechanisms in 36NiCrMo16 steel and 2024-T351 aluminum alloy at low stress triaxiality and, in the latter, quantitative data on damage evolution. It is based on tension and torsion tests run to fracture or interrupted and followed by SEM observations, but also on direct monitoring of damage during torsion tests carried out in a SEM. For such a loading, surface observations are the most pertinent, contrary to high triaxiality loadings, for which damage initiates in the volume and requires techniques like X-ray microtomography or laminography for its analysis. The latter technique has been used for 2024-T351 aluminum alloy, but the results will be reported in a separate paper.

1. Materials

1.1. Material #1: aluminum 2024-T351 (square bar stock, nearly isotropic)

The first batch of specimens is extracted from a square bar of 2024-T351 aluminum alloy. The bar dimensions in the longitudinal (L), width (W) and thickness (T) directions are 120mm, 100mm and 100mm, respectively. The chemical composition as provided by the supplier is given in Tab. III-1.

-	Si	Fe	Cu	Mn	Mg	Cr	Zn	Ti	Other	Al
Min	/	/	3.8	0.3	1.2	/	/	/	/	remain
Max	0.5	0.05	4.9	0.9	1.8	0.1	0.25	0.15	0.15	remain

Tab. III-1 Chemical composition of aluminum 2024-T351 from the square bar, according to McMaster-Carr, in weight %

Metallographic sections extracted from (L-T)-, (L-W) and (T-W)-planes are prepared for quantitative analysis of the microstructure. These sections are polished with SiC paper from grit #500 to grit #4000, then with a 3µm diamond paste, and finally, with an OP-U colloidal suspension (Struers, France) containing 50 nm-wide particles. EBSD analysis of 1.9x2.5*mm* surfaces with a $5\mu m$ step is performed using a Scanning Electron microscope (Quanta, Model FEI 600) equipped with the HKL Channel software. The material features only weak crystallographic texture for the observed areas (about 1000 grains). However, the results

reveal a morphological anisotropy of the polycrystalline microstructure in the L-T and L-W-planes. The grain dimensions measured by the linear intercept method vary between 80µm and 130µm in the L-direction, between 60µm and 100µm in the T-direction, and between 50µm and 70µm in the W-direction.

SEM observations with chemical composition analysis reveal two categories of particles:

1) *Coarse intermetallic particles*, rich in Al, Cu, Fe, Mn and Si, located in the vicinity of grain boundaries (Fig. III-1a). The measured surface fraction is 0.74%, their average major axis length is $8.9\mu m$ and their average aspect ratio is 2.3. Their mean spacing along the thickness direction is $150\mu m$ (approximately two grains).

2) *Fine intragranular dispersoids*, rich in Al, Cu, Fe, Mn, Si and Mg. The surface fraction of intragranular dispersoids is 3.4%, their average major axis length is 171*nm* and their average aspect ratio is 1.9.

Metallographic observations reported do not reveal any large-scale heterogeneity or anisotropy in the distribution of second-phase particles.

Near some coarse intermetallic particles, equi-axed voids can initially be found (Fig. III-1a). Their average area is about $5\mu m^2$ and their surface fraction is about 0.008%. This material will be referred to as alu-1 in the sequel.

1.2. Material #2: aluminum 2024-T351 (round bar stock, strongly anisotropic)

A second batch of aluminum 2024-T351 specimens is extracted from a 40*mm* diameter forged bar. Different from Material #1, Material #2 exhibits a crystallographic texture with a large fraction of (111) directions parallel to the bar axis. Furthermore, the morphological anisotropy is more pronounced with severely elongated grains: up to $900\mu m$ along the axis of the bar, and only $20\mu m$ in width. As for Material #1, coarse intermetallic particles are found in the vicinity of grain boundaries (Fig. III-1b). These elongated particles are aligned along bands along the forging direction, with a mean spacing of $136\mu m$ (approximately seven grains) along the thickness direction. Their mean width is of $5.4\mu m$. This material will be referred to as alu-2 in the sequel.

1.3. Material #3: 36NiCrMo16 steel (round bar stock, nearly isotropic)

The material was delivered in the form of a 30*mm* diameter bar in an annealed state. Its chemical composition as provided by the supplier is given in Tab. III-2. The material structure consists of a ferritic matrix which contains a very low fraction (about 0.04%) of about manganese sulfides, elongated along the bar axis, about 7µm long in average (Fig. III-1c). It also contains 6% of carbides (Fig. III-1d). The mean major and minor axes of these carbides are 192*nm* and 92.2*nm*, respectively, and their mean distance along the tangential direction is 467*nm*. The mean size-to-spacing ratio is 0.6. No initial porosity is detected in this material.

The grain morphologies and orientations were characterized on a (r-θ) and a (r-z) section with EBSD analysis. The material features grains with strongly irregular shapes and laths of tempered martensite within some grains. The average grain size is about 2.3μm in the radial direction, 2.1μm in the tangential direction, and 2.5μm in the longitudinal direction. The material is weakly textured. This material will be referred to as steel in the sequel.

C	Mn	Si	S	P	Cr	Ni	Mo	Cu	Al	Fe
0.37	0.41	0.25	0.016	0.011	1.72	3.74	0.28	0.25	0.03	Remain

Tab. III-2 Chemical composition of 36NiCrMo16 steel (weight %)

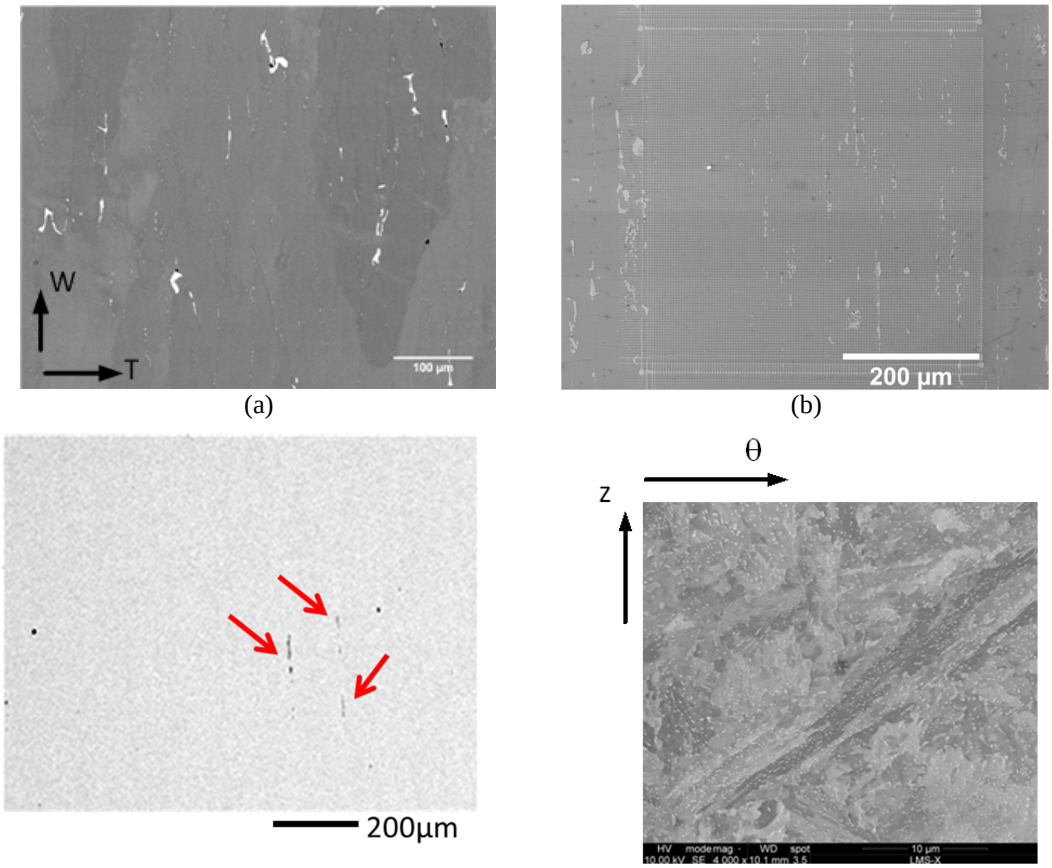

(a) (b) (c) (d)

Fig. III-1 Initial microstructures; (a) alu-1 (b) alu-2 (c) manganese sulfides in the steel (d) carbides in the steel.

2. Experimental procedures

2.1. 2024-T351 aluminum alloys (alu-1 and alu-2)

2.1.1. Combined tension and torsion notched tubular specimens (alu-1)

The test procedure used on alu-1 was described in detail in Chapter I and is only briefly summarized here. Circumferentially notched tubular specimens for tension and torsion tests were extracted with the Z axis parallel to the L direction of the bar (Fig. III-2a). The inner diameter is 20mm, the thickness of the shoulder area is 2mm, while it is reduced to 1mm in the 2mm-high gage section. As strain localization is very sensitive to machining defects, a maximum roughness of 0.1µm was required on both the internal and external surface of the gage section. As explained in Chapter I, the specimen geometry was designed so as to minimize the stress and strain gradients within the gage section, at least prior to necking.

Tests were performed using a servo-hydraulic axial/torsion/internal pressure machine (Tema Concept). Only the axial and torsion actuators were used. They cover a range of +/- 100kN and +/- 600N.m. A biaxial loading angle β is defined as:

$$\beta = \frac{\sigma}{\tau} \tag{4.1}$$

where σ (resp. τ) is the nominal axial (resp. shear) stress component. According to Papasidero et al [101], the stress triaxiality η and Lode angle parameter $\bar{\theta}$ can be expressed as a function of β:

$$\eta = \frac{1}{\sqrt{3}} \frac{\tan\beta}{\sqrt{\tan^2\beta + 4}} \tag{4.2}$$

$$\bar{\theta} = 1 - \frac{2}{\pi} a\cos\left(\frac{6\sqrt{3}\tan\beta}{\left(\tan^2\beta + 4\right)^{3/2}} \right) \tag{4.3}$$

Tests were run either to fracture or interrupted at various stages for two values of β featuring a large proportion of torsion: β=0° ($\eta = 0$ and $\bar{\theta} = 0$) and 55°($\eta = 1/\sqrt{3}$ and $\bar{\theta} = 1$). Note that β=0° corresponds to a stress state of pure shear, while β=55° corresponds to uniaxial tension. Rotation was applied with a speed of 0.019°/s. For β=0°, a zero axial force was imposed, while for other values of β, a procedure was used to apply an increment of axial displacement ensuring the proportionality between the force and the torque. Thus, stress state variations were very limited during the test.

Stereo-correlation of digital images (3DIC) was used to measure displacement and strain fields on the surface of the gage section. Two digital cameras (Pike F505B with 90mm Tamron macro lenses) were used to periodically capture 2452x2054 pixels image pairs of the notched area on which a black and white paint speckle had been applied. The 3D displacement field was then obtained by stereo-correlation of these digital images (3DIC), using VIC3D (Correlated Solutions). The lenses were at a distance of 80cm from the specimen, which provided enough depth of field to allow a proper measurement of out of plane motions due to torsion.

2.1.2. In-situ torsion test (alu-2)

An in-situ torsion test were made in a SEM on a cylindrical specimen with a diameter of 5mm and a gage length of 14mm cut in the forged bar of alu-2, along the longitudinal direction (Fig. III-2b). After careful mechanical and electrolytic polishing, eight 500*500μm^2

wide patches of square shaped gold microgrids with a 4µm pitch were laid on the surface from the upper to the lower end of the gage length, using micro-electro-lithography. The specimen was then mounted on a tension-torsion loading frame with a capacity of 50Nm and 10kN working in a Philips XL 40 SEM and progressively loaded in torsion at a rotation rate of 0.25°/s, while keeping zero axial stress. The test was stopped at intervals to monitor strain and damage evolution at the surface and capture high resolution (4096*4096 pixels) images.

2.2. 36NiCrMo16 steel

Tests were run only to fracture using the notched tubular specimens and in the same conditions as for alu-1, for four loadings cases: β=0° ($\eta = 0$ and $\bar{\theta} = 0$), 21.9° ($\eta = 0.11$ and $\bar{\theta} = 0.33$), 34.1° ($\eta = 0.19$ and $\bar{\theta} = 0.54$) and 55° ($\eta = 1/3$ and $\bar{\theta} = 1$).

An in-situ torsion test was also realized on this material, in the SEM on the same cylindrical specimen geometry as for alu-2 and in the same conditions.

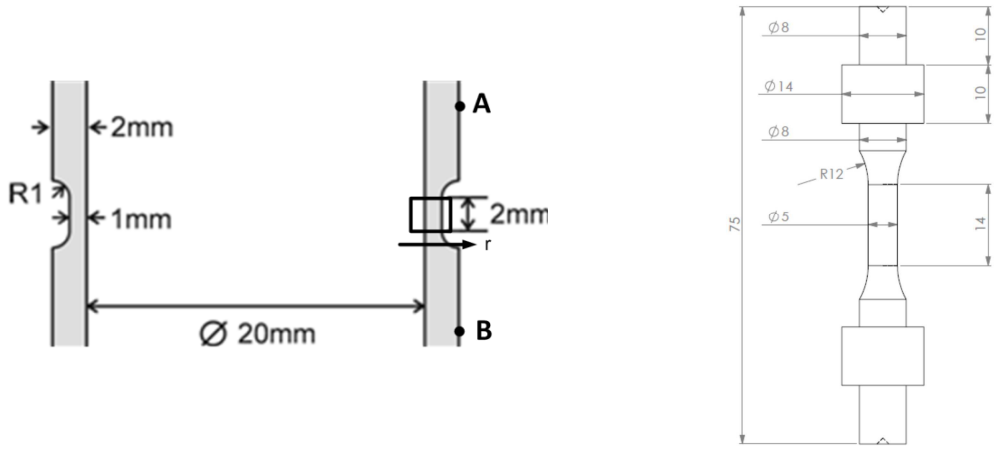

(a) (b)

Fig. III-2 (a) Sketch of the combined tension-torsion notched tubular specimen (b) Sketch of the cylindrical specimen for the in-situ torsion test in the SEM.

2.3.Post-processing

2.3.1. Combined tension and torsion tests on notched tubular specimens

For stereo-correlation measurements of displacement fields on the surface of the gage section, correlation was made using VIC3D (Correlated Solutions) with a gauge length of 1 pixel (24µm), and the subset used to determine the position of each pixel of the gage section was a 21x21 pixel-wide square. As VIC3D automatically smoothes the results along five

neighboring points to post-process the strain fields, which are given in a cartesian frame, an independent post-processing tool was developed using Matlab to compute the axial and shear strain fields at each pixel, without filtering, and in a cylindrical frame.

The fracture surfaces of broken specimens were observed using Scanning Electron Microscopy (SEM). After the interrupted tests, longitudinal (rz) and circumferential (θz) sections were extracted at various locations of the tubes, prepared according to the method described in section 2, and observed with SEM (Quanta FEI 600 or Philips XL 40). For alu-1, some sections were analyzed with a digital optical microscope (Keyence VHX1000) using polarized light, after an anodization with Barker's reagent (200mL of distilled water + 10mL of fluoroboric acid at 24V during 1min30), which revealed grain boundaries with an excellent contrast. Besides, for alu-1, image processing of SEM pictures of a few θz sections was undertaken using Matlab Image Processing Toolbox, in order to compare the damage features with the voids initially present in LT and LW planes.

2.3.2. In-situ torsion experiments

Accurate strain field measurements by digital image correlation were not attempted, since the out-of-plane displacements associated with the large rotation of one of the specimens head would induce an excessive error. However, the distortion of the microgrids was used only for an approximate evaluation of the engineering shear strain γ and axial strain ε_{zz}. In that case, ε_{zz} and γ were obtained from the elongation ΔL_{grid} and rotation α_{grid} of four different 500*500µm^2 grids by: $\varepsilon_{zz} = \frac{\Delta L_{grid}}{L_O}$ and $\gamma = \frac{dx}{L_o} = \tan(\alpha_{grid})$ (Fig. III-3).

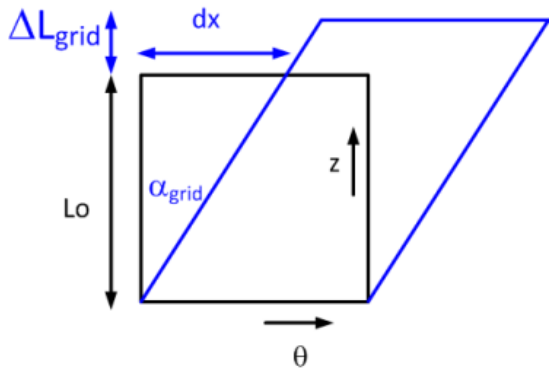

Fig. III-3 Illustration of the grids kinematics

3. Experimental observations

3.1. Aluminum 2024-T351 (materials #1 and #2)

3.1.1. Macroscopic overview

Fig. III-4a and Fig. III-4b show the evolution of the torque (resp. force) as a function of the relative rotation (resp. displacement) measured between two points A and B located on the shoulder section at a distance of 16mm from each other (Fig. III-2a), for combined tension and torsion tests on alu-1 notched tubular specimens. The solid dots on the curves show the points where the tests were interrupted. For β=0° (resp. 55°), two tests to fracture, β0-f_1 and β0-f_2 (resp. β55-f_1 and β55-f_2), along with two interrupted tests β0-i_1 and β0-i_2 (resp. β55-i_1 and β55-i_2) were performed. The corresponding values of final equivalent plastic strains $\bar{\varepsilon}_f$ averaged over a 2mm high optical gauge are summed up in Tab. III-3. Concerning the in-situ torsion test on aluminium-2 cylindrical specimens, Fig. III-4c shows the torque versus the engineering shear strain γ.

Test	β0-f_1	β0-f_2	β0-i_1	β0-i2	β55-f_1	β55-f_2	β55-i_1	β55-i2
$\bar{\varepsilon}_f$	0.25	0.22	0.18	0.20	0.22	0.17	0.14	0.17
Fraction of max $\bar{\varepsilon}_f$			72%	80%			64%	77%

Tab. III-3 Summary of the values of equivalent plastic strain reached during tests on notched tubes of alu-1

Fracture is defined as the moment when the loads dropped suddenly to zero while the specimen got separated in two parts. Concerning combined tension and torsion test on alu-1 notched tubular specimens, a slight dispersion of the rotation at the onset of fracture is observed, as indicated by horizontal error bars (Fig. III-4a and Fig. III-4b).

Fig. III-4d shows the evolution of the engineering axial strain ε_{zz} versus the engineering shear strain γ during torsion tests. The squares and crosses stand for the measurements performed on four grids during the in-situ torsion test on alu-2 cylindrical specimen. The data from the various grids were consistent and could reasonably be fitted by a linear equation which indicates that the axial elongation represents 9.4% of the shear strain in alu-2. The light blue dots stand for the torsion test on the alu-1 notched tubular specimen, for which ε_{zz} and γ were deduced from the measurements of ΔZ and $\Delta\theta$ of an optical gauge of initial height

$L_o = 2mm$ on the surface of the gage section, as: $\varepsilon_{zz} = \frac{\Delta Z}{L_O}$ and $\gamma = \frac{R_{ext}\Delta\theta}{L_O}$, where R_{ext} is the initial external radius of the gage section. For the notched specimen, the final elongation of the gage section was about 20 microns which corresponds to an average engineering axial strain of about 1%. Therefore, an axial elongation occurred during the torsion tests. This effect was more important during the in-situ torsion test on the textured material (alu-2) from the forged bar. This shear-induced elongation corresponds to the so-called "Swift effect" [102] observed in many metallic tubes or cylinders submitted to free-end torsion. Wu et al [103] found that in aluminum tubes, depending on the gage length and thickness and on the initial texture, the elongation for a shear strain of 110% varied between 1 and 4%. This effect was attributed either to texture development (Toth et al [104]) or, more recently, to tension-compression asymmetry resulting from mechanical twinning, deviation from Schmid's law or residual stresses, depending on the metal (Cazacu et al [105]).

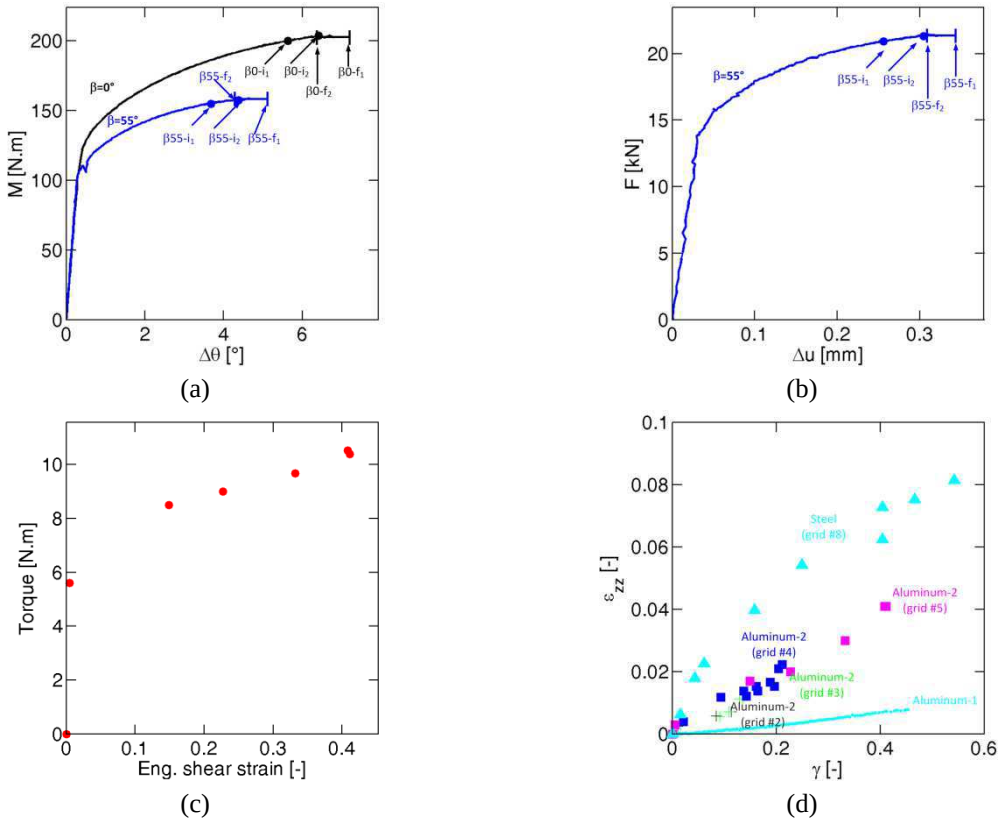

Fig. III-4 Load VS displacement curves (a) M VS Δθ and (b) F VS Δu for interrupted tests and tests to fracture on alu-1 notched tubular specimens (c) M VS -γ for the in-situ torsion test on alu-2 (d) Evolution of the engineering axial strain versus the engineering shear strain measured during in-situ tests.

Pictures of broken specimens are shown in Fig. III-5. For the test on notched tubular specimens corresponding to β=0° (alu-1), fracture occurred near one end of the gage section

(Fig. III-5a), but still at a location where stress triaxiality is zero. Fig. III-5c shows the aspect of the in-situ alu-2 cylindrical specimen broken in torsion in the SEM.

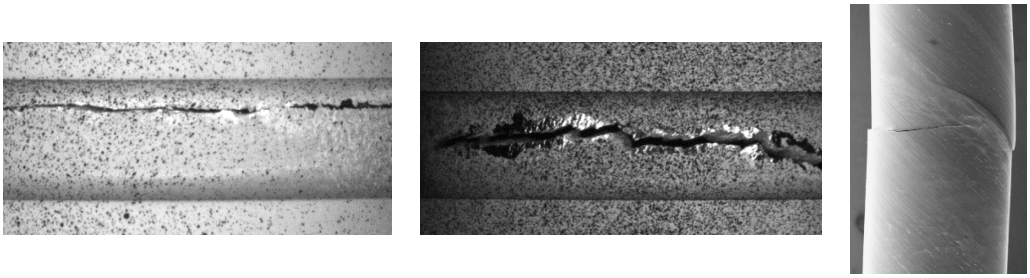

(a) (b) (c)

Fig. III-5 Circumferential view of broken notched specimens for notched specimens of alu-1 (a) β=0° and (b) 55°. (c) View of broken specimens from the torsion in-situ tests on alu-2.

3.1.2. Strain localization

3.1.2.1. Suface strain measurements

The engineering shear and axial strain fields computed from 3DIC with a step size of one pixel (24µm) just before unloading are plotted on Fig. III-6a and Fig. III-6b for β0-i_2, and Fig. III-6c and Fig. III-6d for β55-i_2 tests on alu-1 notched tubular specimens. One can note already that the local strain field is much higher than the values averaged over the gage section, presented in Tab. III-3. Indeed, the step size is lower than the grain size and the strain field is quite heterogeneous. Locally high axial strain values (up to 40% in torsion) can be reached, in bands that seem perpendicular to the tube axis.

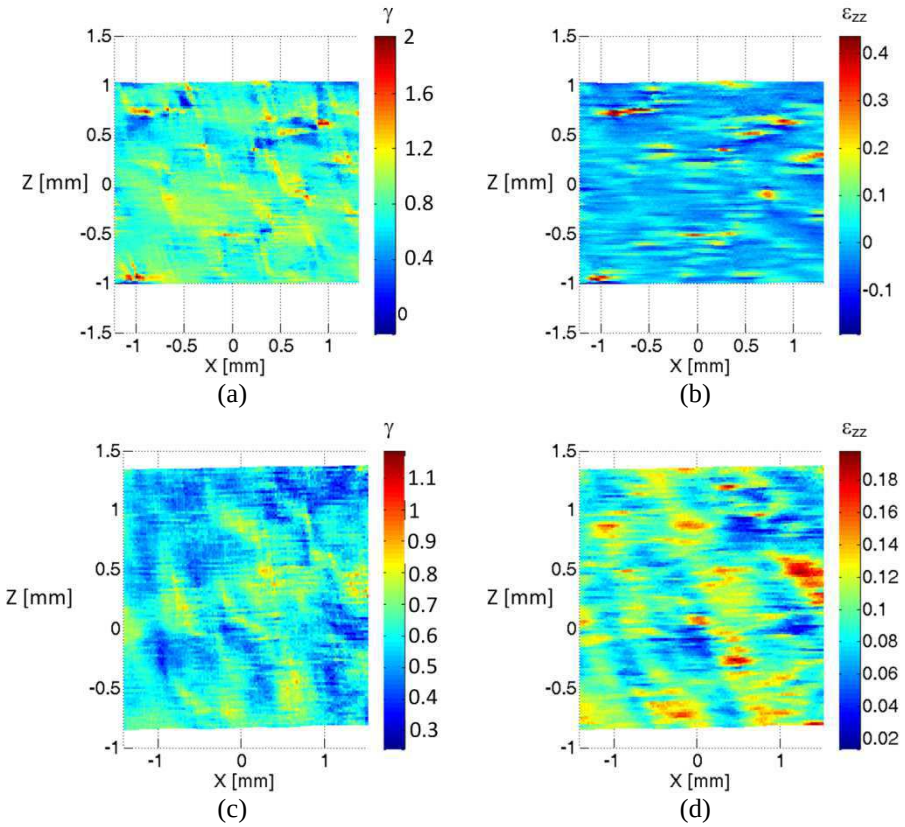

Fig. III-6 Interrupted tests on alu-1. Surface strain fields measured by 3DIC just before fracture for β0-i_2 (a) engineering shear and (b) axial strain, and for β55-i_2 (c) engineering shear and (d) axial strain

3.1.2.2. At the grain scale

Observation of θz sections from interrupted tests on alu-1 notched specimens, polished and etched with Barker's reagent showed that, due to torsion, the major axes of the more or less elliptical grains rotated with respect to their initial average orientation, aligned with the tube axis. An automatic procedure was developed using Matlab to post-process EBSD maps captured with a step size of 5μm over 2.5mm x 1.9 mm wide areas on θz sections (which corresponds approximately to 400 grains). The rotation α of the major axis of each grain was computed with respect to its original orientation, assumed to coincide with the Z-axis, in accordance with observations made in the deformation-free shoulder section. Following the same approach as that used to evaluate the shear strain from micro-grids rotation in the in-situ torsion tests, the shear strain was thus approximated as:

$$\gamma = \tan(\alpha) \tag{4.4}$$

Fig. III-7a and Fig. III-7b show the shear strain map γ obtained from post-processing of the EBSD map according to Eq. 4.4. Each dot represents the position of the center of a grain. It can be seen that the strain distribution is quite heterogeneous. Besides, strain levels are much

higher at this scale than those measured at the macro-scale by averaging over the gage section length. They can reach values up to 2 locally, and even in average, they are higher. Indeed, on the histogram on Fig. III-7c, for β0-i_1 one can see that most grains present a shear strain around 0.55 for a macroscopic shear strain of 0.34. On the histogram on Fig. III-7d, for β55-i_1, most grains present a shear strain around 0.3 for a macroscopic shear strain of 0.23. For β0-i_1, about 52% of the grains have a shear strain between 0.5 and 2. The number of neighboring grains which exhibit a shear strain between 1 and 2, can reach 3 for pure shear, while, for β55-i_1, only a few isolated grains have very high shear strains.

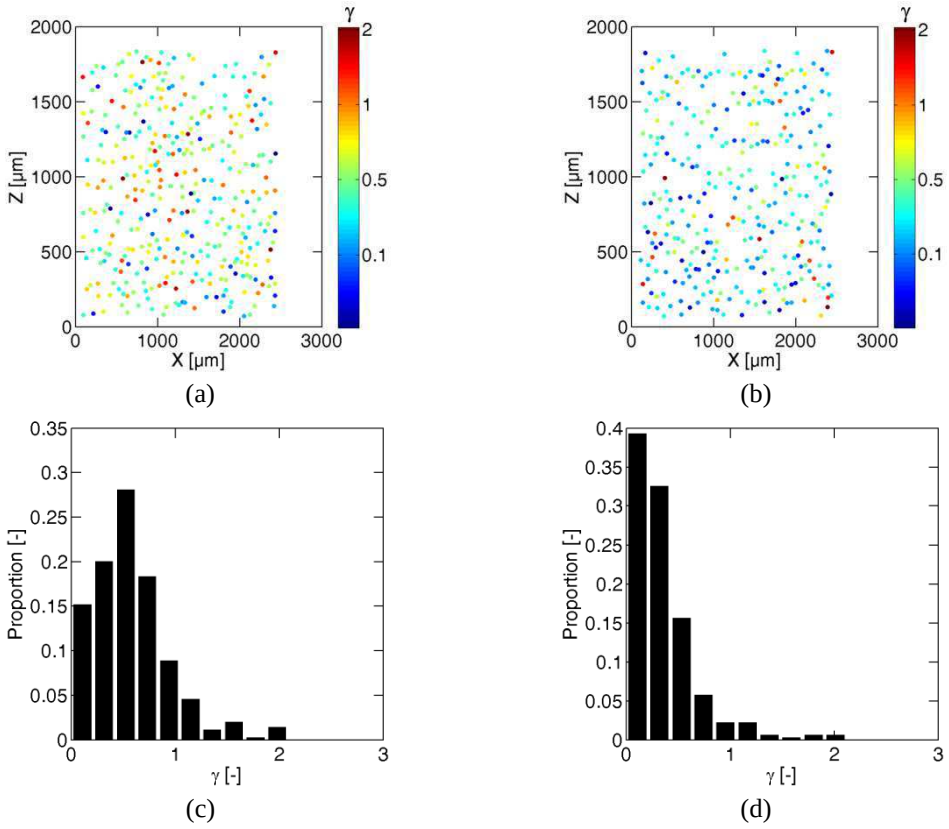

Fig. III-7 Alu-1. Engineering shear strain obtained from grain morphological rotation for (a) β0-$i_1$and (b) β55-i_1. Local shear distribution for (c) β0-$i_1$and (d) β55-i_1.

3.1.2.3. Subgrain localization

Concerning the interrupted tests on alu-1, misorientation bands within a few grains, especially for β=0° (Fig. III-8d) were clearly revealed by optical miscrosopy after etching with Barker's reagent. Those "kink bands" suggest strain localization at a scale even finer than the grain scale that TEM observations would reveal. Most of the kink bands were located in grains very close to the main crack.

During the in situ torsion test on alu-2, strain localization could be observed at small scales. The strain was concentrated near the grain boundaries and even at the grain boundaries themselves, suspected to undergo sliding (Fig. III-8a). Strain differentials between neighboring grains gave rise to surface undulations. In some cases, stress concentrations due to broken particles lying along the grain boundaries might have triggered this intergranular strain localization, but this is not always the case. At late stages, very intense slip bands, triggered by stress concentrations at broken intergranular particles crossed the grain (Fig. III-8b) but stopped at the next grain boundary. It is striking to see such coarse slip bands in a heavily deformed grain, while the neighboring grain still exhibits a relatively homogeneous deformation $\gamma \approx 0.59$. In some cases, one-grain-large (that is: less than 20μm-long) shear microcracks appeared without any visible broken particle in the surrounding, at least on the surface (Fig. III-8c). Ahead of such microcracks, shear strains of the order of 110% were measured, based on local grid rotation.

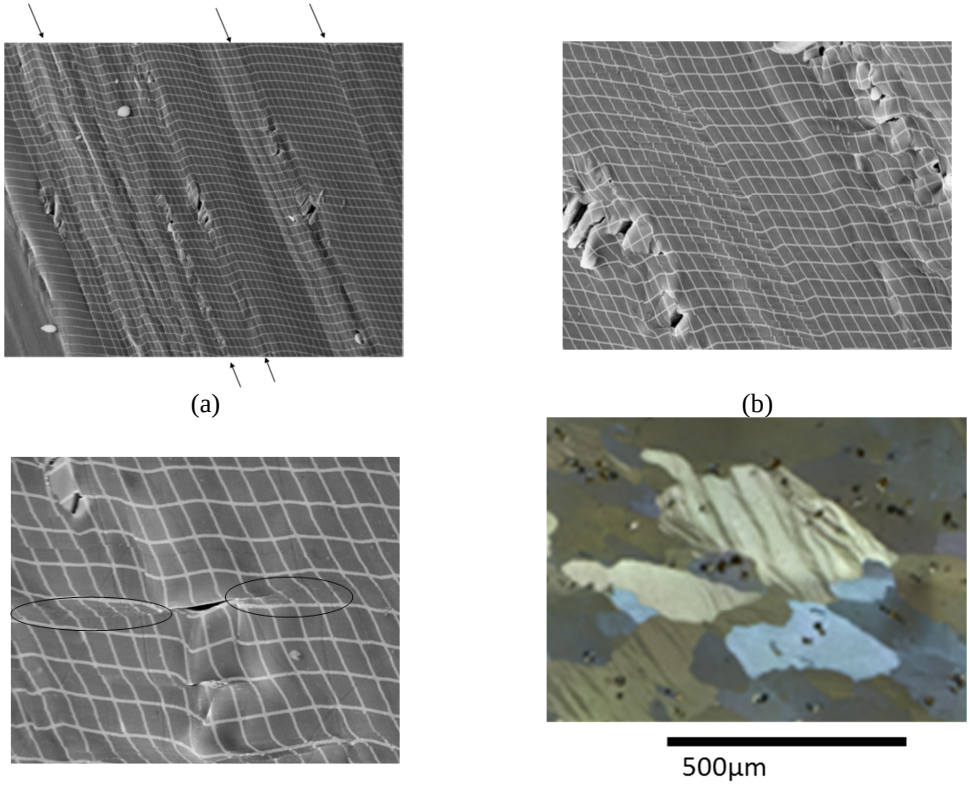

Fig. III-8 Alu-2 (a) Strain localization at grain boundaries and fragments of broken or debonded particles (appearing white on the picture) expulsed from superficial cavities (b) Strain localization into coarse slip bands inside a grain, while the neighbouring grain still exhibits a relatively homogeneous deformation g ≈ 0,59 (c) Extreme shear localization and transgranular micro-cracking at the final stage of in situ torsion (mean shear ≈ 0.46). Shear strain higher than 110% in the circled area (d) Alu-1: kink bands within grains for $\beta 0\text{-}i_1$.

3.1.3. Damage

3.1.3.1. Fracture surfaces

SEM observations of fracture surfaces reveal small, elongated dimples (Fig. III-9a) and abrasive marks (Fig. III-9b). These abrasive marks are mainly present near the outer radius where failure probably initiated and where the relative sliding displacements of the crack face were thus the highest, as it propagated into the depth. In most parts of the fracture surface corresponding to $\beta=0°$, the abrasive marks are more or less aligned with the tangential direction and up to 200µm long. As the proportion of tension increases, they become less extended, but are still observable up to $\beta=55°$.

Two populations or dimples can be observed for $\beta=55°$: large ones (about 15μm-wide) inside which multiple cracked coarse intermetallic particles can be found and small ones (about 1.3μm) containing intact dispersoids. As the stress triaxiality decreases, the dimples decrease in size (down to 1µm in torsion) and become more and more elongated along a preferred orientation, especially those located near the external radius

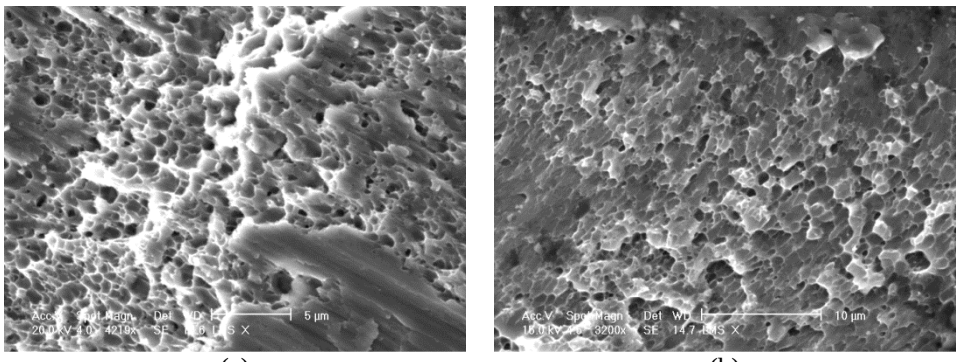

(a) (b)

Fig. III-9 SEM views of fracture surfaces of alu-1 broken notched specimens (a) $\beta=0°$ (b) $\beta=55°$.

3.1.3.2. Micrographs from interrupted tension-torsion tests on notched tubular specimens (alu-1)

SEM observations of polished sections after the interrupted tests on alu-1 notched specimens showed that the greatest amount of damage was located near grain boundaries. Indeed, for both values of β , damage occurred by debonding and multiple fracture of coarse intermetallic particles (Fig. III-10a), and was diffuse within the whole gage section.

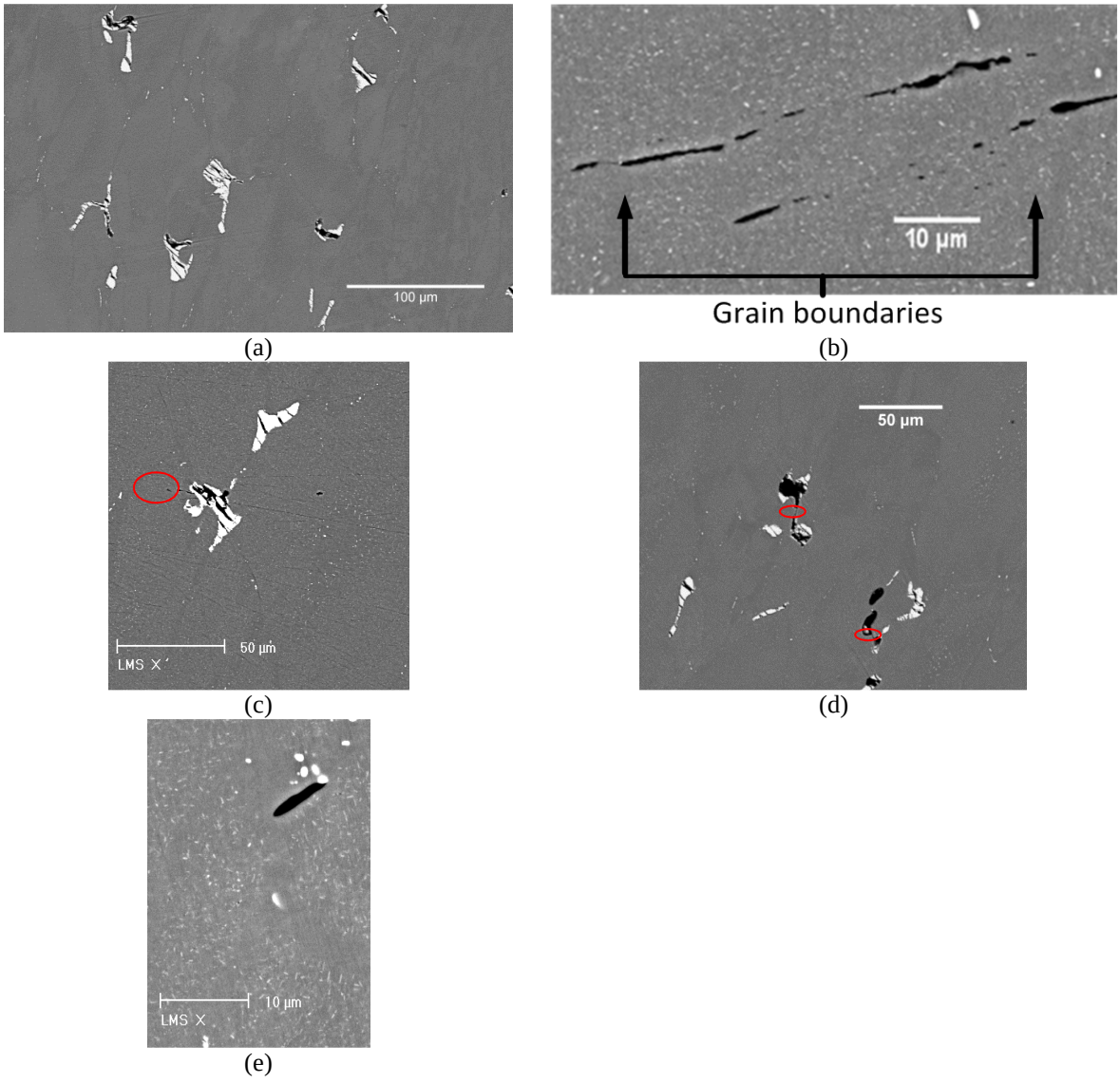

Fig. III-10 SEM micrographs from interrupted tests on notched tubular specimens of alu-1 (a) β55-i_1 (b) β0-i_2 near the crack (c) β0-i_2 very coarse particle fracture near a grain boundary and nucleation of micro-voids (d) β0-i_2 a very elongated void (e) β55-i_2 void sheeting coalescence

The evolution of the number of voids per unit surface is plotted versus the macroscopic equivalent plastic strain for the tests on notched tubes in Fig. III-11b. Crosses are used for voids resulting from debonding, while plain dots also include voids issued from particle cracking. From this graph, it can be inferred that void nucleation mainly comes from particles breaking, while half of the debonding pores results from initial porosity. The void density rate increases throughout the tests. More coarse particles break for β=55° than for β=0°, but the density of voids issued from debonding is the same in both cases. Besides, according to Fig. III-11c, for both values of β, the debonding void area fraction does not increase much with the

plastic strain. However, for β=55°, the debonding void area fraction is higher than for β=0° by a factor 3 and higher than that in the initial state by a factor 6. The total area fraction for β=55° is higher than for β=0° by a factor 5 and higher than the initial state by a factor 32.

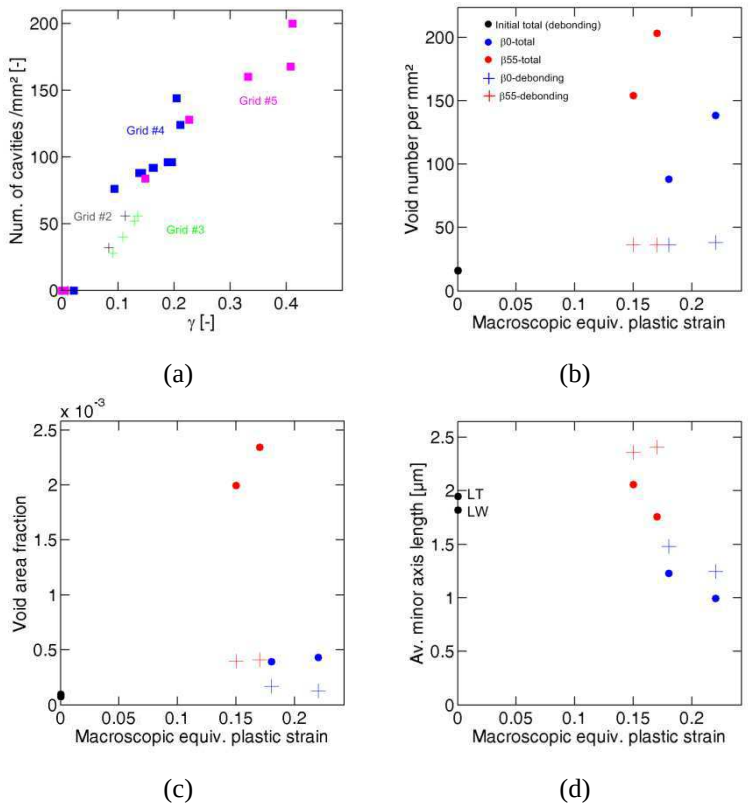

Fig. III-11 (a) Evolution of the void number per surface unit for the in-situ torsion test on alu-2. For the interrupted tests on notched specimens on alu-1, evolution of the (b) number per surface unit (c) area fraction (d) average minor axis.

The area distributions (Fig. III-12) suggest some void growth for β=55°. For β=0°, one may find a few voids with a larger area than the largest void areas in the initial states. However, such voids represent only a small fraction of the voids (between 0.05% and 1.8%) and Fig. III-12c suggests a slight decrease of the average void area. It seems that those very few voids come mostly from debonding occurring in the vicinity of grain boundaries.

On the other hand, void distortion appears quite often in the analyzed sections. Pre-existing voids -mainly issued from particles debonding- are mostly equiaxial, with a mean aspect ratio of 1.4 (Fig. III-13a). After straining nearly to fracture, the voids are elongated, with an average aspect ratio of 3.5 for β=0° and 3.8 for β=55°. A comparison of Fig. III-13b and Fig. III-13d or Fig. III-13c and Fig. III-13e shows that the voids issued from the fracture of intermetallic particles achieve higher aspect ratios than those issued from particles

debonding, because they result from the distortion of a crack with an initially high aspect ratio. It was observed that the major axis of most voids tends to form a specific angle with the Z-axis of the specimen: 45° for β=0° and 55° for β=55°, which, corresponds to the direction of large particles breakage, in both cases, perpendicular to the maximum principal stress. Quantitative analysis based on tests interrupted at a relatively late stage showed a definite increase in aspect ratio of pre-existing initially circular voids under pure shear.

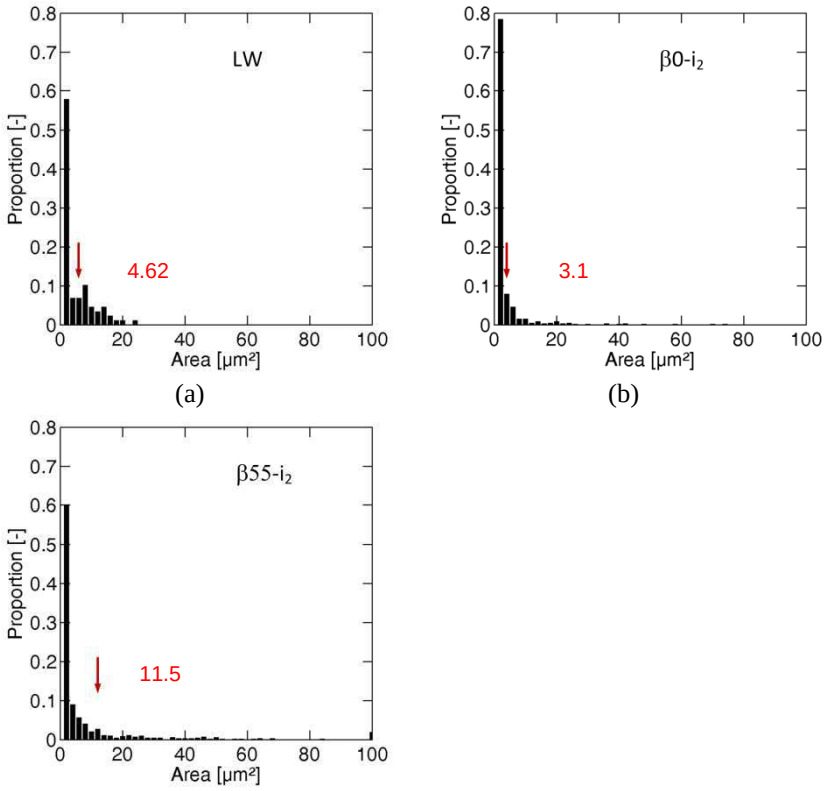

Fig. III-12 Voids area distribution in the alu-1 for (a) initial state (b) β0-i_2 (c) β55-i2. The red arrows represent the average value.

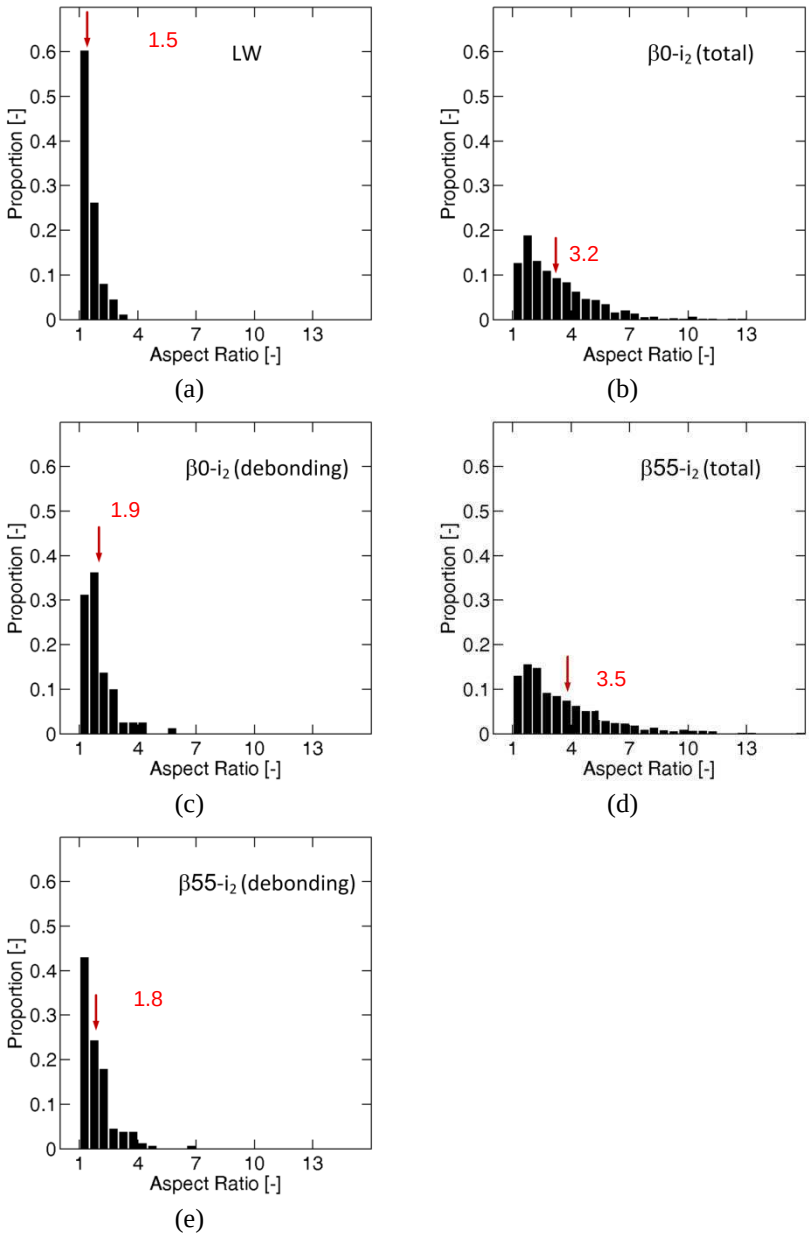

Fig. III-13 Aspect ratio distribution alu-1 for (a) initial state (b) and (c) β0-i_2 (d) and (e) β55-i_2

Very little interaction between voids could be observed until the latest stages, such as β0-i_2 (80% of the fracture strain). However, the notable presence of a population of small dimples on fracture surfaces suggests that micro-void sheeting occurs very shortly before final fracture, through a population of secondary voids born near transgranular dispersoids. This is consistent with observations on a θz section of β0-f_2 showing that a little further away from the crack, debonding of smaller intermetallic particles along grain boundaries occurs, as well as nucleation of intragranular microvoids (Fig. III-10b and Fig. III-10c). As for β55-i_2,

although internal necking may be observed between a couple of neighboring grown cavities, most coalescence events occurs by void sheeting (Fig. III-10d).

3.1.3.3. In-situ torsion test (alu-2)

Fig. III-11a shows the evolution of the number of voids per unit surface plotted versus the mean shear strain of the grid for the in-situ torsion test on alu-2. Above $\gamma \approx 0.025$, cavity nucleation occurs regularly -mainly due to fracture of particles- though with a tendency towards saturation above $\gamma \approx 0.34$.

Real-time monitoring of the cavities –mainly issued from particles fracture like for alu-1 – during in situ torsion (Fig. III-14) suggests in fact a non-monotonic evolution of voids aspect ratios. During the largest part of the test, void evolution is limited to a rotation plus "crack" opening without any lateral extension, until the latest stage and the initiation of coarse slip bands in the grain. As a result, the void aspect ratios -initially quasi infinite due to their crack-like shape- actually decrease as the voids become more circular. , the expulsion of broken and/or debonded particles from surface cavities was frequently observed (Fig. III-8a).

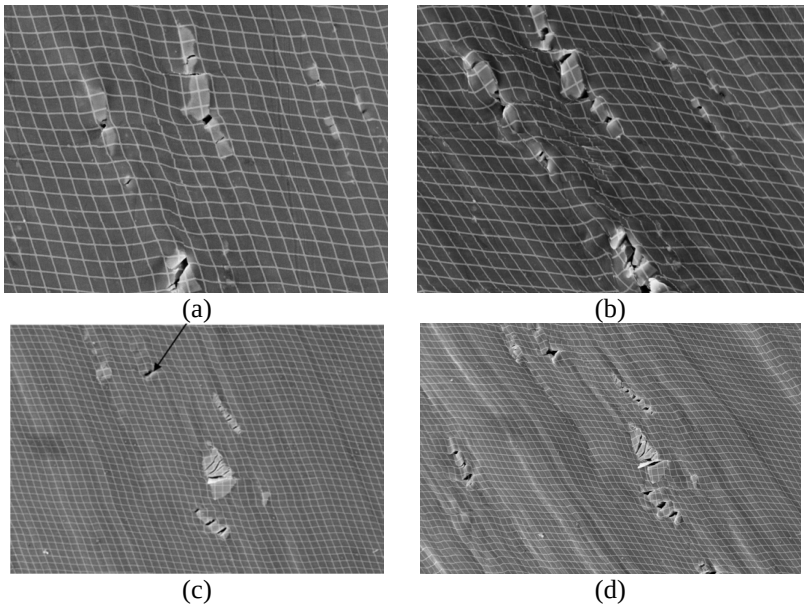

Fig. III-14 Damage evolution during the in-situ torsion test on alu-2 (a) to (c) Rotation and opening of a crack-shaped void which tends to become circular (d) Elongation of the same void, which rotates and become oriented in the direction of the shear plane.

3.2.Experimental observations for steel (material #3)

3.2.1. Macroscopic Overview

Fig. III-15a and Fig. III-15b show the axial and rotational loads VS displacement curves between the same points A and B for steel. The corresponding values of final equivalent plastic strains $\bar{\varepsilon}_f$ averaged over a 2mm high optical gauge are summed up in Tab. III-4. For β=55°, loads reach a maximum value and then decrease smoothly, as the gage section experiences necking. Then, a sudden load drop occurs while the specimen gets separated in two parts. For the other tests, no smooth decrease is observed, and the load just drops abruptly as a macroscopic crack appears. As previously, this event (the dramatic load drop) is considered as the instant of the onset of fracture.

Test	β=0°	β=21.9°	β=34.1°	β=55°
$\bar{\varepsilon}_f$	0.82	0.62	0.65	0.7

Tab. III-4 Summary of the values of equivalent plastic strain reached during tests on steel notched tubes

Fig. III-15c shows the torque versus engineering shear strain deduced from grids deformation for the in-situ torsion test on the steel. Fig. III-4d shows the evolution of the engineering axial strain versus the engineering shear strain, and the triangles stand for the in-situ torsion test on steel. Here again, an axial elongation is observed, since the axial strain reached 7.5%, and represented 13.5% of the shear strain. Pictures of broken specimens are shown in Fig. III-16.

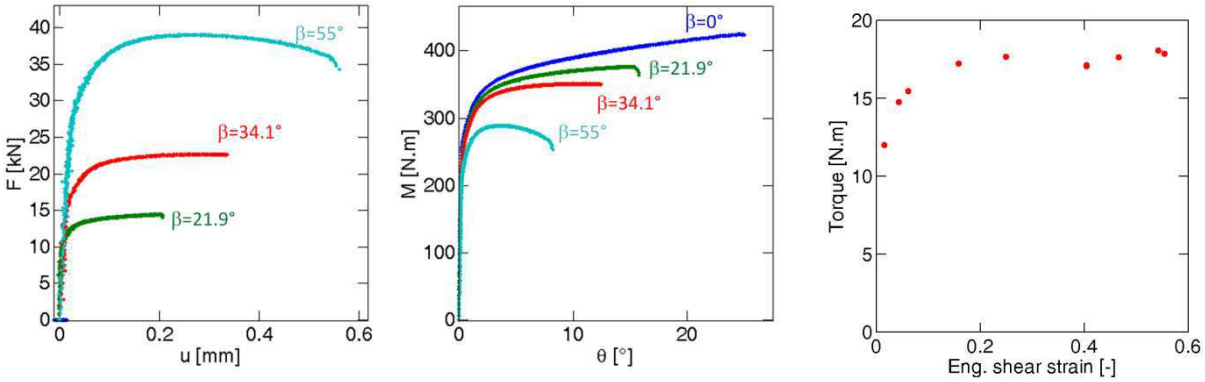

(a) (b) (c)

Fig. III-15 Load VS displacement curves (a) F VS Δu and (b) M VS Δθ for interrupted tests and tests to fracture on steel notched tubular specimens; (c) M VS ~~Δθ~~ γ for the in-situ torsion test on steel.

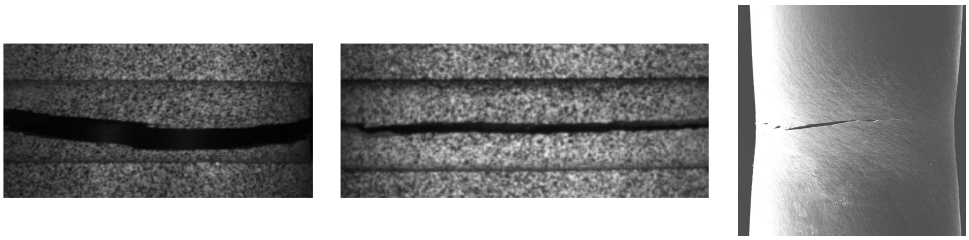

(a) (b) (c)

Fig. III-16 Circumferential view of broken notched specimens for steel notched specimens: (a) β=0° and (c) 55°; (c) View of broken specimens from the torsion in-situ tests on the steel cylindrical l specimen.

3.2.2. Strain localization

For this material as well, strain fields were computed with a step size of 1 pixel (24µm) on the surface of the gage section of tension-torsion notched tubular specimens. These fields are presented in Chapter I. Contrary to the aluminum alloy, the strain field at this scale seemed homogeneous, as the grains size was much lower than the resolution of DIC measurements.

Observation of θz sections from steel notched tubular specimens broken in torsion-dominated loadings showed a rotation of the elongated manganese sulfides, initially oriented along the Z-axis. Following the same approach as that used to evaluate the shear strain γ from micro-grids rotation, their rotation α was used to estimate the local engineering shear strain using Eq. 4.4. The variation of γ with the distance to the fracture plane for tests involving some torsion is plotted on Fig. III-17a. The local strain levels are much higher than those measured at the macro-scale by averaging over the gage section, because of a blatant strain localization near the fracture plane for tests with high proportions of torsion (β=0° and 21.9°), which decreases as the proportion of tension increases. This localization band, in which engineering shear strain can locally reach values up to 4, is very narrow (about 40µm).

EBSD analyses performed on broken specimens for β=0°, and 21.9° in the (rθ) plane, after slightly polishing the fracture surface, suggest that deformation occurs with a reorientation of grains which tends to form clusters sharing the same orientation, this making shear bands development more and more likely to occur, especially in torsion. Misorientation profiles with respect to the Z-axis were computed along tangential lines. These profiles are shown on Fig. III-17b, where only points with 0°-misorientation with their neighbours are represented. Five similar profiles were plotted for each test, and confirm this observation.

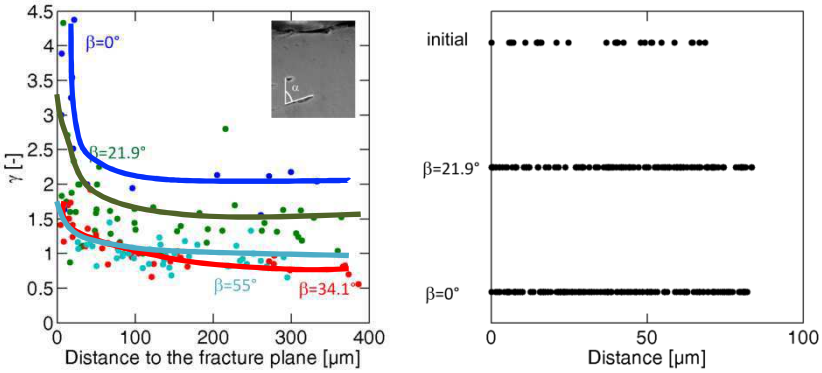

(a) (b)

Fig. III-17 Steel : (a) Evolution of the engineering shear strain versus the distance to the fracture plane (b) Grain misorientation profiles for initial configuration.

3.2.3. Damage

3.2.3.1. Fracture surfaces

SEM observation of fracture surfaces reveal common features with fracture surfaces of alu-1 fracture tests: small, elongated dimples (Fig. III-18b and Fig. III-18c) and abrasive marks (Fig. III-18a) can be seen. The change in dimples size with the stress triaxiality is quite limited: for all tests, their major axis is about 1.5-2µm, their aspect ratio is about 1.7 and carbides can be seen inside. However a dramatic change in orientation is observed: as the stress triaxiality decreases, their major axis becomes more and more oriented in the tangential direction.

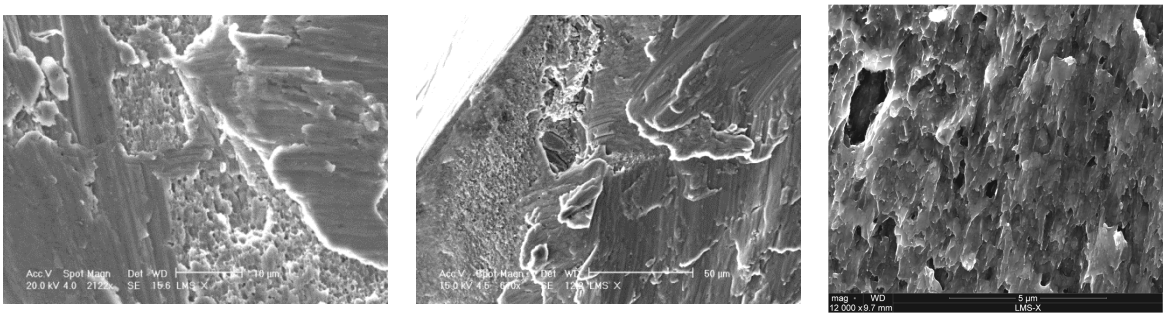

(a) (b) (c)

Fig. III-18 SEM views of fracture surfaces of broken notched specimens (a) steel β=0° (b) steel β=55° (c) alu-1 β=0° (d) alu-1 β=55° (e) steel in-situ torsion test.

3.2.3.2. Micrographs from fracture tests on tension-torsion notched tubular specimens

SEM observations of polished sections of broken steel notched tubular specimens revealed multiple fractures of manganese sulfides near the fracture surface. However, the size and spacing of the dimples observed on the fracture surfaces are not consistent with those of manganese sulfides. These particles are probably not responsible for the final failure, rather

due to late carbides decohesion. On these sections, no void interaction could be seen away from the fracture plane.

3.2.3.3. In-situ torsion test

During the in situ torsion tests on steel, no cavity nucleation was observed on the specimen surface, within the spatial resolution of the SEM, even after strain localization. Instead, beyond $\gamma \approx 0.22$, many one-grain-size long micro-cracks appeared, nearly normal to the axis (Fig. III-19), but most of it did not grow into the neighboring grains.

Only those located in the localization band around the fracture plane finally grew and merged (Fig. III-20). Even though they did not play a significant role in fracture, it is interesting to illustrate the evolution of a group of small, initially circular, pre-existing cavities, probably due to pitting during electro-polishing (Fig. III-21). They hardly grow, but rather elongate along the tensile principal direction and shrink along the compressive one, without a total collapse.

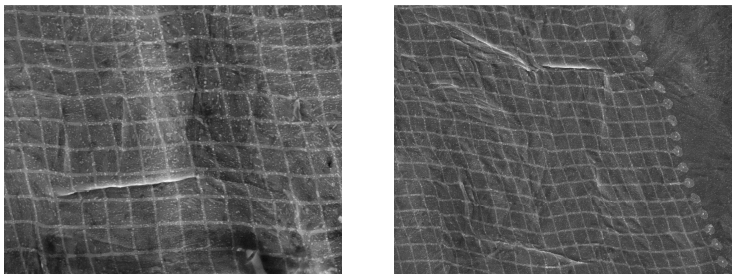

(a) (b)

Fig. III-19 Micro-cracks on the surface of the in-situ torsion specimen for the steel (a) γ=0.22 (b) γ=0.4

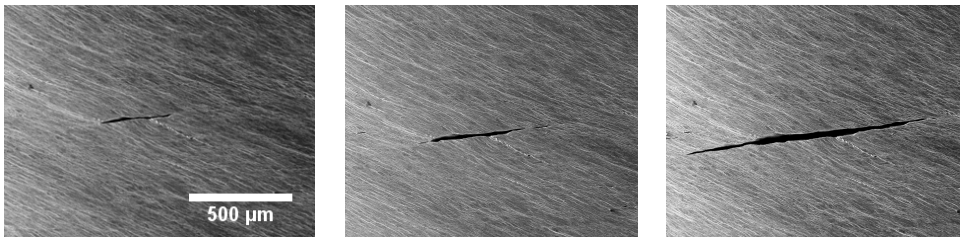

(a) (b) (c)

Fig. III-20 Evolution of a microcrack near the end of the in-situ torsion test on the steel (a) γ=0.5 (b) γ=0.54 (c) γ=0.55

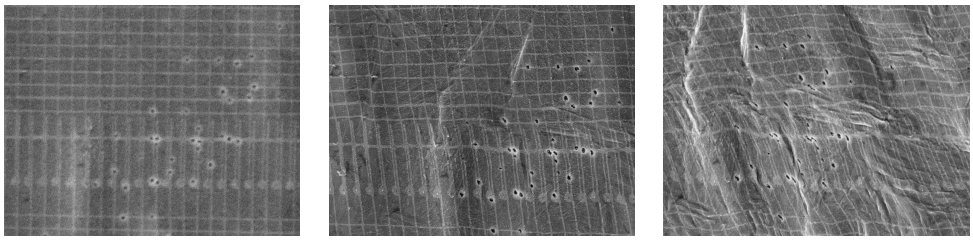

(a) (b) (c)

Fig. III-21 Evolution of preexisting cavities during the in-situ torsion test on the steel (a) γ=0 (b) γ=0.105 (c) γ=0.372

4. Discussion

4.1.Void evolution

Microscopic observations performed on both aluminum alloys suggest that damage occurred mainly by multiple fractures of coarse intermetallic particles, and evolved mainly by void rotation and distortion, combined with some void growth in cases where triaxiality was non-zero or, for zero triaxiality, due to the Swift effect. The real-time observations performed during the in-situ torsion do not support the predictions of some micromechanical models concerning the evolution of a void under shear-dominant loading. In particular, the complete closure of voids under pure shear loading as predicted by Nielsen [47] was not observed here. Even if, in average, the aspect ratio increased, no total collapse of cavity was observed, and some cavities were proven to grow, probably due to the presence of intermetallic particles trapped inside, which might prevent their total collapse at high shear strain, as suggested by the fact that the mean void minor axis length remained close to that of the particles it originated from. The observations were actually more consistent with the conclusions of McVeigh et al. [97], who took into account the presence of particles in a void.

The Swift effect may also play an important part in preventing the complete collapse of the cavities, and even, in helping some cavities to grow. Indeed, the macro-scale axial elongation due to the Swift effect is weak, but the local axial strain field is quite heterogeneous, as shown in Fig. III-6. Therefore, locally high axial strains might contribute to the growth of some cavities at nominally zero stress triaxiality.

The initial geometry considered in unit cell models -Barsoum and Faleskog [34], Mc Veigh et al. [97]- corresponds to a prolate or oblate ellipsoidal cavity with one of its major axes aligned with the shearing direction. Such a configuration is not quite representative of

the kind of damage observed here in the aluminum alloys, since second phase particle cracking -in a principal plane- rather leads to arrays of microcracks inclined by 45° with respect to the shearing direction. We remind that these microcracks first opened without lateral extension. Thus, the aspect ratio first decreases as the cracks become “more circular”. The increase in aspect ratio predicted by several models for shear-dominated loadings seems to occur at a rather late stage of straining (like those reported for interrupted tests on alu-1) and come only in a second stage.

Besides, the boundary conditions used to simulate damage evolutions in shear in unit cell models often include a zero axial displacement condition – Fleck and Hutchinson [106], Anderson et al. [95], Rahman et al. [98] – that would not capture the significant Swift effect observed here, likely to postpone the collapse of the cavities. In some other models – Barsoum and Faleskog [34], Mc Veigh et al. [97], Nielsen et al. [47]– an axial displacement is prescribed so as to keep the ratio of tensile to shear stress constant, but the authors do not generally plot the resulting axial strain, which cannot thus be compared to our measurements. Indeed, the unit cell model allows a control of the stress state that cannot be achieved as easily in experiments. It would be interesting to couple in-situ experiments performed with micro-scale full-field measurements with a unit cell model, by prescribing the measured transformation gradient as boundary conditions.

4.2.Void interaction.

The formation of secondary voids and final coalescence are very fast in the aluminum alloy, and could only be seen after $\beta 0\text{-}i_2$ test, interrupted quite late, while the specimen was already partially broken, or during the last stages of the in situ torsion test. In their numerical study, McVeigh et al. [97] as well as Rahman et al [98] observed that shear localization and the large amount of voids rotation before fracture strongly depend on the size-to-spacing ratio of the second-phase particles. In our experiments, most coarse particles in the aluminum were far from each other (size-to- spacing ratio of 0.16 for alu-1, and 0.04 for alu-2) which explains why there were so few interactions between the voids until very late stages. Some interaction was however observed for $\beta=55°$ because the axial load favored void growth and distortion, this allowing it to get closer and coalesce. For $\beta=0°$, this was more difficult, and only cavities issued from particles belonging to the same cluster were likely to coalesce, as shear loading made their ends come closer together.

5. Conclusion

In the present study, ductile damage of 2024-T351 aluminum alloy and 36NiCrMo16 steel has been investigated, for low values of stress triaxialities through combined tension and torsion tests, run to fracture or interrupted and followed by SEM observations, but also through direct monitoring of damage during torsion tests carried out in a SEM.

In 2024-T351, damage mostly initiates by fracture of the coarsest intermetallic particles along a principal plane, in the vicinity of grain boundaries and is first quite homogeneously spread over the gage section. In pure shear, this generates arrays of micro-cracks inclined by 45° - a configuration that is not described by most the existing unit cell models. The cavities aspect ratio first decreases as the cracks open and turn into voids that finally rotate and elongate in one direction while shrinking in the other –this leading in a second stage to an increase in their aspect ratio. Void growth is observed for $\eta=1/3$ but not $\eta=0$, at least in average. In the latter case, the voids do not collapse, which is attributed both to the presence of intermetallic particles inside it and to the significant axial elongation - Swift effect- associated to the large measured shear strain. The heterogeneity of the axial strain field might explain why, contrary to the average evolution, some voids do achieve a large size in nominally pure shear loading. When a certain level of strain is reached (about 0.22), intragranular micro voids nucleate from dispersoids as well as coarse slip bands, allowing neighboring coarser voids formed earlier at the grain boundaries to join and form a crack which propagates through the grains. Strain localization was illustrated at different scales: at a meso-scale, based on the heterogeneity of surface strain fields from DIC or on the larger grain rotations measured within a distance of 300µm from the fracture surface and at a sub-grain scale, based on early flow localization near grain boundaries and at a later stage, into kink bands or coarse transgranular slip bands.

In 36NiCrMo16 steel, no cavity nucleation was observed during the in situ torsion test within the spatial resolution of the SEM, but, at a rather early stage, several one-grain-size long micro-cracks, nearly normal to the axis, which did not grow. However, small dimples - nucleated from carbides- were present on the fracture surfaces for all triaxiality ratios. This parameter did not influence much the dimples size, but mainly their shape, extremely elongated in pure shear. Evaluations of the local shear strain based on the rotation of manganese sulfides revealed intense strain localization into a very narrow band (40µm wide

in torsion, with shear strains as high as 2.5). This trend towards localized deformation decreased as the stress triaxiality ratio increased;

The crystallographic texture and its evolutions seem to play an important role in the fracture process. In both materials, damage remains confined inside isolated grains and unable to develop into neighboring grains, even when it is already a microcrack for quite a long time. EBSD measurements on steel have shown that as the stress triaxiality decreases, texture evolutions become more and more important and form larger and larger clusters of grains sharing the same orientation, this making shear bands development easier and easier.

It might thus be pertinent to consider the polycrystalline structure of metals and to put emphasis on localization phenomena and micro-cracks development, instead of focusing on continua with initially circular voids, when modeling ductile fracture at low traixiality ratio.

IV. Crack initiation and propagation in aluminum 2024-T351 via in-situ synchrotron radiation computed laminography

---

The last chapter presents the first results of an on-going work in collaboration with the Centre des Matériaux (Evry, France), and Lukas Helfen from the European Synchrotron Research Facility (ESRF) in Grenoble (France). The damage mechanisms in the aluminum 2024-T351 used in Chapter II are analyzed at the micro-scale, at a higher range of stress triaxialities (approximately from 0.4 to 1.4). This investigation benefits from the X-ray laminography technique available at ESRF, and from the know-how of Thilo Morgeneyer et al. for in-situ laminography tests.

The damage mechanisms underlying crack initiation and propagation in a CT specimen are assessed in-situ via synchrotron radiation computed laminography. A quantitative analysis of the evolution of the porosity provides some parameters that could be used in a future work in micromechanical models: a critical void volume fraction for crack propagation, and the evolution of the porosity distribution. The main result of this part is that even at this range of stress triaxiality, the predominant coalescence mechanism in aluminum 2024-T351 is shear localization.

The contribution of Frank Nguyen, engineer at Centre des Matériaux, to the image processing of the volumes obtained at ESRF is gratefully acknowledged.

The advances in X-ray synchrotron computed tomography and laminography make it possible to characterize more and more precisely ductile fracture and improve its modeling. Indeed, while conventional two-dimensional metallographic techniques require destruction of a specimen to partially access the mechanisms and are not proof against artefacts, this fully three-dimensional technique allows better qualitative and quantitative understanding of damage. Thus, a more accurate investigation of initiation and growth of damage on metallic materials provided quantitative microstructural information, such as the voids distribution, size, shape or density, that could bring a better insight in the damage process [107,108,13], discuss the validity of ductile damage mechanics models calibrations [100], allow a direct experimental calibration of micromechanical models parameters [109,110,22], validate or extend void growth models [111]. In particular, X-ray tomography and laminography has brought another perspective to the understanding of the different growth and coalescence mechanisms in the flat to slant ductile fracture transition during crack propagation [36].

In the present work, an in-situ tensile test is performed on a CT specimen using X-ray laminography. A qualitative analysis allows to highlight the main damage mechanisms, which gives useful information to guide the choice of a model. On the quantitative front, focus is brought on the characterization of void volume fraction evolution. Besides an average critical porosity which could be ultimately used in micromechanical models, a damage field is computed, which allows to link the crack propagation to microstructural heterogeneities.

1. Material

The material investigated is the same 2024-T351 aluminum alloy as the one used in the study presented in Chapter II. Its description is briefly reminded in this section.The bar dimensions in L, T and W directions are 900mm, 100mm and 100mm, respectively.

As mentioned in Chapter III, the material features two categories of particles: intergranular coarse intermetallic particles, rich in Al, Cu, Fe, Mn and Si, and transgranular dispersoids, rich in Al, Cu, Fe, Mn, Si and Mg. The volume fraction of coarse intermetallic particles assessed via image analysis of a volume of $0.5mm^3$ is about 1.1%; their average dimensions are 9µm x 4µm. Initial porosity can be found near these particles. The initial void volume fraction assessed via image analysis of a volume of $0.5mm^3$ is about 0.04% and their average dimensions. One can note that the initial coarse particles and, more significantly, the

void fractions estimated by volume analysis are higher than the fractions measured by SEM metallography in Chapter III. A similar observation was made by Taylor and Sherry [100]. However, in their case, the discrepancies between 2D and 3D measurements were less dramatic, as the order of magnitude of the dimensions on which they performed their analyses was quite similar. In our case, the size of the zone examined by laminography is much smaller than the size of the zone analyzed by SEM metallography.

2. Experimental procedure

2.1. In-situ test

A test was performed on a 1mm thick CT specimen. The specimen geometry is illustrated in Fig. IV-1a. It consisted of a 15mm long pre-crack created by electron-discharge machining. The specimen was loaded in the L direction by means of a two-screw device to control the crack opening displacement (COD) which was monitored by digital image correlation, measuring the relative displacement of δ5 markers, i.e. two markers located at 2.5mm on both sides of the crack and 4mm away from the initial notch (Fig. IV-1b). The crack propagation direction corresponds to the W direction. The in-situ test was performed using the synchrotron X-ray source on line ID19 of the European Synchrotron Radiation Facility (ESRF) in Grenoble. A monochromatic beam of 19keV energy and an axis inclination angle of about 25° (θ=65°) were used (Fig. IV-1c and d). The distance between the specimen and the detector is 50mm. Volumes of 1.4x1.4x1.4mm^3 were reconstructed using 2500 angularly equidistant projections with an exposure time of 100ms per projection, and a resolution of 0.7µm per voxel.

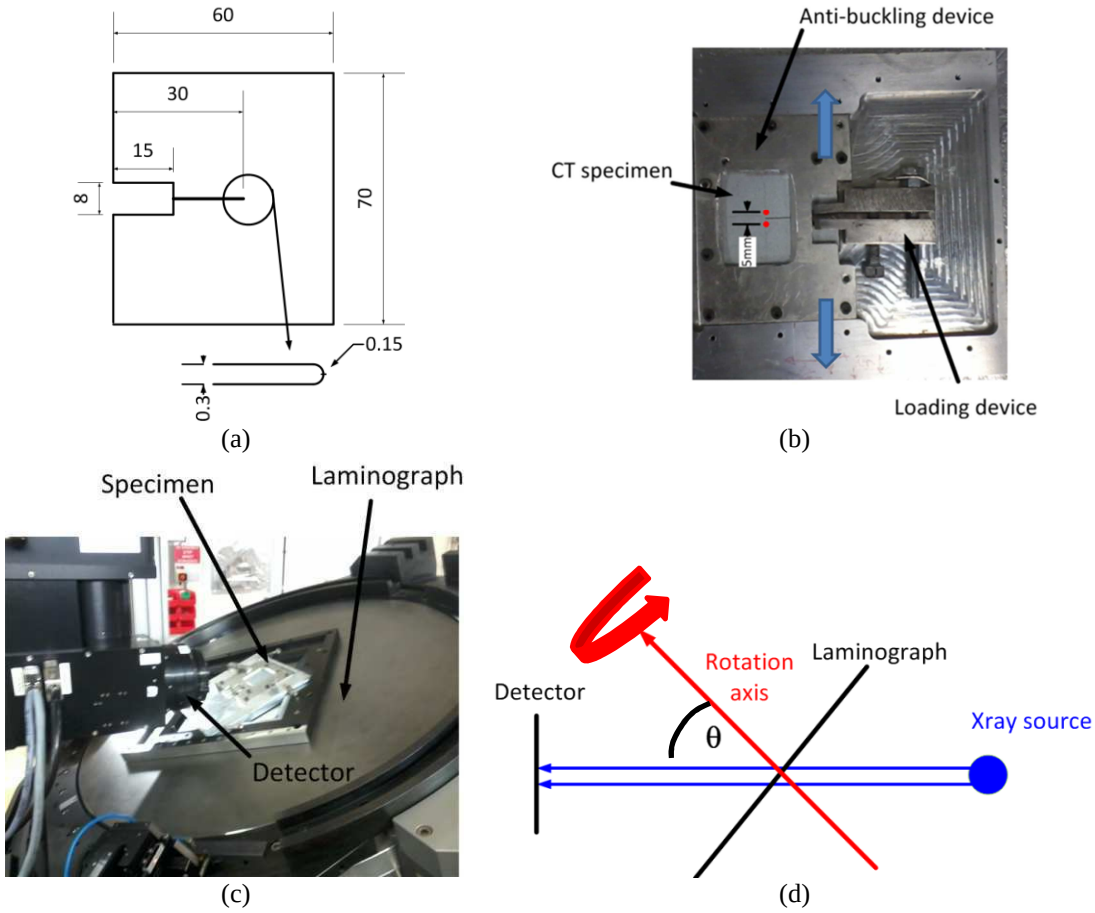

Fig. IV-1 (a) CT-specimen geometry (all dimensions in mm) (b) Loading device and CT specimen (δ5 markers in red) (c) CT specimen mounted on ID19 beamline (d) schematics of the ID19 beamline

2.2.Experiment post-processing

Damage was qualitatively analyzed by extracting sections in the LW and LT planes from reconstructed volumes, at different specimen locations and for different COD values. LW sections were extracted at mid-thickness, while LT sections were extracted at different locations ahead of the initial notch. This analysis was coupled with SEM observations of the fracture surfaces.

A quantitative post-processing was also undertaken in order to quantify damage evolution during crack propagation. Sub-volumes of 770 x 1335 x 940µm^3 were segmented using Matlab Image Processing Toolbox to isolate the crack and the voids. The first direction of these sub-volumes corresponds to the thickness direction T (385µm on both side of the mid-thickness slice) and the second dimension corresponds to the crack propagation direction W. A void volume fraction field was computed for all steps using fixed grids of 50 x 50 x 50µm^3 For this purpose, the sub-volumes were divided into 18 layers of 50µm in the L direction, and

each layer was divided into a grid of 50 x 50µm^2. The local void volume fraction was computed for each square in each layer. Assuming that the crack path opens following the location of maximal porosity, the output of this analysis was a map of the maximum void volume fraction over the 18 layers. This post-processing is illustrated in Fig. IV-2. Besides, for each loading step, a crack opening displacement map (COD-map) was computed by adding all pixels within the crack isolated by image processing. Of course, the results of this post-processing is strongly dependent on the discretization of the volume of interest. Here, a size of 50µm is chosen, because it is quite representative of average distance between particles where voids are first nucleated. A fixed grid is used to post-process all the volumes, which probably leads to an underestimation of the void volume fraction.

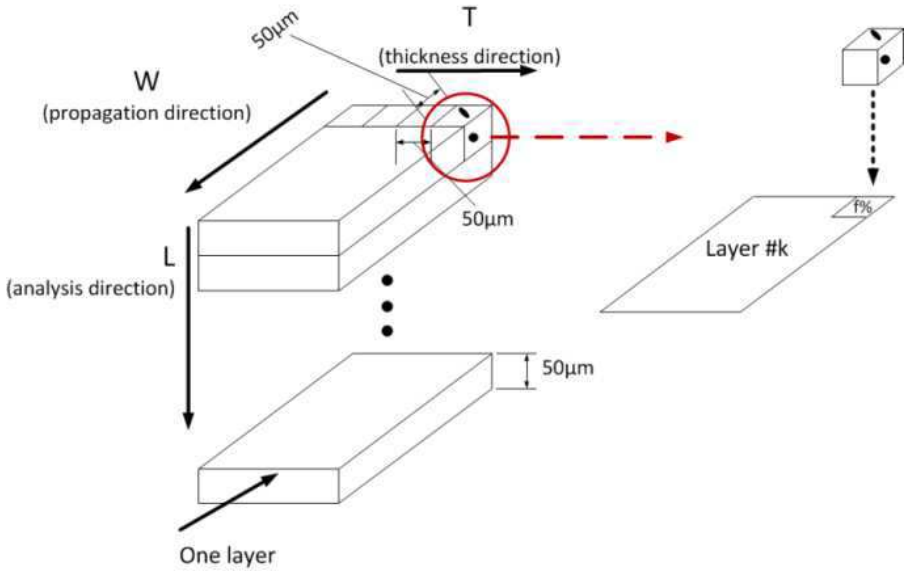

Fig. IV-2 Computation of the void volume fraction field.

3. Results

3.1. Qualitative analysis

2D sections of the specimen at mid-thickness in the LW plane are shown in Fig. IV-3 for different values of δ5. Damage occurred by cracking of coarse intermetallic particles or growing of pre-existing voids. Most particles break perpendicularly to the loading direction. At δ5=7.3µm, at mid-thickness, fracture of a particle located about 15µm away from the notch surface is observed (Fig. IV-3b). The void grows a little and coalesces with the crack at

$\delta 5$=16.8µm (Fig. IV-3c). But then, no crack advance is measured. The crack just opens until $\delta 5$=42.5µm (Fig. IV-3d), when it propagates brutally, coalescing with another void located about 100µm ahead of the initial notch and circled in blue in Fig. IV-3b.

When the crack starts propagating at $\delta 5$=42.5µm, a small zone (no more than 150µm from the initial notch surface) can be seen around mid-thickness where voids coming from broken intermetallic particles grow more than near the free surfaces. This can be seen in Fig. IV-4a and b, which show 2D sections of the specimen in the TW plane, located right at the initial notch tip, and 150µm away from it, as the crack starts propagating. Besides, Fig. IV-5a shows a SEM view of the broken specimen fracture surface. The initial notch tip is located right at the bottom of the picture, and one can see in the first 150µm away from the initial notch, at mid-thickness, circled in red, clusters of broken intermetallic particles. The tunneling effect classically observed in ductile fracture of notched or pre-cracked specimens, which consists in a flat triangular zone in which the crack propagates faster in the mid-section - where the stress triaxiality is higher- than near the free surfaces is hardly observed here. The crack propagates in a slanted way almost immediately. This is probably due to the fact that the notch is not too severe. Indeed, in Bron et al. [8], comparison between the fracture surfaces of notched bars with different notch radii or shape (in U or in V) and Kahn specimens show that as the severity of the notch increases, the tunneling zone is more important. On the contrary, as the severity of the notch decreases, the slant propagation begins earlier. Past the first 150µm away from the initial notch surface, a few evidences of void growth can be found, not necessarily at mid-thickness, but away from the free surfaces, and at locations where intermetallic particles broke.

The predominant coalescence mechanism in this test appears to be void sheeting. Fig. IV-4c shows a 2D section of the specimen in the TW plane, about 510µm ahead of the initial notch, at $\delta 5$=56.9µm. The voids circled in red came from fracture of intermetallic particles and grow while void sheeting occurs between them. These features can also be found on the fracture surface. Fig. IV-5b shows a zoom of the zone circled in red in Fig. IV-5a, right in front of the initial notch. Between 50µm-large zones where broken intermetallic particles can be found lie submicronic dimples, inside some of which dispersoids can be seen (Fig. IV-5d). These kind of dimples are also found near the free surfaces of the fracture surface, as in Fig. IV-5c, which presents a zoom of the zone circled in blue in Fig. IV-5a. In some places, friction marks are present on the fracture surface, meaning that the crack faces slide against each other (Fig. IV-5e). In-situ, little intermediate steps could be captured between a void growth and its

sudden interaction with the crack, and SEM micrographs showed no sign of damage around dispersoids away on either side of the crack, nor at the crack tip, suggesting that this shear localization occurs very brutally, as if the material just unzipped between grown voids coming from fracture of coarse particles. This observation is in accordance with Taylor and Sherry [100], who also analyzed broken CT specimens using X-ray an FIB tomography.

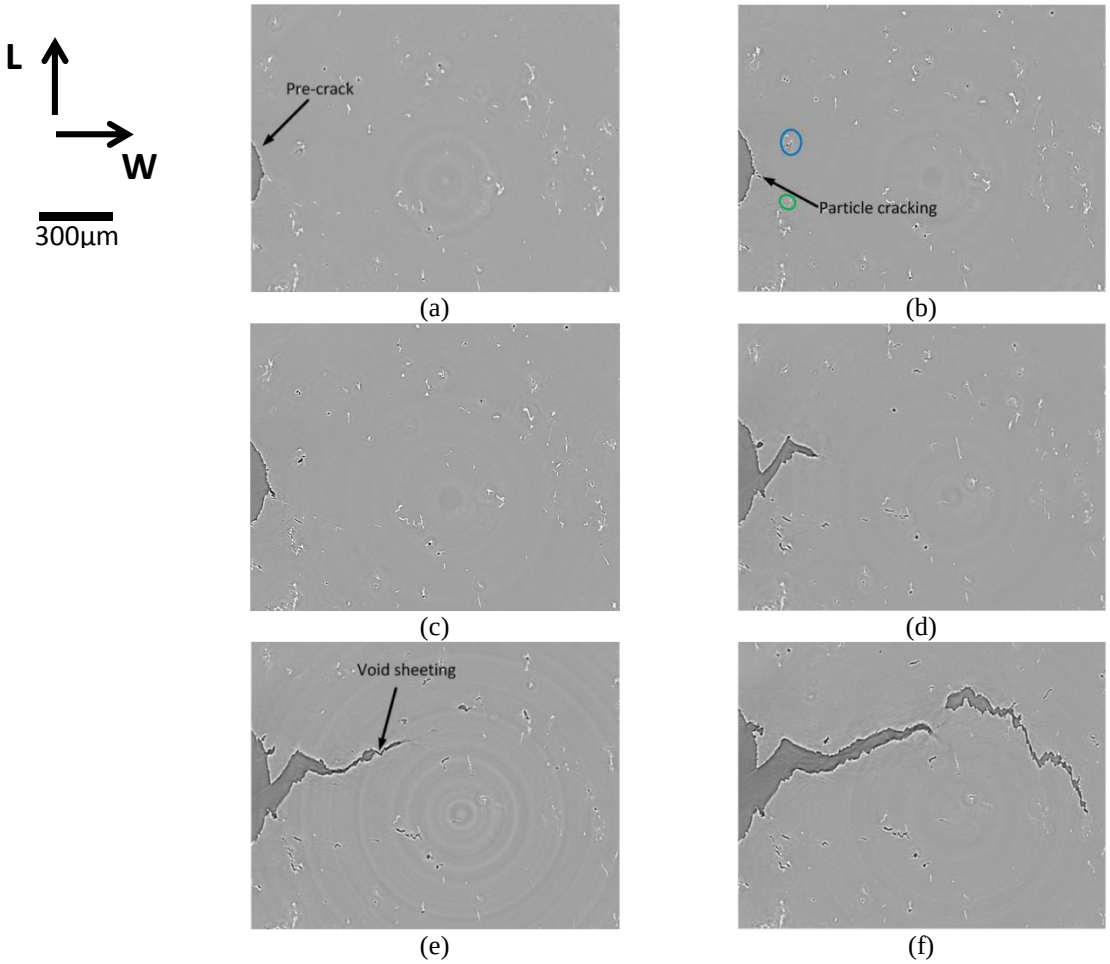

Fig. IV-3 2-D sections in the LW plane at mid-thickness of the specimen for δ5 = (a) 0µm (b) 9.8µm (c) 16.8µm (d) 42.5µm (e) 56.9µm (f) 77.4µm

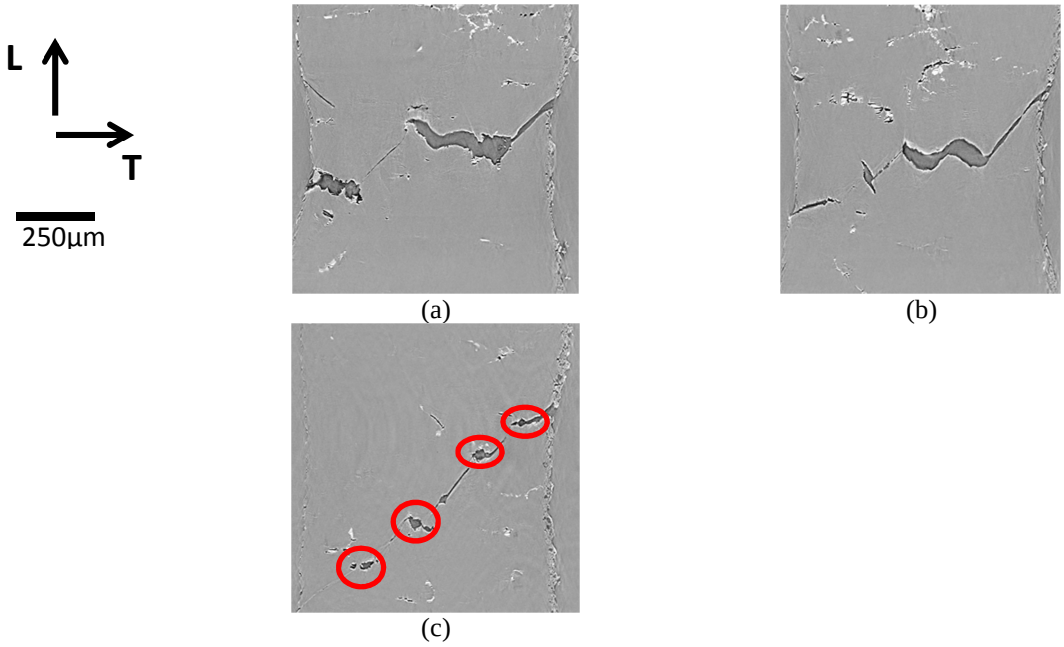

Fig. IV-4 2-D sections in the LT plane in regions located (a) at the initial notch tip (δ5=27.6µm) (b) 150µm ahead of the initial notch tip (δ5=42.5µm) (c) 510µm ahead of the initial notch (δ5=77.4µm)

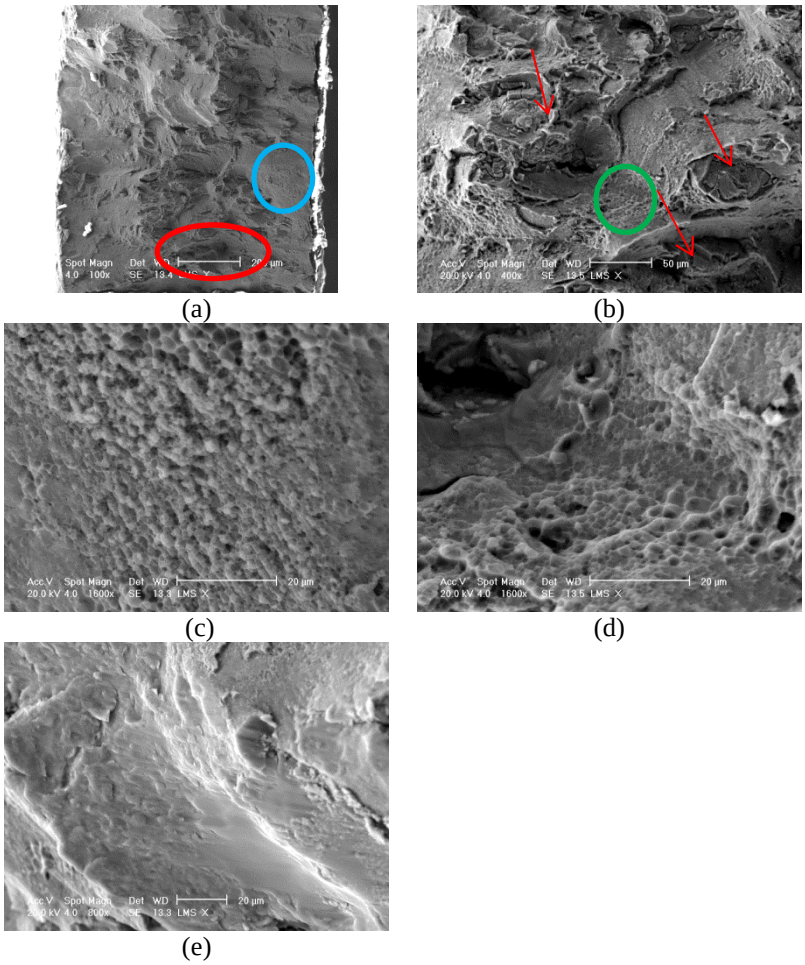

Fig. IV-5 SEM views (a) global view of the fracture surface (b) zoom in the zone circled in red; red arrows point at broken intermetallic particles near grain boundaries (c) zoom in the zone circled in blue (d) zoom in the zone circled in green (e) friction marks

3.2.Quantitative analysis

Fig. IV-6 shows 3D views of thresholded subvolumes where only the crack and cavities appear for four values of δ5. The early slant aspect of the crack appears clearly for δ5= 42.5µm (Fig. IV-6c) and subsequent values of δ5, along with the void growth in front of the crack tip.

The crack path is quite irregular, as can be seen in Fig. IV-3f for instance. Sometimes indeed, the crack seems about to interact with certain voids, but finally follows another path. For example, at δ5=16.8µm (Fig. IV-3c), the crack seems ready to propagate towards the void circled in green (Fig. IV-3b). But then, at δ5=42.5µm (Fig. IV-3d), the crack rather coalesces with the void circled in blue, which came from the cracking of a particle at δ5=9.9µm located about 100µm ahead of the initial notch (Fig. IV-3b). The analysis of the evolution of the volume of these two cavities suggests that the crack ultimately interacted with the void which increase rate was higher (Fig. IV-7).

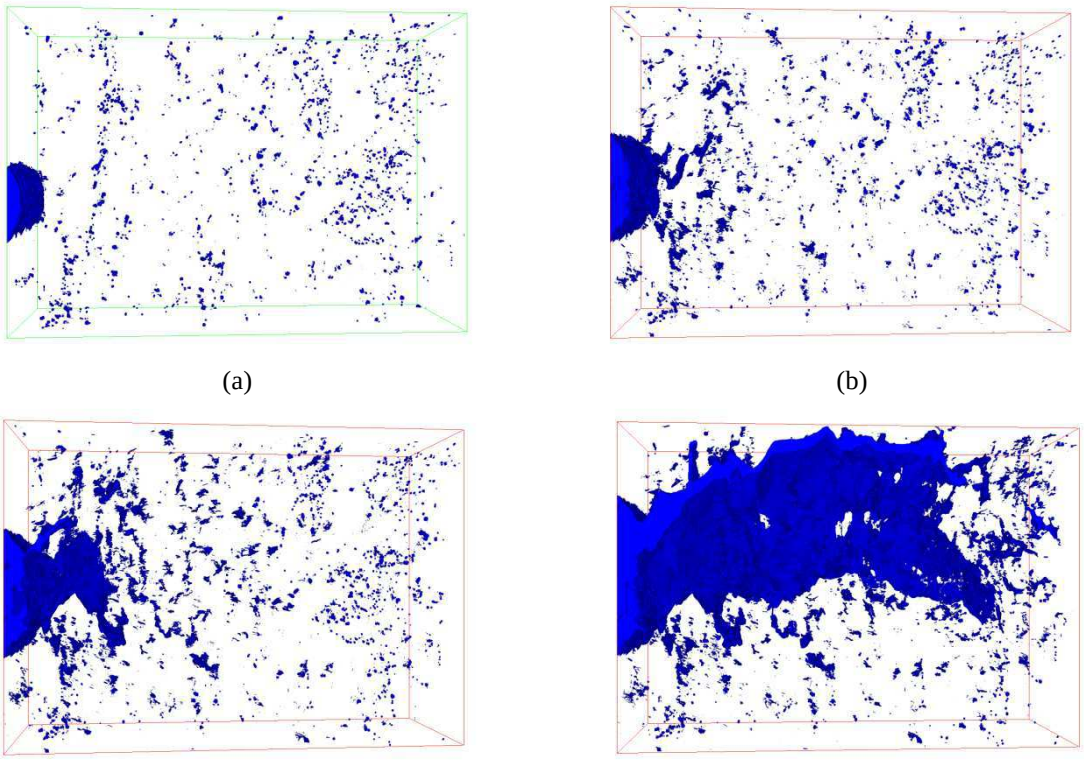

(a) (b)

(c) (d)

Fig. IV-6 3D view of thresholded sub-volumes (T x W x L = 770 x 1335 x 940µm^3) for (a) δ5= 0µm (b) δ5= 27.6µm (c) δ5= 42.5µm (d) δ5= 77.4µm

Quantitative post-processing of the porosity is presented in Fig. IV-8, in the form of maps showing the maximum void volume fraction field in the L direction (i.e, crack opening

direction) superimposed with the crack opening displacement map as defined in section 2.2, for different values of δ5. The whiter the zone, the more open the crack. Initially, a few heterogeneities can be observed in the void volume fraction field, with locations were initial porosity is more important –about 5%- (Fig. IV-8a). We remind that these void volume fractions are averaged on volumes of 50µm x 50µm x 50µm, which explains why they are much larger than the initial void volume fraction announced in section 1 averaged over a volume of 0.53mm^3. It seems that these initial heterogeneities influence, at least partly, the crack path, as these initial locations undergo the most important and rapid void growth. Thus, for δ5=27.6µm (Fig. IV-8b), δ5=42.5µm (Fig. IV-8c) or δ5=56.9µm (Fig. IV-8d), the largest increase in void volume fraction occurs at locations which, initially, exhibited the highest values of porosity. During the loading, the porosity can locally reach values larger than 10%. Besides, as the crack propagates, its front isn't straight anymore, as it tends to be more advanced in zones where the porosity was maximal at the previous steps (Fig. IV-8c and d).

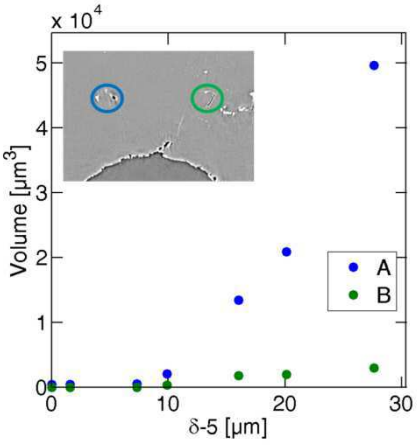

Fig. IV-7 Evolution of the volume of two cavities located ahead of the notch.

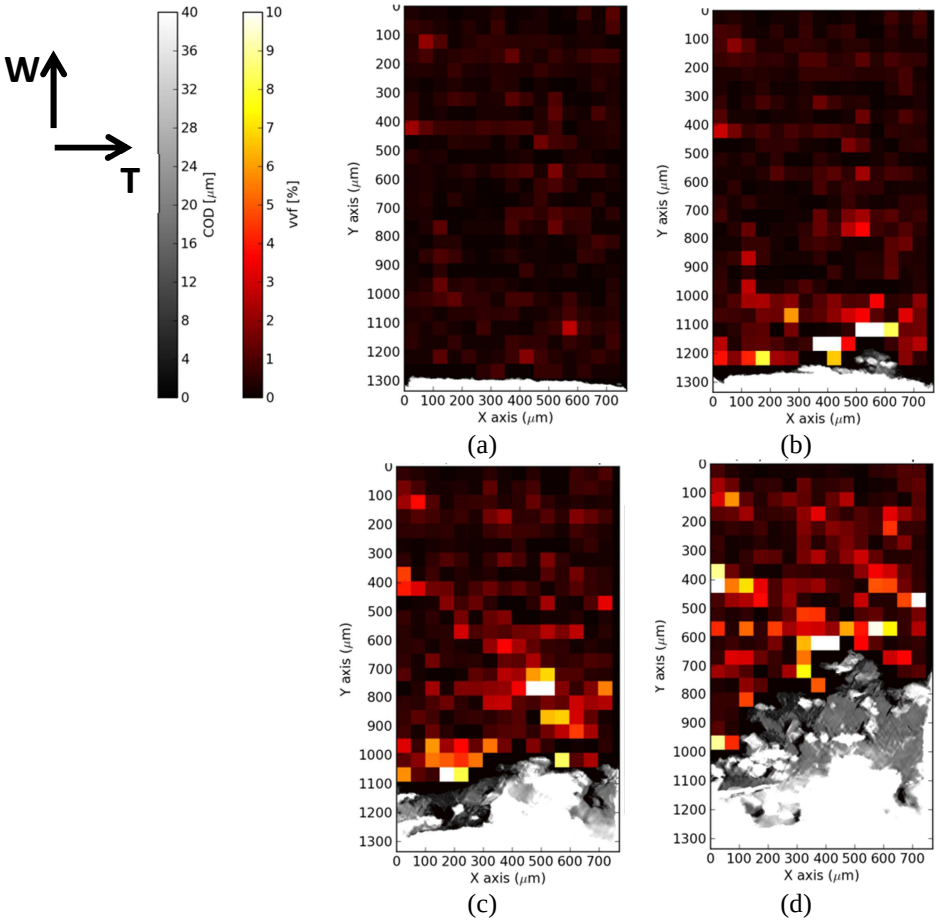

Fig. IV-8 Maximum void volume fraction and COD maps for δ5= (a) 0µm (b) 27.6µm (c) 42.5µm and (d) 56.9µm.

Fig. IV-9 shows the evolution of the average porosity ahead of the crack tip as a function of the distance to the initial notch, for different values of δ5. These values were obtained by processing the previous maps in the following way. First, the crack front was determined and discretized following the 50µm boxes sides. Then, this crack front was propagated at different distances and the void volume fraction field was averaged along the subsequently propagated crack fronts. Until δ5=20.1µm, the average porosity ahead of the crack tip increases, but the pre-crack does not propagate and just opens. Then, the critical porosity for crack propagation, from Fig. IV-9, is between 3% and 4%.

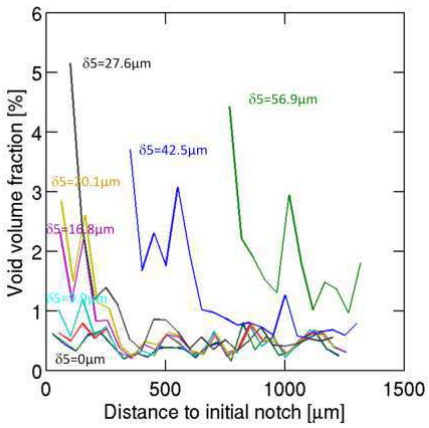

Fig. IV-9 Evolution of average void volume fraction versus the distance to the initial crack front

4. Conclusion

In the present study, ductile fracture of 2024-T351 aluminum was investigated qualitatively and quantitatively, via in-situ tension on a CT-specimen under X-ray laminography. Damage was found to occur by fracture of coarse intermetallic particles located at grain boundaries. In this particular case, almost no tunneling occurred. Slant crack propagation was observed almost as soon as propagation started, and, although growth of voids nucleated at large intermetallic particles was observed and measured, the governing mechanism in our case seemed to be void sheeting, in spite of the high stress triaxialities values that could be expected in this specimen (between 0.4 and 1.4). A field of the void volume fraction was computed and suggested that initial porosity heterogeneities predetermined the crack path, while providing information which could prove useful when using a micromechanical model, such as a critical porosity at which the crack propagates. The predominance of void sheeting mechanisms justifies the utilization of a shear localization failure criterion such as the Hosford-Coulomb criterion in a future attempt to simulate the slant propagation of the crack.

Conclusions and Perspectives

The main realization of this thesis is the development of a robust experimental protocol aimed at studying the effect of a wide range of stress states on metals ductility. After a thorough parametric study, a stocky tubular tension-torsion specimen was designed, which allows an accurate and easy control of the stress state. Although the plane stress conditions prevailing in the gage section do not allow to uncouple the effects of the stress triaxiality and the Lode angle parameter – which could be interesting to compare the damage mechanisms with the results predicted by unit cell models where such uncoupling is possible– the history of both parameters, was registered and taken into account. In the steel investigated, where substantial variations of the stress state occur after necking, the use of a linear damage accumulation rule is sufficient to get satisfactory predictions of the onset of fracture. In the aluminum alloy, a non-linear damage accumulation rule gives very promising results for the prediction of fracture in the case of non-proportional loading. Therefore, this protocol is able to provide reliable experimental databases for the calibration of fracture models – like the phenomenological Hosford-Coulomb model calibrated here- in a range of stress states that is widely encountered in industrial contexts, especially, sheet forming . One particular interest of the stocky tubular tension-torsion specimen developed in this study appeared in the construction of the fracture locus of aluminum 2024-T351. Indeed, this axisymmetric geometry is very well adapted to investigations under pure shear loading compared with flat shear specimens. It is also worth noting that the experimental boundary conditions were applied in the simulations, so as to be able to capture post-necking behavior under multiaxial loading. This procedure was successful in the case of the steel.

In the aftermath of this work, further investigations can be considered.

For instance, an investigation on the effect of the strain rate on the ductility of aluminum 2024-T351 would be worthwhile, as this material is prone to dynamic strain ageing and since several works in the literature suggest that this type of phenomenon can significantly affect ductility.

Besides, the microstructure, yield stress and hardening capacity of 2024-T351 aluminum alloy as well as that of 36NiCrMo16 steel, can be substantially modified by thermal treatments. Therefore, these materials could be used to analyze the influence of the microstructure, yield stress and hardening coefficient on the macroscopic fracture locus, but also on damage mechanisms, using the type of quantitative analyses presented in Chapter III.

One can note that in Chapter III, only specimens subjected to proportional loading were examined by SEM microscopy. No such investigation was undertaken for specimens

subjected to non-proportional loading, as these analyses were very time consuming. However, this could be an interesting perspective, to assess the effect of preloading on particle cracking/debonding and on voids, and thus, link this microstructural information to the macroscopic differences observed in the fracture strain. For instance, one can imagine how, during preloading in tension, damage of coarse intermetallic particles leads to a predisposition of the material to break earlier during the second part of the test. Conversely, closure of initial voids during pre-compression must contribute to delay the material failure during a subsequent loading. However, one can expect a little more complexity in these mechanisms. For instance, during preloading in compression, cavity nucleation by decohesion, or particle breaking in a direction parallel to the loading direction with no cavity growth, could also occur. During preloading in shear, pre-existing voids may rotate and elongate, while cracks coming from broken particles may grow and become less elongated, but still have a preferred orientation, as observed in Chapter III. Then, it would be interesting to investigate what would happen if tension, or combined tension and torsion were to be applied to such a configuration. Such sequential biaxial tests could be run in the SEM, using the tension and torsion machine available at LMS, but would provide only surfacic information. X-ray tomography would be very well adapted to this study, more than SEM metallography, of course, because it would avoid artefacts due to metallographic preparations, and because the quantitative analysis would be more reliable, but especially because it would allow to access any location within the thickness of a stick extracted from the specimen gage section, which was not the case in the SEM metallography. Now, after the unloading phase of the non-proportional loading tests, FEA showed that the stress state and strain field are more heterogeneous in the gage section, especially for pre-loading in compression or tension. Besides, for torsion-dominated loading, it would allow to really access the specimen surface, which disappears during polishing. Such experimental data would give interesting insight, to be compared with predictions of unit cell calculations under non-proprotional loading (Benzerga et al. [75]), or other future unit cell calculations featuring shear-dominant pre-loadings.

Another outlook concerns the in-situ tests under X-ray laminography. The partial results presented in Chapter IV were part of a wider experimental campaign at ESRF, which consisted in investigating the effect of the stress state via in-situ tests under X-ray laminography for three plane stress specimens, besides the CT specimen: a notched tensile specimen, a tensile specimen with a central hole, and a flat shear specimen. The study performed on the CT specimen showed that even at high stress triaxialities, void sheeting is

predominant in aluminum 2024-T351, and this justifies the use of the shear localization Hosford-Coulomb fracture initiation model. Tests on the three other geometries would give precious qualitative and quantitative information on damage evolution under very different stress states, providing additional justification for the choice of a damage model, or quantitative data for micromechanical models. It was mentioned, in Chapter II, that the flat shear specimen is not suitable for the analysis of ductility under pure shear loading. However, even if this kind of specimen breaks under uniaxial tension near the free ends, it could be possible to observe in-situ and in three dimension damage evolution under shear conditions. Besides, this kind of study should preferentially be performed on a material with more microstructural contrast than aluminum 2024-T351, therefore more suitable for digital volume correlation. The evolution of chosen porosities could then be directly compared with the predictions of micromechanical models, with the measured displacement applied as boundary conditions to the unit cell, for a direct quantitative validation of the model.

References

[1] W. Lode, "Versuche über den Einfluß der mittleren Hauptspannung auf das Fließen der Metalle Eisen, Kupfer und Nickel," *Zeitschrift für Physik*, vol. 11-12, pp. 913-939, 1926.

[2] A. A. Benzerga and J. B. Leblond, "Ductile fracture by void growth to coalescence," *ADV. APPL. MECH.*, no. 44, pp. 169-305, 2010.

[3] J. W. Hancock and A. C. Mackenzie, "On the mechanisms of ductile failure in high-strength steels subjected to multi-axial stress states," *J. MECH. PHYS. SOLIDS*, vol. 24, pp. 147-169, 1976.

[4] P. W. Bridgman, *Studies in large plastic flow and fracture*. Cambridge: Harvard University Press, 1964.

[5] Y. Bao and T. Wierzbicki, "On fracture locus in the equivalent strain and stress triaxiality space," *INT. J. MECH. SCI.*, no. 46, pp. 81-89, 2004.

[6] I. Barsoum and J. Faleskog, "Rupture mechanisms in combined tension and shear - experiments," *INT. J. SOLIDS. STRUCT.*, vol. 44, pp. 1768-1786, 2007.

[7] M. Dunand and D. Mohr, "Optimized butterfly specimen for the fracture testing of sheet materials under combined normal and shear loading," *ENG. FRACT. MECH.*, vol. 78, pp. 2919-2934, 2011.

[8] F. Bron, J. Besson, and A. Pineau, "Ductile rupture in thin sheets of two grades of 2024 aluminum alloy," *MATER. SCI. ENG.* , vol. 380, pp. 356-364, 2004.

[9] A. S. Argon and J. Im, "Separation of second phase particles in spheroidized 1045 steel, CU-0.6pct Cr Alloy and Maraging Steel in Plastic Straining," *METALL TRANS A*, vol. 6, pp. 839-851, 1975.

[10] F. M. Beremin, "Cavity formation from inclusions in ductile fracture," *METALL TRANS A*, vol. 12, pp. 723-731, 1981.

[11] L. Babout, E. Maire, and R. Fougères, "Damage initiation in model metallic materials : X-ray tomography and modelling," *ACTA MATER.*, vol. 52, pp. 2475-2487, 2004.

[12] S. Bugat, "Comportement et endommagement des aciers austéno-ferritiques vieillis: une approche micromécanique," Ecole Nationale Supérieure des Mines de Paris, Ph.D. thesis 2000.

[13] E. Maire, O. Bouaziz, M. Di Michiel, and C. Verdu, "Initiation and growth of damage in a dual-phase steel observed by X-ray microtomography," *ACTA MATER.*, vol. 56, pp. 4954-4964, 2008.

[14] A. A. Benzerga, "Rupture ductile des tôles anisotropes," Ecole Nationale Supérieure des Mines de Paris, Ph.D. thesis 2000.

[15] A. A. Benzerga, J. Besson, and A. Pineau, "Anisotropic ductile fracture - part I : experiments," *ACTA MATER.*, vol. 52, pp. 4623-4638, 2004.

[16] T. F. Morgeneyer, J. Besson, H. Proudhon, M. J. Starink, and I. Sinclair, "Experimental and numerical analysis of toughness anisotropy in AA2139 Al-alloy sheet," *Acta Materialia*, vol. 57, pp. 3902-3915, 2009.

[17] A. Weck, D. S. Wilkinson, H. Toda, and E. Maire, "2D and 3D visualization of ductile fracture," *ADV. ENG. MATER.*, vol. 8, pp. 469-472, 2006.

[18] G. Le Roy, J. D. Embury, G. Edward, and M. F. Ashby, "A model of ductile fracture based on the nucleation and growth of voids," *ACTA METALL.*, vol. 29, pp. 1509-1522, 1981.

[19] T. Pardoen and F. Delannay, "Assessment of void growth models from porosity measurements in cold-drawn copper bars," *METALL TRANS A* , vol. 29, pp. 1895-1909, 1998.

[20] B. Marini, F. Mudry, and A. Pineau, "Experimental study of cavity growth in ductile rupture," *ENG. FRACT. MECH.*, vol. 22, pp. 989-996, 1985.

[21] D. Chae and D. A. Koss, "Damage accumulation and failure in HSLA-100 stel.," *MATER. SCI. ENG. A*, vol. 366, pp. 299-309, 2004.

[22] Y. Shen et al., "Three-dimensional quantitative in situ study of crack initiation and propagation in AA6061 aluminum alloy sheets via synchrotron laminography and finite-element simulations," *ACTA MATER.*, vol. 61, pp. 2571-2582, 2013.

[23] A. Ghahremaninezhad and K. Ravi-Chandar, "Ductile failure behavior of polycrystalline Al 6061-T6," *INT. J. FRACTURE*, vol. 174, pp. 177-202, 2012.

[24] A. Ghahremaninezhad and K. Ravi-Chandar, "Ductile failure behaviour of polycrystalline Al6061-T6 under shear dominant loading," *INT. J. FRACTURE*, vol. 180, pp. 23-39, 2013.

[25] B. J. Lee and M. E. Mear, "Stress concentration induced by an elastic spheroidal particle in a plastically deforming solid," *J. MECH. PHYS. SOLIDS*, vol. 47, pp. 1301-1336, 1999.

[26] M. Cockroft and D. Latham, "Ductility and workability of metals," *J INST METALS*, vol. 96, pp. 33-39, 1968.

[27] J. Rice and D. Tracey, "On the ductile enlargement of voids in triaxial stress fields," *J. MECH. PHYS. SOLIDS*, vol. 17, pp. 201-217, 1969.

[28] P. F. Thomason, *Ductile fracture of metals*. New York: Pergamon Press, 1988.

[29] A. Gurson, "Continuum theory of ductile ruptuer by void nucleation and growth - part I: yield criteria and flow rules for porous ductile media," *J. ENG. MATER.-T. ASME* , vol. 99, pp. 2-15, 1977.

[30] V. Tvergaard and A. Needleman, "Analysis of the cup-cone fracture in a round tensile bar," *ACTA METALL.*, vol. 32, pp. 157-169, 1984.

[31] J. Faleskog, X. Gao, and C. Fong Shih, "Cell model for nonlinear fracture analysis. Part I - micromechanics calibration," *INT. J. FRACTURE*, vol. 89, pp. 355-373, 1998.

[32] J. Koplik and A. Needleman, "Void growth and coalescence in porous plastic solids," *INT. J. SOLIDS STRUCT.*, vol. 22, pp. 989-996, 1988.

[33] K. S. Zhang, J. B. Bai, and D. François, "Numerical analysis of the influence of the Lode parameter on void growth," *INT. J. SOLIDS STRUCT.*, vol. 38, pp. 5847-5856, 2001.

[34] I. Barsoum and J. Faleskog, "Rupture mechanisms in combined tension and shear - micromechanics," *INT. J. SOLIDS STRUCT.*, vol. 44, pp. 5481-5498, 2007.

[35] K. Nahshon and J. W. Hutchinson, "Modification of the Gurson Model for shear failure," *EUR J MECH A-SOLID* , vol. 27, pp. 1-17, 2008.

[36] T. F. Morgeneyer and J. Besson, "Flat to slant ductile fracture transition : tomography examination and simulations using shear-controlled void nucleation," *SCRIPTA MATER*, vol. 65, pp. 1002-1005, 2011.

[37] M. Gologanu, J. B. Leblond, and J. Devaux, "Approximate models for ductile metals containing nonspherical voids - case of axisymmetric prolate ellipsoidal cavities," *J. MECH. PHYS. SOLIDS*, vol. 41, pp. 1723-1754, 1993.

[38] M. Gologanu, J. B. Leblond, and J. Devaux, "Approximate models for ductile metals containing nonspherical voids - case of axisymmetric oblate ellipsoidal cavities," *J. ENG. MATER.-T ASME.*, vol. 116, pp. 290-297, 1994.

[39] M. Gologanu, J. B. Leblond, G. Perrin, and J. Devaux, *Recent extensions of Gurson's model for porous ductile metals*, Springler-Verlag, Ed. New-York: P. Suquet ed., Continuum Micromechanics, 1997.

[40] A. A. Benzerga and J. Besson, "Plastic potentials for anisotropic porous solids," *EUR. J. MECH. A*, vol. 20, pp. 397-434, 2001.

[41] S. M. Keralavarma and A. A. Benzerga, "An approximate yield criterion for anisotropic porous media," Comptes rendus Mécanique 2008.

[42] S. M. Keralavarma and A. A. Benzerga, "A constitutive model for plastically anisotropic solids with nonspherical voids," *J. MECH. PHYS. SOLIDS*, vol. 58, pp. 874-901, 2010.

[43] C. Bordreuil, E. Salle, and J.- C. Boyer, "An orthotropic specific damage model with inclusion consideration," *J. MATER. PROCESS. TECH.*, vol. 143-144, pp. 337-341, 2003.

[44] N. Aravas and P. Ponte-Castañeda, "Numerical methods for porous metals with deformation-induced anisotropy," *COMPUT. METHOD. APPL. M.*, vol. 193, pp. 3767-3805, 2004.

[45] K. Danas and P. Ponte-Castañeda, "Influence of the Lode parameter and the stress triaxiality on the failure of elasto-plastic porous materials," *INT. J. SOLIDS STRUCT.*, vol. 49, pp. 1325-1342, 2012.

[46] J. W. Hutchinson and V. Tvergaard, "Comment on “Influence of the Lode parameter and the stress triaxiality on the failure of elasto-plastic porous materials” by K. Danas and P. Ponte Castañeda," *INT. J. SOLIDS STRUCT.*, no. 49, pp. 3484-3485, 2012.

[47] K. L. Nielsen, J. Dahl, and V. Tvergaard, "Collapse and coalescence of spherical voids subject to intense shearing studied in full 3D," *INT. J. FRACT.*, vol. 177, pp. 97-108, 2012.

[48] X. Gao et al., "On stress-state dependent plasticity modeling: Significance of the hydrostatic stress, the third invariant of stress deviator and the non-associated flow rule," *INT. J. PLASTICITY*, vol. 27, pp. 217-231, 2011.

[49] Y. Bai and T. Wierzbicki, "Application of extended Mohr-Coulomb criterion to ductile fracture," *INT. J. FRACTURE*, vol. 161, pp. 1-20, 2010.

[50] C. Coulomb, *Essai sur une application des regles des maximis et minimis a quelques problèmes de statique relatifs a l'architecture.*: Mem Acad Roy des Sci, 1776.

[51] O. Mohr, *Abhandlungen aus demGebiete der Technischen Mechanik (2nd ed).* Berlin: Ernst, 1914.

[52] D. Bigoni and A. Piccolroaz, "Yield criteria for quasibrittle and frictional materials," *INT. J. SOLIDS STRUCT.*, vol. 41, pp. 2855-2878, 2004.

[53] D. Mohr and S. Marcadet, "Hosford-Coulomb model for predicting the onset of ductile fracture at low stress triaxialities," *submitted for publication*, 2013.

[54] K. L. Nielsen and V. Tvergaard, "Failure by void coalescence in metallic materials containing primary and secondary voids subject to intense shearing," *INT. J. SOLIDS STRUCT.*, vol. 48, pp. 1255-1267, 2011.

[55] M. Dunand and D. Mohr, "Effect of Lode parameter on plastic flow localization at low stress triaxialities," *submitted for publication*, 2013.

[56] D. Mohr and S. Henn, "Calibration of Stress-triaxiality Dependent Crack Formation Criteria: A New Hybrid Experimental–Numerical Method," *Experimental Mechanics*, vol. 47, pp. 805-820, 2007.

[57] X. Teng, H. Mae, Y. Bai, and T. Wierzbicki, "Pore size and fracture ductility of aluminum low pressure die casting," *Engineering Fracture Mechanics*, vol. 76, pp. 983-996, 2009.

[58] D. Mohr and F. Ebnoether, "Plasticity and fracture of martensitic boron steel under plane stress conditions," *International Journal of Solids and Structures*, vol. 46, pp. 3535-3547, 2009.

[59] M. Dunand and D. Mohr, "Hybrid experimental–numerical analysis of basic ductile fracture experiments for sheet metals," *International Journal of Solids and Structures*, vol. 47, pp. 1130-1143, 2010.

[60] M. Bornert et al., "Assessment of Digital Image Correlation Measurement Errors: Methodology and Results," *Experimental Mechanics*, vol. 49, pp. 353-370, 2009.

[61] M. A. Sutton, J. J. Orteu, and H. Schreier, *Image correlation for shape, motion and deformation measurements: basic concepts, theory and applications*, Springer, Ed., 2009.

[62] G. I. Taylor and H. Quinney, "The plastic distortion of metals," *Philosophical Transactions of the Royal Society of London. Series A*, vol. 230, pp. 323-362, 1932.

[63] D. Nouailhas and G. Cailletaud, "Tension-torsion behavior of single-crystal superalloys: Experiment and finite element analysis," *International Journal of Plasticity*, vol. 11, pp. 451-470, 1995.

[64] J. X. Zhang and Y. Y. Jiang, "Lüders bands propagation of 1045 steel under multiaxial stress state," *International Journal of Plasticity*, vol. 21, pp. 651-670, 2005.

[65] A. S. Khan, R. Kazmi, A. Pandey, and T. Stoughton, "Evolution of subsequent yield surfaces and elastic constants with finite plastic deformation. Part-I: A very low work hardening aluminum alloy (Al6061-T6511)," *International Journal of Plasticity*, vol. 25, pp. 1611-1625, 2009.

[66] A. S. Khan, A. Pandey, and T. Stoughton, "Evolution of subsequent yield surfaces and elastic constants with finite plastic deformation. Part II: A very high work hardening aluminum alloy (annealed 1100 Al)," *International Journal of Plasticity*, vol. 26, pp. 11241-1431, 2010.

[67] T. Kuwabara, K. Yoshida, K. Narihara, and S. Takakashi, "Anisotropic plastic deformation of extruded aluminum alloy tube under axial forces and internal pressure," *International Journal of Plasticity*, vol. 21, pp. 101-117, 2005.

[68] Y. P. Korkolis, S. Kyriakides, T. Giagmouris, and L. H. Lee, "Constitutive Modeling and Rupture Predictions of Al-6061-T6 Tubes Under Biaxial Loading Paths," *Journal of Applied Mechanics*, vol. 77, 2010.

[69] U. S. Lindholm, A. Nagy, G. R. Johnson, and J. M. Hoegleldt, "Large Strain, High-strain Rate Testing of Copper," *Journal of Engineering Materials and Technology - transactions of the ASME*, vol. 102, pp. 376-381, 1980.

[70] X. Gao, T. Zhang, M. Hayden, and C. Roe, "Effects of the stress state on plasticity and ductile failure of an aluminum 5083 alloy," *International Journal of Plasticity*, vol. 25, pp. 2366-2382, 2009.

[71] S. M. Graham, T. T. Zhang, X. S. Gao, and M. Hayden, "Development of a combined tension–torsion experiment for calibration of ductile fracture models under conditions of low triaxiality," *International Journal of Mechanical Sciences*, vol. 54, pp. 172-181, 2012.

[72] S. S. Haltom, S. Kyriakikdes, and K. Ravi-Chandar, "Ductile failure under combined shear and tension," *INT. J. SOLIDS STRUCT.*, vol. 50, pp. 1507-1522, 2013.

[73] J. H. Sung, J. H. Kim, and R. H. Wagoner, "A plastic constitutive equation incorporating strain, strain-rate, and temperature," *International Journal of Plasticity*, vol. 26, pp. 1746-1771, 2010.

[74] F. D. Fischer, O. Kolednkik, G. X. Shan, and F. G. Rammerstorfer, "A note on calibration of ductile failure damage indicators," *International Journal of Fracture*, vol. 73, pp. 343-357, 1995.

[75] A. A. Benzerga, D. Surovik, and S. M. Keralavarma, "On the path-dependence of the fracture locus in ductile materials - Analysis," *International Journal of Plasticity*, vol. 37, pp. 157-170, 2012.

[76] L. Xue, "Damage accumulation and fracture initiation in uncracked ductile solids subject to triaxial loading," *International Journal of Solids and Structures*, vol. 44, pp. 5163-5181, 2007.

[77] T. B. Stoughton and J. W. Yoon, "A new approach for failure criterion for sheet metals," *International Journal of Plasticity*, vol. 27, pp. 440-458, 2011.

[78] A. S. Khan and H. Liu, "A new approach for ductile fracture prediction on Al 2024-T351 alloy," *INT. J. SOLIDS. STRUCT.*, vol. 35, pp. 1-12, 2012.

[79] Y. Lou, H. Huh, S. Lim, and K. Pack, "New ductile fracture criterion for prediction of fracture forming limit diagrams of sheet metals," *International Journal of Solids and Structures*, vol. 49, pp. 3605-3615, 2012.

[80] Y. Lou and H. Huh, "Extension of a shear-controlled ductile fracture model considering the stress triaxiality and the Lode parameter," *International Journal of Solids and Structures*, vol. 50, pp. 447-455, 2013.

[81] I. Barsoum and J. Faleskog, "Micromechanical analysis on the influence of the lode parameter on void growth and coalescence," *INT. J. SOLIDS STRUCT.*, vol. 2011, pp. 925-938, 2011.

[82] F. Barlat, D. J. Lege, and J. C. Brem, "A six-component yield function for anisotropic materials," *International Journal of Plasticity*, vol. 7, pp. 693–712, 1991.

[83] A. P. Karafillis and M. C. Boyce, "A general anisotropic yield criterion using bounds and a transformation weighting tensor," *Journal of the Mechanics and Physics of Solids*, vol. 41, pp. 1859–1886, 1993.

[84] Y. Bai and T. Wierzbicki, "A new model of metal plasticity and fracture with pressure and Lode dependence," *INT. J. PLASTICITY*, vol. 24, pp. 1071-1096, 2008.

[85] F. Bron and J. Besson, "A yield function for anisotropic materials. Application to aluminum alloys.," *International Journal of Plasticity*, vol. 20, pp. 937-963, 2004.

[86] T. Giagmouris, S. Kyriakides, Y. P. Korkolis, and L.-H. Lee, "On the localization and failure in aluminum shells due to crushing induced bending and tension," *International Journal of Solids and Structures*, vol. 47, pp. 2680–2692, 2010.

[87] D. Wagner, J. C. Moreno, C. Prioul, J. M. Frund, and B. Houssin, "Influence of dynamic strain aging on the ductile tearing of," *Journal of Nuclear Materials*, vol. 300, pp. 178-191, 2002.

[88] A. Benallal, T. Berstad, T. Borvik, A. H. Clausen, and O. S. Hopperstad, "Dynamic strain aging and related instabilities:," *European Journal of Mechanics A/Solids*, vol. 25, pp. 397-424, 2006.

[89] W. F. Hosford, "A generalized isotropic yield criterion," *Journal of Applied Mechanics*, vol. 39, p. 607, 1972.

[90] D. Mohr and S. Henn, "A new method for calibrating phenomenological crack formation criteria - report 113," Impact and Crashworthiness Laboratoryn, Massachusetts Institute of Technology, Cambridge, MA, Technical report 2004.

[91] M. Luo and T. Wierzbicki, "Numerical failure analysis of a stretch-bending test on dual-phase steel using phenomenological fracture model," *International Journal of Solids and Structures*, 2010.

[92] Abi Akl, "La comparaison des essais de cisaillement pour caractériser la rupture ductile à basse triaxialité," Impact and Crashworthiness Laboratory, Massachusetts Institue of Technology, Cambridge, MA, internship report 2013.

[93] M. Bruenig, O. Chyra, D. Albrecht, L. Driemeier, and M. Alves, "A ductile damage criterion at various stress triaxialities," *International Journal of Plasticity*, vol. 24, pp. 1731-1755, 2008.

[94] F. A. McClintock, S. M. Kaplan, and C. A. Berg, "Ductile fracture by hole growth in shear bands," *INT. J. FRACTURE MECH.*, vol. 2, no. 4, pp. 614-627, 1966.

[95] P. M. Anderson, N. A. Fleck, and K. L. Johnson, "Localization of plastic deformation in shear due to microcracks," *J. MECH. PHYS. SOLIDS*, vol. 38, no. 5, pp. 681-699, 1990.

[96] K. Danas and P. Ponte-Castañeda, "A finite strain model for anisotropic viscoplastic porous media - part II: Applications," *EUR J MECH A-SOLID*, vol. 28, pp. 402-416, 2009.

[97] C. McVeigh, F. Vernerey, W. K. Liu, B. Moran, and G. Olson, "An interactive micro-void shear localization mechanism in high strength steels," *J. MECH. PHYS. SOLIDS*, vol. 55, pp. 225-244, 2007.

[98] M. A. Rahman, C. Butcher, and Z. Chen, "Void evolution and coalescence inoprous ductile materials in simple shear," *INT. J. FRACT.*, vol. 177, pp. 129-139, 2012.

[99] M; T. Tucker, M. F. Horstemeyer, W. R. Whittington, K. N. Solanki, and P. M. Gullet, "The effect of varying strain rates and strses states on the plasticity, damage and fracture of aluminum alloys," *MECH. MATER.*, vol. 42, pp. 895-907, 2010.

[100] K. L. Taylor and A. H. Sherry, "The characterization and interpretation of ductile fracture mechanisms in AL2024-T351 using X-ray and focused ion beam tomography," *ACTA MATER*, vol. 60, pp. 1300-1310, 2012.

[101] J. Papasidero, V. Doquet, and D. Mohr, "Determination of the effect of stress state on the onset of ductile fracture through tension-torsion experiments," *Experimental Mechanics*, p. in press, 2013.

[102] H. Swift, "Length changes in metals under torsional overstrain," *ENGINEERING*, vol. 163, pp. 253-257, 1947.

[103] H. C. Wu, Z. Xu, and P. T. Wang, "Torsion test of aluminum in the large strain range," *INT. J. PLASTICITY*, vol. 13, no. 10, pp. 873-892, 1998.

[104] L. S. Toth, J. J. Jonas, P. Gilormini, and B. Bacroix, "Length changes during free end torsion: a rate sensitive analysis," *INT. J. PLASTICITY*, vol. 6, pp. 83-108, 1990.

[105] O. Cazacu, B. Revil-Baudard, and F. Barlat, "New interpretation of monotonic Swift effects: role of tension-compression asymmetry," *MECH. MATER.*, vol. 57, pp. 42-52, 2013.

[106] N. A. Fleck and J. W. Hutchinson, "Void growth in shear," in *Proc. Royal Soc. London A 407*, London, 1986, pp. 435-458.

[107] T. F. Morgeneyer, M. J. Starink, and I. Sinclair, "Evolution of voids during ductile crack propagation in an aluminum alloy sheet toughness test studied by synchrotron radiation computed tomography," *ACTA MATER.*, vol. 56, pp. 1671-1679, 2008.

[108] T. F. Morgeneyer et al., "Ductile crack initiation and propagation assessed via in situ syncrhotron radiatio-computed laminography," *Scripta Materialia*, vol. 65, pp. 1010-1013, 2011.

[109] S. Thuillier, E. Maire, and M. Brunet, "Ductile damage in aluminium alloy thin sheets: Correlation between micro-tomography observations and mechanical modeling," *Material Sciences Engineering*, vol. 558, pp. 217-225, 2012.

[110] B. Revil-Baudard, O. Cazacu, S. Thuillier, and E. Maire, "Effect of stress triaxiality on porosity evolution in notched bars: quantitative agreement between a recent dilatational model and X-ray tomography data," *Mechanics Research Communications*, vol. 50, pp. 77-82, 2013.

[111] C. Landron et al., "Validation of void growth models using X-ray microtomography characterization of damage in dual phase steels," *Acta Materialia*, vol. 59, pp. 7564-7573, 2011.

[112] D. Mohr and S. J. Marcadet, "General formulation of damage indicator models of ductile fracture at low stress triaxialities," *(submitted)*, 2012.

[113] K. L. Nielsen, J. Dahl, and V. Tvergaard, "Collapse and coalescence of spherical voids subject to intense shearing: studied in full 3D," *INT. J. FRACTURE*, vol. 177, pp. 97-108, 2012.

[114] D. Steglich, W. Brocks, J. Heerens, and T. Pardoen, "Anisotropic ductile fracture of Al 2024 alloys," *ENG. FRACT. MECH.*, vol. 75, pp. 3692-3706, 2008.

[115] X. Teng, H. Mae, Y. Bai, and T. Wierzbicki, "Pore size and fracture ductility of aluminum low pressure die casting," *Engineering Fracture Mechanics*, vol. 76, pp. 983-996, 2005.

[116] E. Maire, C. Bordreuil, L. Babout, and J. C. Boyer, "Damage initiation and growth in metals. Comparison between modeling and tomography experiments," *J. MECH. PHYS. SOLIDS*, vol. 53, pp. 2411-2434, 2005.

[117] T. Pardoen, D. Dumont, A. Deschamps, and Y. Brechet, "Grain boundary versus transgranular ductile failure," *J. MECH. PHYS. SOLIDS*, vol. 51, pp. 637-665, 2003.

[118] T. Pardoen and J. W. Hutchinson, "An extended model for void growth and coalescence.," *J. MECH. PHYS. SOLIDS*, vol. 48, pp. 2467-2512, 2000.

[119] V. Doquet, D. Caldemaison, and T. Bretheau, "Combined tension and torsion cyclic tests inside a scanning electron microscope," in *EUROMAT*, vol. 3, Balatonszéplak, Hungary, 1994, pp. 732-739.

[120] M. Gologanu, J. B. Leblond, and J. Devaux, "Approximate models for ductile metas containing nonspherical voids - case of axisymmetric prolate ellipsoidal cavities," *J. MECH. PHYS. SOLIDS*, vol. 41, pp. 1723-1754, 1993.

[121] F. Barlat et al., "Linear transfomation-based anisotropic yield functions," *International Journal of Plasticity*, vol. 21, pp. 1009-1039, 2005.